Surface-Bound Functional Hydrogel Networks

Inaugural Dissertation to obtain the academic degree
Doctor rerum naturalium (Dr. rer. nat.)

Submitted to the Department of Biology, Chemistry, Pharmacy
of Freie Universität Berlin

by

Anna Lydia Herrmann

June 2020

The following project was carried out within the research group of Prof. Dr. Rainer Haag from **October 2016** until **May 2020** at the Institute of Chemistry and Biochemistry of the Freie Universität Berlin.

1. Reviewer: Prof. Dr. Rainer Haag, Freie Universität Berlin

2. Reviewer: Prof. Dr. Christoph Schalley, Freie Universität Berlin

Date of defense: 2020, September 1st

Acknowledgements

Completion of this doctoral dissertation was only possible with the support of several people and I would like to express my sincere gratitude to all of them. First of all, I want to thank Prof. Dr. Rainer Haag for having me as a part of his vibrant, helpful, and interesting research group. I really enjoyed working on my topic and having such a nice work environment. Moreover, Prof. Dr. Christoph A. Schalley is gratefully acknowledged for co-refereeing this thesis.

I would also like to thank my scientific mentor, Dr. Uwe Schedler, who always took the time for scientific discussions and helped me with new ideas. He supported me in becoming a better researcher, he introduced me into industry projects, and thanks to him I could go abroad where, again, I grew and developed so much.

In addition, I would like to thank all former and present AG Haag group members, especially Dr. Wiebke Fischer and Eike Ziegler for being of great help and support with all questions and problems I encountered throughout those years. I would like to thank Cathleen Schlesener, Katharina Goltsche, Anja Stöshel, Elisa Quaas, Marleen Selent, and Dr. Katharina Achazi for their help with synthesis, GPC measurement, cell viability tests, and for the great help with moving to Arnimallee. For their personal support, an open ear, and the fun times I would like to thank all current and former members of our Lunch Groups. For their great support during the beginning of my PhD, I would like to thank Dr. Badri Parshad, Dr. Christoph Schlaich, and Dr. Abhishek Kumar Singh.

I would like to acknowledge the assistance of the Core Facility BioSupraMol supported by the DFG. And I want to thank Dr. Luis Cuellar for measuring AFM.

I want to thank Dr. Stephan Block, who was a great collaboration partner and who was very patient in teaching me new techniques and methods. I would also like to thank Amanuel Wolde-Kidan and Prof. Dr. Roland Netz for patiently evaluating my data and for having me as part of this interesting collaborative project.

For my time in Senftenberg I would like to thank Prof. Dr. Peter Schierack for letting me work in his group. I would like to express my gratitude to Dr. Stefan Rödiger who supervised and guided me through that project and was of great help. I want to thank Dr. Carsten Schmidt for introducing me to the biotechnology lab techniques, and I want to thank Jörg Nitschke and Alexander Böhm for all the great help with the VideoScan software, Franzi, Rafal, Olowe and Juliane I want to thank for

creating such a nice work environment and making me feel welcome. I want to express my appreciation to Dr. Aamir Ali, who was very welcoming and helped me a lot during that time.

For my stay in Boston, Massachusetts, I want to thank Prof. Dr. David Kaplan, who was so kind to let me work at his laboratory and was very helpful regarding all matters I needed assistance with. I want to thank my supervisor, Dr. Jugal Kishore Sahoo, who took the time to try to find solutions with me, and for creating a nice working environment. Chenchen, Philipp, and Long I want to thank for the great office environment, help with ordering, and their participation on my excursions. I want to thank Benjamin Andrew Allen for the good times in Somerville and the thorough English language polishing.

Further, I would like to thank Dr. Pamela Winchester for the careful language polishing of my manuscripts.

I want to thank my former classmates for the fruitful discussions across working groups and our time together from the very first semester.

To my parents, Ute and Hartwig, I will always be very grateful. They were very patient and supportive throughout all those years. To my siblings Ines and Markus, I am grateful for their moral support and encouragement. I am also thankful to the rest of my family, especially to my grandma. I wish she could have seen me finally graduate.

Lastly, I want to thank my friends, who were a huge support through all the ups and downs.

THANK YOU.

Table of Contents

1 Introduction

The recent outbreak of the severe acute respiratory syndrome coronavirus-2 (SARS-CoV-2) has become a worldwide problem. After its first appearance in late 2019 it quickly became pandemic, and societies and their economies have suffered from the consequences. In the absence of a successful treatment or vaccination, rapid detection methods are crucial for the timely implementation of measures to prevent virus transmission within societies. It is necessary to detect such diseases early to prevent further spread and to contain the virus.[1] This exemplifies the importance of fast, efficient, and reliable testing and demonstrates the value of biosensors and bioanalytical tests.

Even before the virus outbreak, however, biosensors and multiplex detection methods played a major role in the fields of clinical diagnostics, point-of-care testing, personalized medicine, and pharmaceutical research, with an important objective to understand interaction processes at the molecular level.[2] In this area, highly sensitive detection platforms with excellent specificity are required, for their ability to provide useful insights into the health of individuals.[3] In heterogeneous assays, the contact between the surface and the analyte determines the performance of the sensor, and so the quest for new and improved materials is ever increasing. Among the problems encountered are insufficient loading capacity of two-dimensional surfaces, bad accessibility of immobilized bioprobes, and the incorrect orientation of these probes.

There are many tools to improve and optimize biosensors, one of them being the use of hydrogels. Through immobilization of these water-swollen, three-dimensional polymeric networks, we can extend the limited coverage of two-dimensional surfaces and unlock enhanced immobilization capacity and accessibility of biomolecules. The improved signal intensity leads to a lower limit of detection and reduces the background signal for better signal-to-noise ratios.[4] The solution-like environment created by hydrogel matrices also stabilizes and protects the structure of delicate biomolecules that would otherwise denature on surfaces.[5]

In this work, the concept of surface-bound functional hydrogels was investigated with the aims of improving existing procedures in biosensing, developing a new method for multiplex analysis, and implementing an experimental setup for studying physical properties of hydrogel networks.

2 Theoretical Background

2.1 Hydrogels

2.1.1 Definition

A gel is defined as a viscoelastic, solid-like, but deformable material, that is composed of a substantially diluted network in a continuous gas or liquid medium.[6] More specifically, gels are classified by the dispersing medium, for hydrogels this medium is water. The network consists of a chemically or physically crosslinked, hydrophilic polymer which entails the structural stability and prevents the dissolution of the polymer into the aqueous media. Maintaining its shape while absorbing a large amount of water or aqueous media makes hydrogels the ideal candidate for the encapsulation of drugs, proteins and other biomolecules.[7-9] Furthermore, the three-dimensional matrix shows a high permeability for small molecules, metabolites, oxygen, and other water soluble components. These traits and their visco-elastic properties make hydrogels an excellent candidate for mimicking the extracellular matrix or mucus, and as a carrier material for biomolecules.[10-12]

The first hydrophilic gel (hydrogel) was synthesized by Wichterle and Lim in 1960, with the ambitious goal to create a “plastic” that is in permanent contact with human tissue. They defined the demands for a polymeric network to be placed in a human body and stated the need for a hydrophilic, three-dimensional network.[13] Ever since, the variety, demand, and range of applications have grown immensely. They are used in different fields of biotechnology, such as drug delivery, tissue engineering, and molecular diagnostics.[14, 15] Hydrogels have been generated from a variety of synthetic polymers, including polyethylene glycol (PEG), poly(N-isopropylacrylamide) (PNIPAAm), poly(2-hydroxyethyl methacrylate) (PHEMA), as well as natural polymers, such as chitosan, alginate, dextran, and hyaluronic acids. Generally, these materials are resistant to protein and cell adhesion due to their hydration properties.[16] Moreover, depending on either the inherent properties or by means of chemical modification, hydrogels can also be thermo-responsive, degradable, charged, swell upon stimuli, be self-healing, or magnetic.

2.1.2 Crosslinking methods

Hydrogels can be crosslinked either physically or chemically, as depicted in Figure 1. In general, chemical bonds are stronger and typically irreversible. Physical crosslinks are reversible, and their strength depends on the type of interaction and the amount of crosslinking.

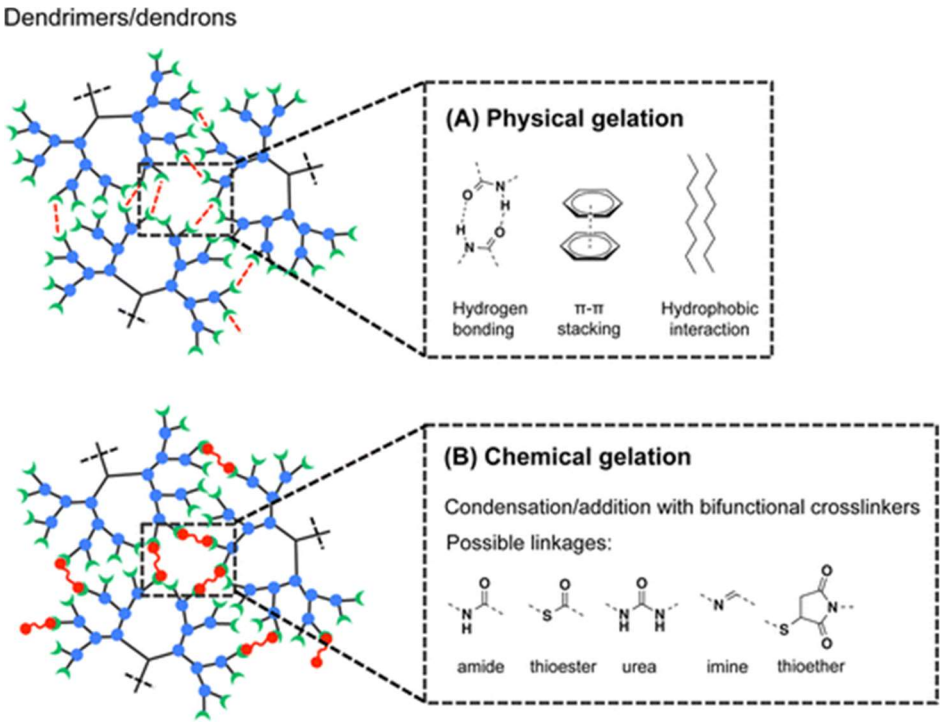

Figure 1 Examples of crosslinking methods for hydrogel formation based on chemical and physical crosslinks based on dendritic macromonomers. Reprinted with permission from ref. [17]. Copyright 2016 American Chemical Society

Physical Crosslinking

Physical crosslinks are formed when the hydrogel is built up by reversible interactions such as hydrogen bonds, ionic association, hydrophobic interactions, host-guest complexation, or metal complexation. These reversible interactions are mainly used in stimuli responsive hydrogels. This is because the non-covalent linkages will break in response to certain stimuli such as mechanical stress or physical changes. Physical changes include alteration in pH, ionic strength, temperature, or the presence of a ligand, whose affinity towards the crosslinker is stronger than the hydrogel component itself. In all these cases, the binding between

polymer and crosslinker inside the hydrogel will break up and result in property changes. The second important area for physical crosslinks is in self-healing hydrogels. Since the crosslinks are reversible a break in the hydrogel can be reversed (healed) by placing the cut pieces into contact again. For example, a very strong, tough, and self-healing hydrogel was obtained by combining two types of physical crosslinks in a single polymer hydrogel, containing iron ions (Fe^{3+}).[18] The crosslinking was based on hydrophobic interactions and is supported by ionic coordination. between Fe^{3+} and carboxylic groups. The resulting material had excellent tensile strength and elongation at break, exhibited 100% rapid recovery of elastic modulus, fracture stress and dissipated energy, and spontaneous self-healing behavior and has potential applications in biomedical and environmental engineering and in intelligent materials.

Chemical crosslinking

Chemical gelation is based on the reaction between two complementary functional groups, where covalent bonds are formed to build up the hydrogel network. In principle, two methods are possible, either already formed macromolecules are crosslinked together, or a monomer growing into a linear polymer chain is crosslinked during polymerization by a bi- or multivalent reagent. The chemical bonds are usually either obtained by photopolymerization, using photosensitive groups, or by condensation/addition reactions, which include amidation, esterification, thioesterification, Schiff base formation, Michael addition, and other click-type reactions. Click reactions are especially favorable, because they do not need an activation, they are modular, wide in scope, give very high yields, generate only inoffensive side products, and they usually form at room temperature.[19] Chemically crosslinked hydrogels are generally more stable than physically crosslinked ones, since covalent bonds are stronger than secondary bonds. Therefore, they are used more often in applications where extended use of the material is required. The use of chemical bond formation gives a diverse panel of hydrogels with adjustable physical and rheological properties. This is achieved by the careful choice of crosslinker and reaction conditions.

Naturally, both types of crosslinking can be combined into one hydrogel. An example is a supramolecular hydrogel, in which the formation of the hydrogel is based on non-covalent interactions, followed by the chemical crosslinking of the host molecules. Okumura and Ito developed this dual-crosslinked hydrogel based on polyrotaxanes. First, they threaded α-cyclodextrins onto a long PEG chain with bulky head groups and then chemically

crosslinked some of the α-cyclodextrins. The resulting hydrogel is thereby both covalently crosslinked and physically crosslinked by host-guest interaction. The topologically interlocked polymer chains can equalize stress that is applied onto the gel by letting the α-cyclodextrins move freely along the PEG chains. Thus, this hydrogel shows excellent swelling capacity (400 times its dry weight), is flexible, and is tensile to twice its length.[20]

2.1.3 Functional hydrogel network

Hydrogels come with specific properties, which originate from the molecular units of the polymer chains. These units also allow for further chemical modifications to provide networks with additional or adjustable functional properties. Typical groups, which either possess a function or are used to introduce further functions, are carboxylic acids, thiols, amines, and hydroxyl groups. These functional groups influence the hydrogel's behavior and properties, such as stiffness, swelling ratio, and responsiveness. The type of polymer influences the biocompatibility, and the degree of crosslinking is used to tune the mesh size of the network. If the inherent functions do not serve the purpose, or if additional features are needed, further groups can be introduced chemically. A prominent motive is the carboxylic group, which can be activated to bind biologically active species or react with labeling moieties. As an entrapment matrix, the hydrogel can be designed to form in situ and encapsulate and possibly immobilize a biomolecule onto a surface and keep it active and functional inside its solution like environment.

Bioorthogonal Hydrogels. Bioorthogonal reactions are reactions that do not interfere with biological processes.[21] They are especially useful in chemical biology, which strives to probe molecules in living systems. Such reactions must proceed rapidly under physiological conditions and be inert to the variety of functionalities found in vivo. Historically, the field of bioorthogonal chemistry was pioneered by Bertozzi and co-workers with the development of the Staudinger ligation, which was used to selectively label cell-surface glycans. It utilizes two chemical groups (azide and a functionalized triarylphosphine) that are absent in biological components and form a stable amide bond. Due to limitations regarding stability and reaction kinetics, Bertozzi et al. developed the strain-promoted azide-alkyne cycloaddition (SPAAC) as an alternative. The ring-strain of cyclooctyne and its derivatives promotes the progression of the reaction without the need for external activation. The strain arises from the conformational stress from the linear nature of sp-hybridized triple bonds. For cyclooctyne, this distortion lies at roughly 161°, which accounts for an energy gain of

nearly 17 kJ/mol for the reaction from the alkyne to an sp^2-hybridized double bond as in triazole.[22-24] Another very important bioorthogonal reaction is the inverse-electron demand Diels-Alder reaction, between a strained tetrazine and a strained alkene.[25] See Figure 2 for the general concept of bioorthogonal hydrogels and the mentioned chemical groups. To date, the field of bioorthogonal chemistry has been growing as it addresses the need for highly specific and robust reactions in biological contexts. Accordingly, bioorthogonal chemistry is also a favorable tool for hydrogel formation. Since the crosslinking chemistry does not interfere with the biology, it works excellently as a reaction used for building an in situ biomolecule embedding matrix. If desired, biomolecules can selectively be introduced and immobilized into the hydrogel through modification with the complementary chemical group. In contrast to a bio-reactive matrix, this inherently prevents non-specific binding. There are several hydrogels based on SPAAC chemistry. It was used as an inert matrix for enzyme immobilization in a biosensor[26] or for the (micro)encapsulation of cells with no loss in cell viability.[27, 28]

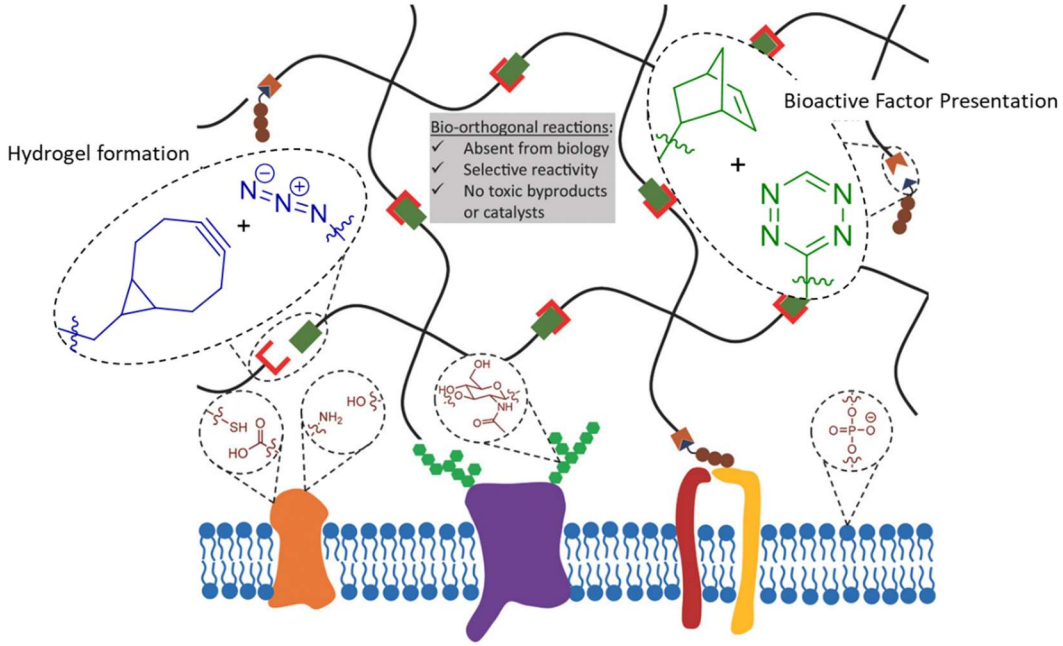

Figure 2 A bioorthogonal hydrogel matrix (black) is shown on top of a cell surface (blue lipid bilayer). As hydrogel crosslinking two bioorthogonal reactions are represented, the SPAAC reaction in blue and inverse-electron demand Diels-Alder reaction in green. Common biological functional groups are presented on the cell surface in red. Adapted with permission from ref. [29]. Copyright 2018 WILEY-VCH Verlag GmbH & Co. KGaA, Weinheim

Hydrogel matrix used as filter. Due to their porous structure, hydrogels can function as a size-selective matrix or filter. Hydrogel matrices are used to exclude unwanted larger objects, to spatially separate objects, or to accumulate sample upon incubation. For example, a PEG-based hydrogel was used as a semipermeable membrane designed for an artificial pancreas. The antifouling property of the hydrogel prevented protein attachment, which is important to prolong the lifetime of the membrane in the body, and at the same time still allowed for the diffusion of insulin and glucose.[30] A thermoresponsive hydrogel was used as a material to extract water and low-molecular-weight solutes from a larger cellulase enzyme or a virus. The hydrogel swells at low temperature, is removed by filtration, and then collapses by heating to 35 °C and can be reused. The meshes of the gel are small enough to prevent the enzyme or the virus from being absorbed and the process of hydrogel swelling does not change the ionic environment or shear conditions of the medium.[31]

2.1.4 Dendritic and hyperbranched polymer-based hydrogels

Macromolecules with a branch-on-branch structure, such as dendrimers and hyperbranched polymers, possess unique chemical and physical properties, which are beneficial in a variety of applications. Due to their highly branched repeating units, which adopt in a globular structure, a high surface-area-to-volume ratio with numerous terminal end groups is obtained.[32]

Dendrimers are monodisperse macromolecules, built up by uniform branches. They are composed of a core (multivalent initiator), repeating branching units (generations, G), and multiple peripheral functional groups.[17] These macromonomers show interesting properties. They are highly symmetric, have a defined size and architecture, and exhibit multiple reactive end groups. However, a disadvantage is the tedious, multi-step synthesis, getting even more dreary when it comes to high molecular weights. Hyperbranched polymers are essentially structurally imperfect dendritic structures. They are highly branched macromolecules with a three-dimensional dendritic architecture and show properties similar to those of the corresponding dendrimers.[33] Depending on the application, the ease of access to hyperbranched polymers, as opposed to dendrimers, can outweigh the slightly lower controllability of the hyperbranched structures. A promising class are aliphatic polyether

polyols, such as dendritic or hyperbranched polyglycerol.[34] Sunder et al. obtained excellent properties, like a high degree of branching and low polydispersity (PDI < 1.5), for

hyperbranched polyglycerol with the “ring-opening multibranching polymerization” (ROMBP). Hyperbranched polyglycerol combines a flexible aliphatic polyether backbone with multiple hydrophilic groups.[35, 36] Researchers got interested in polyglycerol-based polymers for biomedical applications because of the structural similarity to PEG, which is an FDA approved polymer and used extensively in that field. To date numerous studies have been conducted, and hyperbranched polyglycerol has been found to be highly blood- and biocompatible, non-immunogenic, and non-toxic.[37, 38] And, most importantly in its application as a matrix for biosensing, it was found to be resistant to protein adsorption and showed excellent antifouling properties.[39] Two other important advantages of hyper-branched polyglycerols for use in hydrogels are their high degree of functionality and their highly hydrophilic nature. The structural features of polyglycerol are easily tailored by adopting synthetic methodologies to the hydroxyl end groups. They allow the formation of crosslinks with groups still remaining for the introduction of additional chemical groups for advanced function. Additionally, their excellent water solubility renders them excellent component for hydrogel formation.

Historically, Newkome and co-workers described the first example of a dendrimer-based hydrogel, which was physically crosslinked. It was formed by intermolecular hydrogen bonding and hydrophobic interactions.[40] Another early example is the chemically crosslinked hydrogel based on dendritic macromolecules by Grinstaff et al. in 2002. A dendrimer based on PEG, glycerol, and succinic acid was modified with an acrylate head group and then photo-crosslinked for applications in wound healing, where they managed to successfully seal a 4.1 mm corneal laceration on an enucleated eye.[32]

The first hydrogel based on hyperbranched polyglycerol was reported by Hennink et al. in 2006. They functionalized the hydroxyl end groups with different amounts of acrylates and produced photo-crosslinked hydrogels with tunable storage moduli and low swelling capacity.[41] In combination with hyaluronic acid they embedded multipotent stromal cells into the hydrogel with a cell viability of 75%.[42] The first successful cell encapsulation into a polyether-polyol-based hydrogel was performed in the Haag group in 2011 by photo-crosslinking.[43] In the following years more cell-laden hydrogels based on a similar structure were prepared, but with further and improved crosslinking strategies, such as thiol-Michael

addition and strain-promoted azide-alkyne-cycloaddition.[44, 45] Excellent biocompatibility was achieved, and consequently the scope of applications was expanded to joint lubricant and to enzymatic immobilization for biosensing (see Figure 3).[26, 46]

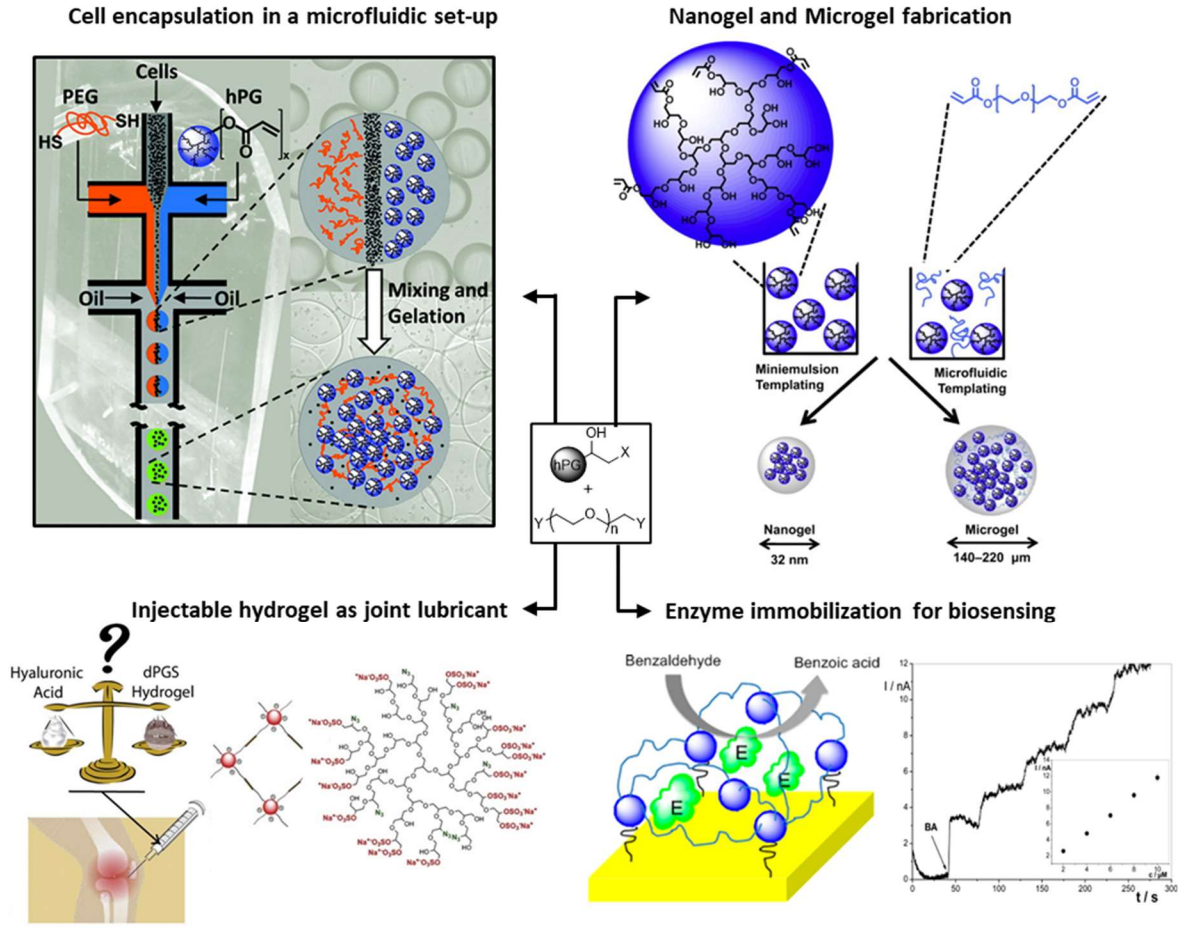

Figure 3 Overview of hPG-PEG based hydrogels in different fields of applications. Adapted with permission from ref. [26, 43, 45, 46]. Copyright 2012 American Chemical Society, 2010 Elsevier Ltd., 2017 Elsevier B.V., 2014 American Chemical Society

2.1.5 Biocompatibility and antifouling properties of PEG and hPG

A material is biocompatible, if it is not toxic and does not produce an immune response when exposed to living systems.[47] Fouling is the unwanted attachment of proteins and biofilm formation on material which is in contact with fluids. Preventing nonspecific protein adsorption and cell adhesion is crucial for the performance of devices like biosensors, implantable devices, vascular grafts, venous and urinary catheters, and is also critical in marine context on ships.[48] Many strategies in this direction have been developed, one of them being the use of biocompatible polymers with antifouling properties.[49, 50] Of these,

poly(ethylene glycol) (PEG) is one of the very well performing polymers and is used as the gold standard in many applications.[51, 52] The protein-rejecting properties of PEG are ascribed to its water-like character, its uncharged nature, and the high motility of the polymer chains. These characteristics result in a minimal interfacial energy at the polymer/water interface. Consequently, biomolecules which approach this interface will not be greatly affected.[5] In the past years, however, both linear and hyperbranched polyglycerol were also investigated for their biocompatibility as well as antifouling properties (see Figure 4).[53-55] They show excellent performance and are proposed as a replacement or addition to PEG. This is due to their structural similarity, whereby polyglycerol offers more options for chemical modification due to its numerous functional end groups.

In the context of hydrogels used as a biosensor matrix, the antifouling properties of PEG and dPG are advantageous to prevent nonspecific binding of non-targeted molecules.[56] However, the biocompatibility and options for chemical modification enable the embedding of biomolecules by either entrapment or immobilization within the network.

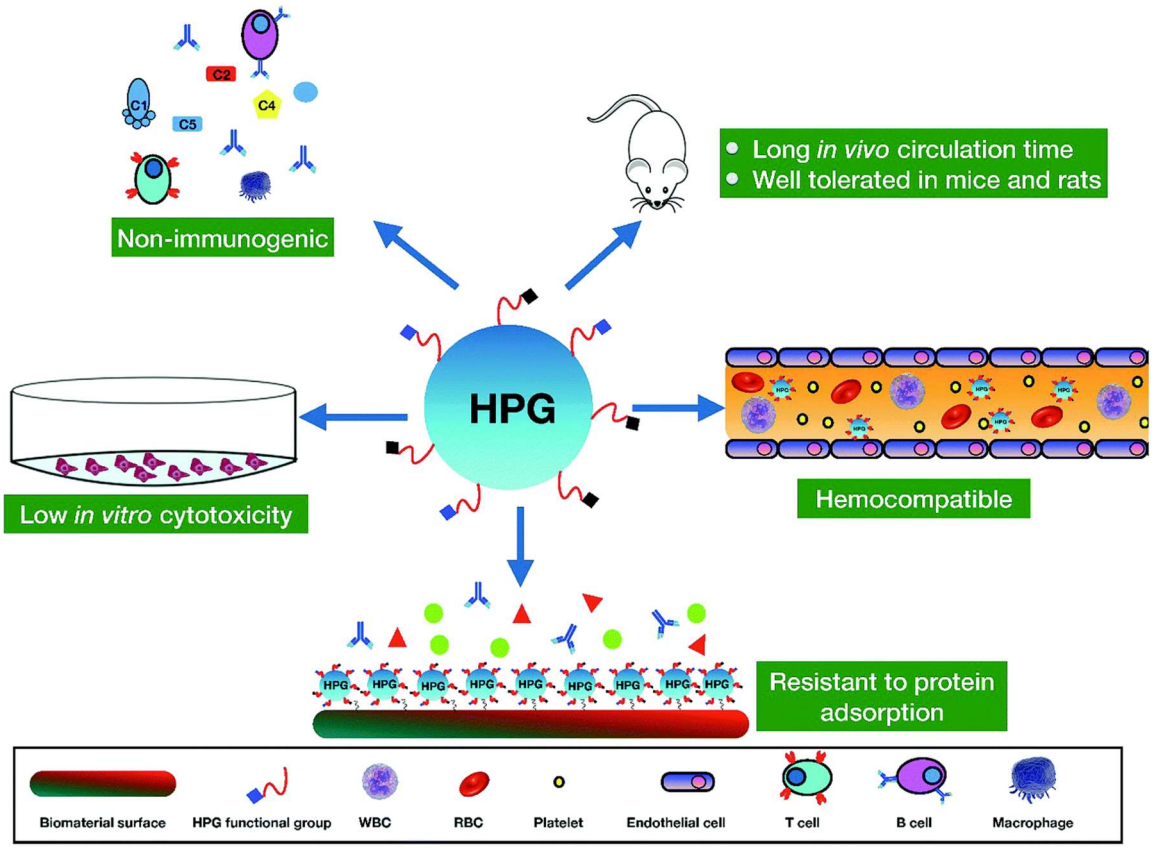

Figure 4 Overview of the biocompatibility profile of hyperbranched polyglycerols (hPGs). Reprinted with permission from ref. [38]. Copyright 2013 Royal Society of Chemistry

2.2 Network structure characteristics

2.2.1 Overview

The optimal technical features of a hydrogel depend on the demands of the application. Some properties common to hydrogels can be used to compare and qualify them. One important hydrogel feature is the absorption capacity (swelling ratio), which is the amount of water a hydrogel can hold in relation to its dry weight. For some applications, the rate of absorption is also important. Hydrogels form a three-dimensional network and thereby create pores, which can be used for encapsulation of biomolecules as well as for size selection. The durability and stability of a hydrogel are important parameters during swelling and for handling and storage. Finally, for most biomedical applications, it is favorable for a hydrogel to be colorless, odorless, non-toxic, have a low residual monomer content of unreacted species, have preferably a low price, and to degrade without the formation of toxic species. Figure 5 gives a scheme for a hydrogel at different scales, whereby the mesh size ξ is depicted in the nanoscopic regime and the free volume radius r_{FV}, which is the radius of empty voids inside the meshes between molecules, in atomic scale. Some further details and approaches on how to determine hydrogel properties are presented hereafter.

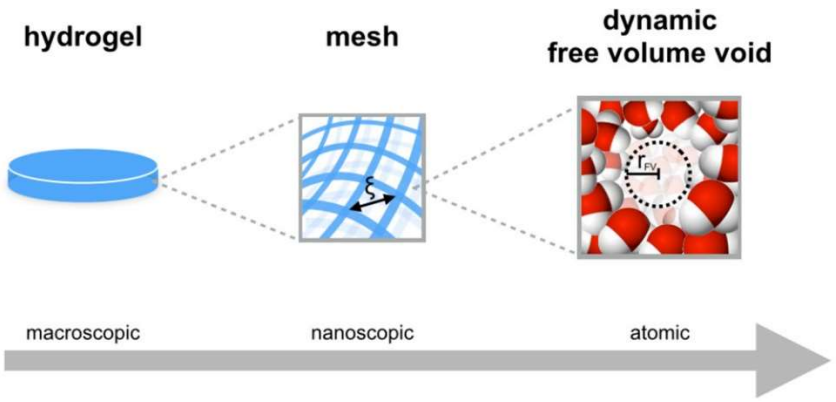

Figure 5 Scheme of a hydrogel at different scales. Reprinted with permission from ref. [57]. Copyright 2019 American Chemical Society

2.2.2 Swelling ratio

As a crosslinked polymeric network, hydrogels undergo swelling instead of dissolution in water. The mass swelling ratio (q) of a hydrogel is calculated by dividing the mass of a fully swollen hydrogel sample ($m_{swollen}$) by the mass of the dehydrated, dry sample (m_{dry}) as shown

in equation (1).[58] Alternatively, the polymer volume fraction ($\boldsymbol{\nu_{2,s}}$) is stated, which is the polymer volume divided by the volume of the swollen network. It can be related to the mass swelling ratio q by taking the density into account (see equation (2)).[59] The swelling behavior of hydrogels is influenced by the properties of the polymers used. More hydrophilic polymers, for example, lead to a higher swelling ratio. Hydrophilicity can in general be tailored by the introduction of functional groups or by using. Furthermore, swelling can be increased by using polyelectrolytes which not only increase hydrophilicity but also the charge repulsion leads to additional expansion of the network. Another important factor is the degree of crosslinking. A high extent of crosslinking forms a stiff network, decreasing the swelling upon exposure to water or aqueous solutions.[60] This is a result of shorter distances between joints, whereby smaller pores for the accommodation of water are created.

$$\boldsymbol{q = \frac{m_{swollen}}{m_{dry}}} \quad \textbf{(1)}$$

$$\boldsymbol{\nu_{2,s} = \frac{V_{dry}}{V_{swollen}} = \frac{m_{dry}/\varrho_{dry}}{m_{dry}/\varrho_{dry} + m_{water}/\varrho_{water}}} \quad \textbf{(2)}$$

From a thermodynamic point of view, the Flory-Rehner theory states that a crosslinked polymer gel, which does not contain ionic moieties and is swollen to equilibrium in liquid, is affected by two opposing forces, the thermodynamic force of mixing and the retractive force of the polymer chains. At the swelling equilibrium, these two forces are equal.[61, 62]

2.2.3 Rheology

Hydrogels are studied extensively in so many different applications that it is critical to have measures and quantities that allow us to characterize and compare hydrogels with each other and to tissue, mucus, substrates, etc. Rheology studies the deformation and flow of matter, dealing primarily with the stresses generated during the flow of complex materials including polymers, colloids, foams, and gels. It is an excellent tool to determine hydrogel mechanical properties since it is quick, sensitive, requires relatively small sample volumes, and reveals differences in the network architecture. The mechanical properties measured by rheology are best understood by using the theories of *rubber elasticity* and *viscoelasticity*. These theories consider the recovery of the polymer chain orientation and structure after elongation as time-independent and time-dependent properties, respectively.

Rubber elasticity theory. The term rubber elasticity refers to materials that can be elongated by up to 1000% and fully return to their initial state almost instantly.[63] Such materials are usually lightly crosslinked materials with a large free volume, so their response to external stress is a fast rearrangement of the polymer chains and hence, the mechanical behavior of the gel is mainly dependent on the polymer network. The recovery into the initial state is driven primarily by the reconstitution of entropy, and less by enthalpy. Other typical characteristics of rubber like elastic behavior include high extensibility generated by low mechanical stress and complete recovery after removal of the deformation.[64]

To obtain an equation that relates network characteristics of a hydrogel to mechanical stress-strain behavior, several thermodynamic models and equations are considered. It is assumed, that a) only the polymer chain itself but not individual bonds are stretched, and no internal energy changes are considered, b) that for elastomeric materials, the increase in length mainly results in a decrease of entropy (those measures are connected by the Maxwell equations), c) that the internal energy contribution to the retractive force is zero, d) no volume changes upon deformation occur and finally, e) that the elastic stress of a rubber material under uniaxial extension is directly proportional to the number of network chains per unit volume (expressed by $\frac{\rho}{\overline{M_C}}$).[64] The shear stress per unit area τ is connected to G, the shear modulus, by the extension ratio α in equation (3) and finally, the shear modulus G can be expressed by equation (4).[65, 66]

$$\tau = G \cdot (\alpha - \frac{1}{\alpha^2}) \tag{3}$$

$$G = \frac{\rho RT}{\overline{M_C}} \cdot Q^{-1/3} \cdot \left(1 - \frac{2\overline{M_C}}{\overline{M_N}}\right) \tag{4}$$

ρ is the density of the polymer, R is the ideal gas constant, T the temperature, $\overline{M_C}$ is the average molecular weight between crosslinks, Q is the volume swelling ratio and M_N is the number average molecular weight of linear polymer chain before crosslinking.

Viscoelasticity. Viscoelastic behavior reflects the combined viscous and elastic responses upon deformation. Hydrogels are typical viscoelastic materials because they are intermediate in character between liquids and solids. This theory considers the relationship between

elasticity, flow, and molecular motion in polymeric materials.[63] The imposed mechanical motion is a time dependent property where the rate of applied strain or stress matters, not only its magnitude. In a purely elastic material, an applied strain results in an immediate response in stress, which means the phase angle δ is in phase (close to zero). In purely viscous materials, the response in stress lags strain by a 90° phase. The material's response is at a maximum when the time scale of the mechanical motion is on the same time scale of the molecular motion of the polymer.[64] Viscoelastic materials like hydrogels behave somewhere in between these limiting cases. Their viscoelasticity is studied by dynamic mechanical analyses which provide information by measuring the response of a sample when it is deformed under periodic oscillation (stress or strain). In dynamic experiments the material is exposed to a sinusoidal shear strain γ (or stress ε) as expressed in equation (5), where γ_0 is the shear strain amplitude, ω is the frequency, which can also be expressed as $2\pi f$, and t is the time.[65]

$$\gamma = \gamma_0 \sin(\omega t) \tag{5}$$

The main rheological technique for hydrogel characterization is to apply small-amplitude oscillatory shear (SAOS). Thereby, the hydrogel sample is placed between parallel disks (or a cone and a disk), and a small amplitude torsional oscillation generates shear flow in the sample.[67] Typical measures that are determined by rheology are the gelation point t_{gel} by a time sweep and the dynamic moduli G' (elastic or storage modulus) and G'' (viscous or loss modulus) by strain and frequency sweeps. The time sweep yields the gelation time as the time t_{gel}, where $G'' = G'$.[68]

There are two raw components measured by the SAOS rheology measurement: (1) the torque, which combined with geometry information gives the complex modulus G^* and (2) the phase angle δ, which is the measured phase difference between the oscillating strain and stress waves. From that, G' and G'' are calculated by equations (6) – (8).[67]

$$G'' = G^* \sin\delta \tag{6}$$

$$G' = G^* \cos\delta \tag{7}$$

$$G''/G' = \tan\delta \tag{8}$$

Additionally, $\tan\delta$ is an expression for the damping factor, and it measures the ratio of the energy dissipated as heat to the maximum energy stored in the material during one cycle of oscillation. Before the gelation occurs, the sample starts as a low-viscosity liquid and the initial signal of torque is small. This is expressed by a phase angle near 90° ($\sin\delta \sim 1$, $\cos\delta \sim 0$). Thus, G' becomes zero and $G'' \sim G^*$. As the sample progresses towards the gel point, the phase angle δ grows, and consequently G' becomes measurable and increases. After the gelation point the loose ends and dangling chains, which were responsible for the viscous signal, become part of the elastic gel network. During the measurement of the time-dependent gel formation, this is represented by an increase in G' and decrease in G''. It is important to note that with very small phase angles the values of G'' become unreliable and should not be considered ($\sin\delta \sim 0$).

.

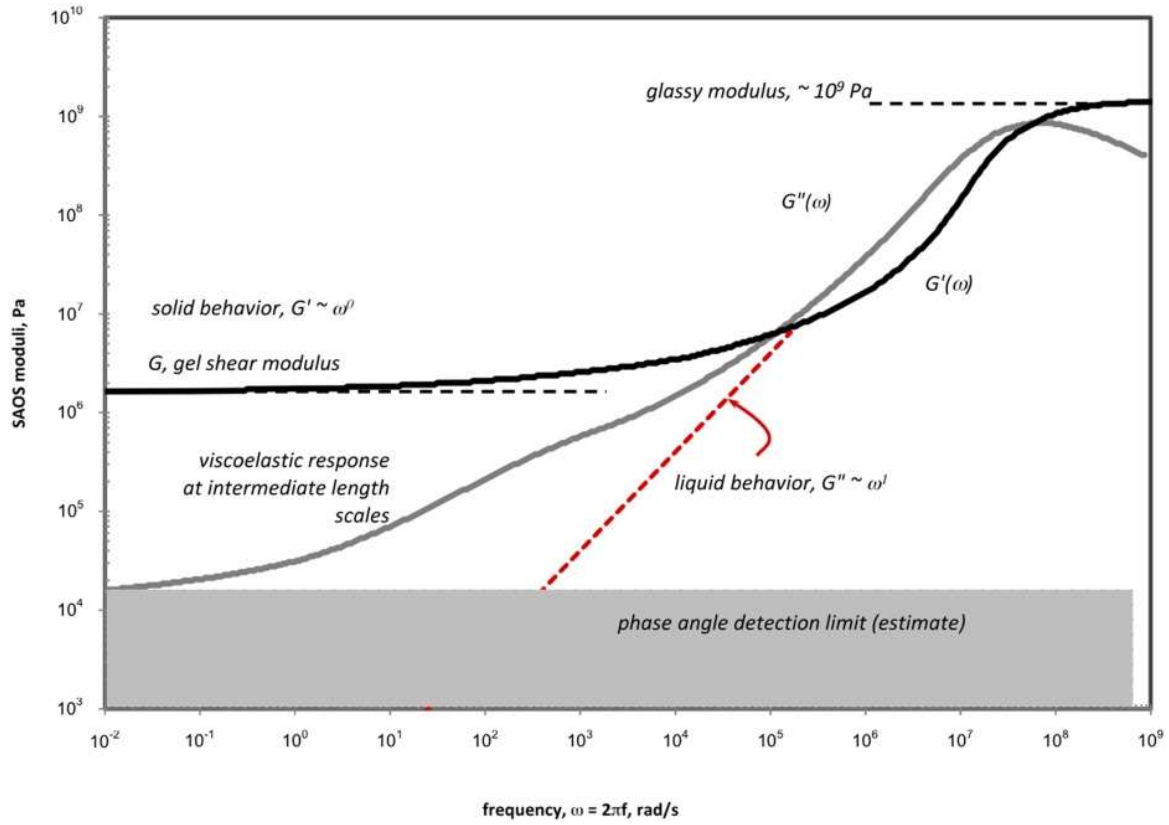

Figure 6 Typical linear-viscoelastic behavior of a crosslinked gel. Plotted are $\boldsymbol{G'}$ and $\boldsymbol{G''}$measured by small-amplitude oscillatory shear (SAOS) versus the frequency. At high frequencies, the glassy behavior of polymers is observed and at low frequencies $\boldsymbol{G'}$ approaches a plateau, the gel shear modulus. The transition of $\boldsymbol{G'}$ between these two plateaus characterizes the glass transition of the polymer. Reprint with permission from ref. [68]. Copyright 2013 Wiley Periodicals

In the linear-viscoelastic regime, which is determined by the strain- and frequency sweeps, the measured values can be used to deduce important properties of a hydrogel structure, such as degree of crosslinking, entanglement, glass transition, and more details of the chain architecture.[68] Figure 6 depicts a typical plot of the linear-viscoelastic behavior of a crosslinked gel. In summary, from the gelation point we can estimate how fast hydrogels form, from the storage modulus G' we receive information about the elasticity and stiffness of the material, and G'' describes the viscous character of the network. [69] Further information on the internal structure of the hydrogels can be obtained by relating the shear modulus to the number density of network units and thereby, get an estimated mesh size.[46]

2.2.4 Mesh size

Three-dimensional crosslinking of polymer chains results in a material consisting of the polymer, interspersed with open spaces called meshes. These meshes allow for water absorption and for diffusion of solutes small or flexible enough to penetrate the network structure. The sizes of these meshes typically range in the nanometer regime,[70, 71] although larger pores (up to several micrometer) can be achieved by various techniques, such as freeze-drying, use of porogens, or by gas formation.[72] Several methods exist to determine or estimate the mesh size, however, it is important to keep in mind that, owing to network heterogeneity and polymer polydispersity, most hydrogels have a range of mesh sizes. Especially with non-ideal network structures such as dangling chains or closed loops, which arise during the gelation process, a uniform distribution of mesh sizes is rarely achieved. Notably, a network with homogeneous mesh size can be obtained with the gelation of symmetrical tetrahedron-like macromonomers of the same size.[73]

There are a few direct methods to determine the mesh size, such as atomic force microscopy, confocal microscopy, electron microscopy, and small-angle X-ray scattering (SAXS).[74, 75] However, confocal microscopy is typically limited by the resolution (>1 μm), and electron microscopy, which enables very high resolution, typically alters the morphology of the hydrogel during sample preparation. As a result, most methods to determine the mesh size are indirect methods, for example following the diffusion of fluorescence-labeled diffusor molecules, or by using models that connect the mesh size to swelling behavior or to visco-elastic properties measured by rheology.[9]

Following the classical theory of rubber elasticity, which relates the mesh size ξ only to the shear modulus G, an estimation for a mesh size can be obtained from equation (9)), with the temperature T, the Avogadro constant N_{Av}, and the ideal gas constant R.[64, 76, 77]

$$\xi = \left(\frac{RT}{N_{Av}G}\right)^{1/3} \tag{9}$$

Following Peppas et al., the mesh size ξ is defined as seen in Equation (10).[78] Here, α is the elongation ratio of the polymer chain in any direction. For isotropically swollen hydrogels, it can be related to the polymer volume fraction by $\alpha = \nu_{2,s}^{-1/3}$.[62, 79]

$$\xi = \alpha \cdot \sqrt{r_0^2} = \nu_{2,s}^{-\frac{1}{3}} \cdot \sqrt{r_0^2} \tag{10}$$

Since the polymer volume fraction $\nu_{2,s}$ of the swollen hydrogel is determined by the ratio of the polymer volume to swollen hydrogel volume, we can roughly estimate it by the inverse mass swelling ratio q if the density of both water and our polymer is roughly 1 g/cm^3. The root-mean-square, unperturbated end-to-end distance between crosslinks $\sqrt{r_0^2}$ is given by Peppas et al. as $\sqrt{r_0^2} = l\sqrt{C_n N}$ and equation (10 becomes equation (11).[80] Here, l represents the average bond length of the polymer, C_n is the Flory characteristic ratio or rigidity factor, and N is the number of links per polymer chain and can be calculated by equation (12), where x is the number of bonds per monomer, $\overline{M_c}$ is the average molecular weight between crosslinks, and M_r is the molecular weight of a repeating unit. So finally, equation (13) can be used to determine the mesh size.

$$\xi = q^{1/3} \cdot l \cdot \sqrt{C_n N} \tag{11}$$

$$N = \frac{x\overline{M_c}}{M_r} \tag{12}$$

$$\xi = q^{1/3} \cdot l_{bond} \sqrt{3C_n \frac{M_C}{M_r}} \tag{13}$$

Even though these models give a good estimation for the mesh size and are easy to measure, a better understanding of the mesh size is obtained with particle-tracking techniques. They

probe the local microenvironment of hydrogels and a size cut-off is determined from an abrupt change in the transport behavior of tracer particles of different sizes.[81]

2.2.5 Diffusion and partition in Hydrogels

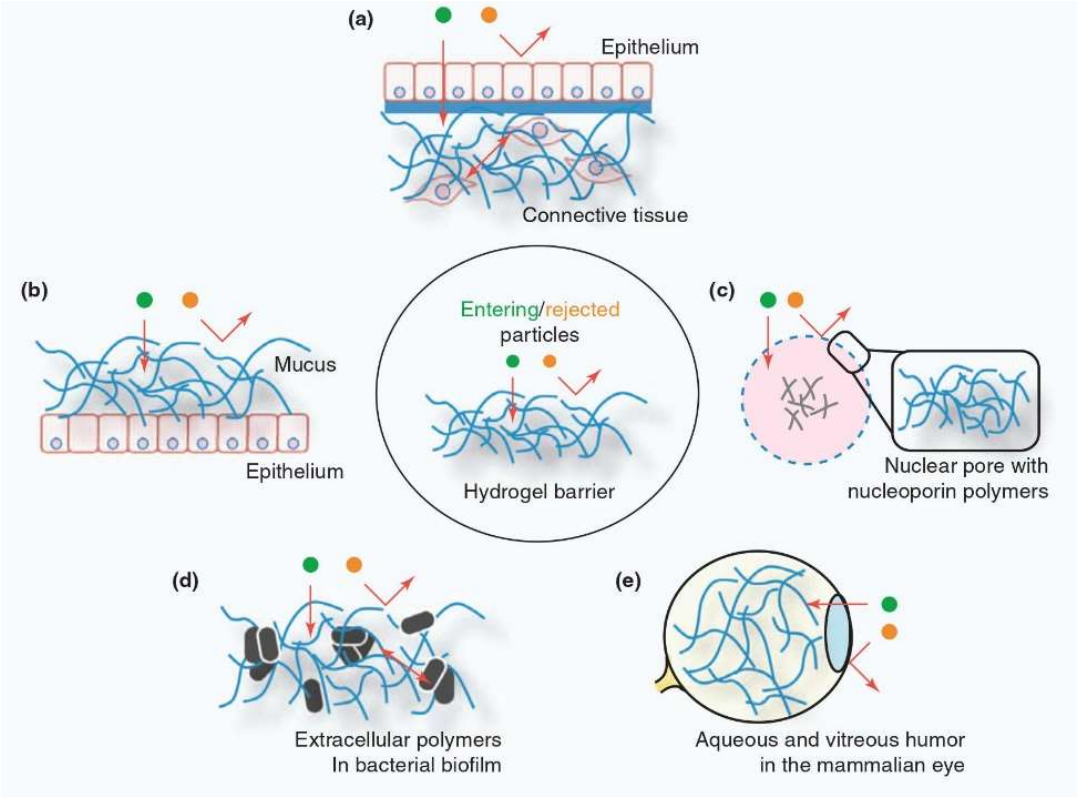

Figure 7 Overview of biologically relevant hydrogels that control the translocation of microscopic objects and act as selective permeability filters. They allow the passage of particular molecules (green) while rejecting others (orange). Depicted are the extracellular matrix (a), the mucus (b), a nuclear pore (c), a bacterial biofilm (d), and the vitreous humor in a mammalian eye (e). Reprinted with permission from ref. [81]. Copyright 2011 Elsevier Ltd.

Hydrogels do not only establish and regulate the mechanical properties in cells and tissues or serve as lubricants in joints or on epithelial cells; they can also serve as porous structures for embedding molecules or as selective barriers that control the exchange of molecules between separated compartments.[81] Some of the biologically relevant hydrogel barriers are depicted in Figure 7. It is important to analyze the properties of partitioning and diffusion to better understand the observed phenomena. The partition coefficient K is defined as the concentration of the solute in the gel divided by the concentration of the solute in the bathing solution at equilibrium.[82] It is a measure of how easily a solute can penetrate the network.

The diffusion coefficient or diffusivity, D, is defined by the Stokes-Einstein equation (c.f. equation (14)) and is dependent on Boltzmann's constant k_B, the temperature T, the viscosity η, and the radius of the diffusor r.[83]

$$D = \frac{k_B T}{6\pi\eta r} \tag{14}$$

The main hydrogel parameter that influences the diffusion coefficient involved in mass transfer is the mesh size. It is dependent on the molecular mass between adjacent crosslinks and the volume taken up by the polymer itself. The resulting mesh acts as a selective barrier with regard to the permeability of substances.[60, 84] The selectivity can simply be size-based, where the mesh size defines the molecular size cutoff. Or the permeability of a diffusor can depend on the interaction with the hydrogel surface. If there is an attraction, even solutes smaller than the mesh size can get trapped whereas larger ones without any interaction could pass. The size selectivity is more prominent for rigid and compact molecules like proteins than it is for flexible and random coiled diffusors like DNA strands, PEG or dextrans.[82]

There are several parameters to investigate in pursuit of understanding transport through hydrogels in the body like mucus or the ECM, such as pH alterations, salt concentration, additives, charged versus uncharged particles, or which part of the hydrogel is responsible for diffusion effects. Therefore, it is important to have an easily modifiable, fast, and reliable measuring platform. Diffusion measurements are done mostly with fluorescence-labeled solutes of known size. These solute's progression through the network is followed by fluorescence microscopy and evaluated by physical models. These models are based mainly on hydrodynamic effects, obstruction effects, free volume theory, or, in further advanced cases, on thermodynamic models.[85] One method is to follow the fluorescence recovery after photobleaching (FRAP), where a high-intensity laser bleaches the fluorescent dye on a small part of a diffusing species. The recovery of the fluorescence intensity happens through exchange of bleached with unbleached solutes and this process is driven by diffusion.[86] Alternatively, a hydrogel sheet can be incubated in a solution with fluorescence-labeled diffusors of different sizes. At selected time points, a gel sheet is removed from solution and the extent of penetration into the gel can be followed by confocal fluorescence microscopy.[87] These methods, however, do not continuously measure the fluorescence intensity, which is interesting in studying mass transport through biologically relevant hydrogel layers.[88]

2.3 Bioanalytical assays and biosensing

2.3.1 Definition

In a bioanalytical assay, a biological recognition element (bioprobe) is typically immobilized on a solid support (substrate) and specifically interacts with and sequesters a target molecule from solution. The device is termed a biosensor if the entire process of recognition and transduction into a measurable signal is performed in a self-contained device. Typically, however, in bioanalytical systems additional processing steps are required. The term "biosensor" was coined by Carl Kamman in 1977 but was only defined by IUPAC in 1997.[89] To qualify as a biosensor, a device must be "a self-contained integrated device, which is capable of providing specific quantitative or semi-quantitative analytical information using a biological recognition element […], which is retained in direct spatial contact with a transduction element. […]". Figure 8 shows a schematic representation of a biosensor. It starts with a sample, which can be obtained from a variety of biological sources. If the target is available to diffuse freely, the collected analyte (such as urine, saliva, or blood samples) is used directly as the analyte and brought into contact with the substrate. In general, however, the target must be extracted, enriched, and potentially purified before it is applied to the biosensing device. The biological counterpart of the target, the probe molecules (nucleic acids, proteins, antibodies, enzymes, cells etc.) must be immobilized on a substrate (a solid surface, e.g. glass, metal, microbeads, hydrogels, etc.). The interaction of the target and the probe are registered physicochemically and then transduced into a detectable signal, which may then be amplified depending on the detection method. Finally, the results are processed

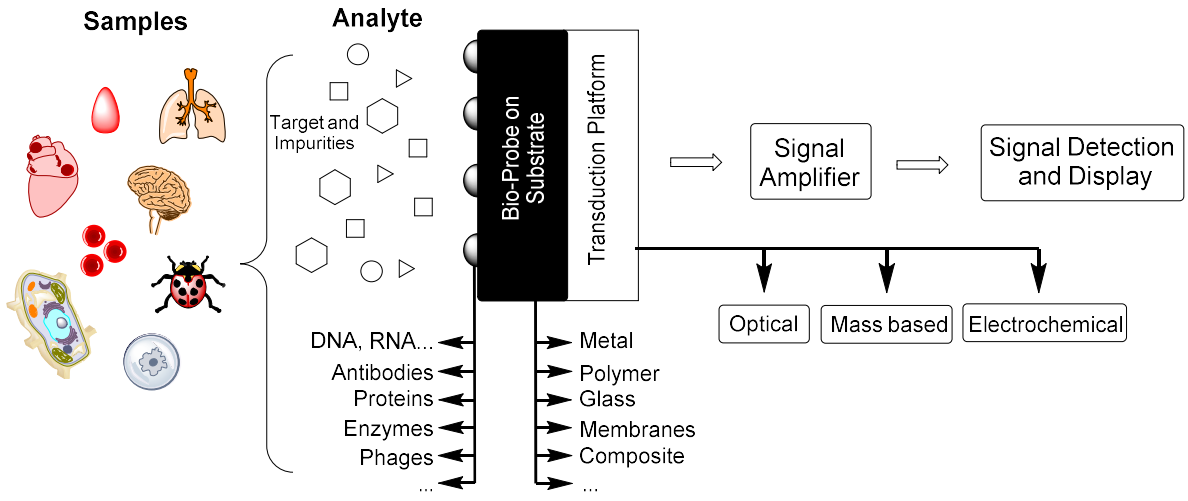

Figure 8 Schematic representation of a biosensor.

and displayed. Examples of commonly used biosensors include glucose monitors for diabetes patients and pregnancy tests, which detect human chorionic gonadotropin in urine. In addition to healthcare, applications arise in environmental field monitoring, food analysis, and crime detection.[1]

2.3.2 Biochemical fundamentals

Any biospecific interaction can be used for the construction of a biosensor. The most prominent examples are substrate-specific interactions of enzymes, sequence-specific hybridization of oligonucleotides (DNA and RNA based), antibody-antigen interaction, and cell-based or cellular-structure-based processes. The more specific this affinity interaction between bioprobe and analyte, the better the **selectivity** of the entire sensor. This affects the reliability of the results and influences sample preparation and assay performance.[90] Furthermore, the technique and the material onto which (or by which) the probe is immobilized, can influence the response time, the dynamic range, and thereby the **sensitivity** of biosensors.[91] This is due to the fact that biological processes are influenced by alterations of the environmental conditions. These influences can have an impact on the stability of the biomolecule. Besides the right biological detection setup, the right transduction platform determines the effectiveness of the signal processing and the biosensor's output type. These peculiarities decisively determine the limits of applicability of biosensors.[92] The biochemical fundamentals will be discussed for antibodies in immunoassays and oligonucleotides in DNA hybridization biosensors.

Antibodies in Immunoassays. Immunoassays are based on antigen-antibody or antibody-antibody interaction. They gained popularity because of their impressively low detection limit and high selectivity. These traits, combined with relatively easy access to a number of antibodies covering an increasing number of important analytes, makes them an important tool in biomedical applications.[93] Antibodies (Ab), also known as immunoglobulin (Ig), are large proteins that are produced by specialized B lymphocyte cells of the immune system. They are formed as a response to the presence of antigens, which are any kind of molecule detected as foreign by the host. There are different types of antibodies; however, immunoglobulin G (IgG) is the one most important for immune response. All IgG-type antibodies have the same general arrangement (see Figure 9, left), with only the antigen

binding site being specific for each antigen. They are Y-shaped and composed of four polypeptide chains with an overall molecular weight of ~150 kDa.[94] The interaction between the epitope of the antigen and the antibody is based on size, shape, and chemical compatibility within the interface. The high specificity paired with high affinity constants (typically they range between 10^9 and 10^{11} M^{-1})[95] makes antibodies an ideal biorecognition element. When they are used in a biosensor and are immobilized on a solid support, the recognition sites must be exposed to the target molecules. This is connected to the amount and prientation of the immobilized probe. Too few gives an insufficient signal but if they are too densely packed, steric hindrance impedes with the recognition process (see Figure 9, right).[96]

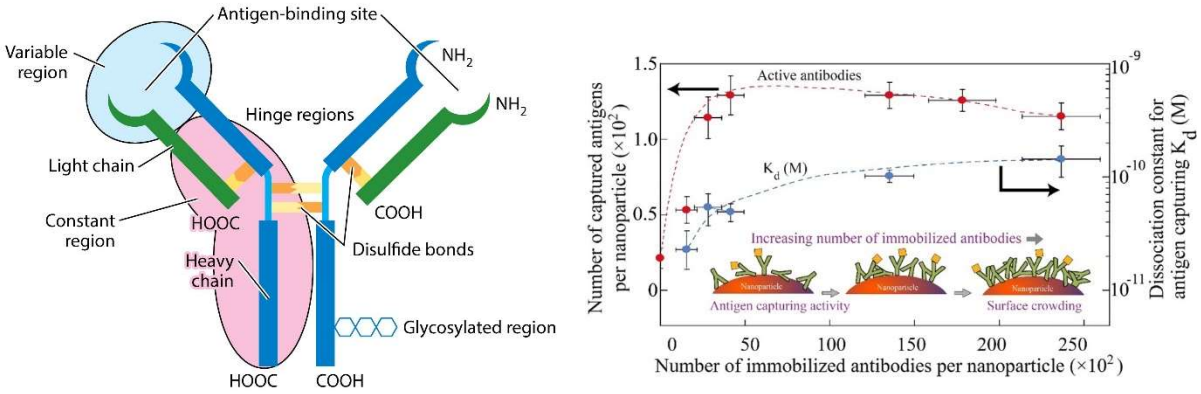

Figure 9 Left: Schematic of an antibody with important regions highlighted. Modified and reprinted with permission from ref. [97]. Copyright 2017 Annual Reviews **Right:** Crowding effect shown for antibodies on a nanoparticle. The data show that the immunoassay response scales with the number of active antibodies, increasing initially and saturating at higher antibody densities. Reprinted with permission from ref. [96]. Copyright 2014 American Chemical Society

More recently, instead of the whole antibody, smaller fragments of antibody-like molecules have been used. They show a similar high affinity for their target antibody but can diffuse more easily, penetrate deeper through tissue, and reach smaller destinations than full-sized antibodies due to their smaller size.[98, 99] Next to single chain-variable fragments (scF_v) and third-generation molecules, which are single-domain antibodies (D_{ab}), the most common and thoroughly studied class of antibody agents are Fab fragments (antigen binding fragments).[100] They are obtained either by recombinant synthesis or by proteolytic cleavage of the parent antibody. Before the Fab fragment is obtained, the disulfide bridge from the hinge region is broken up by reduction. The resulting C-terminus thiols can then be used to immobilize the Fab fragment in an oriented fashion, or for labeling with dyes or enzymes.[101]

A full-sized antibody has estimated molecular dimensions of 15 x 7 x 3.5 nm, which is, despite its flexibility, much larger than a Fab fragment of 4 x 2.5 x 3.5 nm.[102, 103] In biosensing, Fab fragments can be used as the secondary antibody, where they are highly advantageous because they do not lack specificity for the antigen, but are much smaller, and therefore, can accumulate more densely due to less steric hindrance. The higher amount of labeled biomolecule produces a higher signal intensity, lowers the limit of detection, and improves the signal-to-noise ratio.[104]

Radioimmunoassays with radiolabeling were the primary means of detecting successful antibody binding until the so-called enzyme-linked immunosorbent assay (ELISA) was introduced in 1971; ELISA is now the standard method to detect and quantify antigens or antibodies.[105, 106] Alternatively, the presence of an antigen can be visualized by a fluorescence-labeled antibody or Fab fragment. Fluorescent dyes are especially favorable because they are detectable in small amounts, and, unlike enzyme-based assays, require no additional step of substrate conversion. Therefore, the tests are less time consuming and fewer steps are necessary.[104]

Oligonucleotides in DNA hybridization biosensors. Oligonucleotides are short DNA or RNA single strands (typically 20-40 base pairs), that form a double helix with their complementary strand, via hybridization. If one strand is immobilized on a surface and incubated with the analyte, hybridization will take place only between strands of complementary sequences, based on the specific pairing of adenine with thymine, and guanine with cytosine by hydrogen bonds (see Figure 10). The successful hybridization on the substrate is transduced into a measurable signal, allowing conclusions to be drawn as to which target was present in the investigated analyte. Apart from the genetic, sequence-specific detection of targets, oligonucleotide-based biosensors can make use of aptamers. Aptamers are short oligonucleotides with a strong affinity towards small molecules, heavy metals, peptides, or proteins.[107, 108] This detection is generally based on charges and hydrophobic interaction between the oligonucleotide and the target molecule.

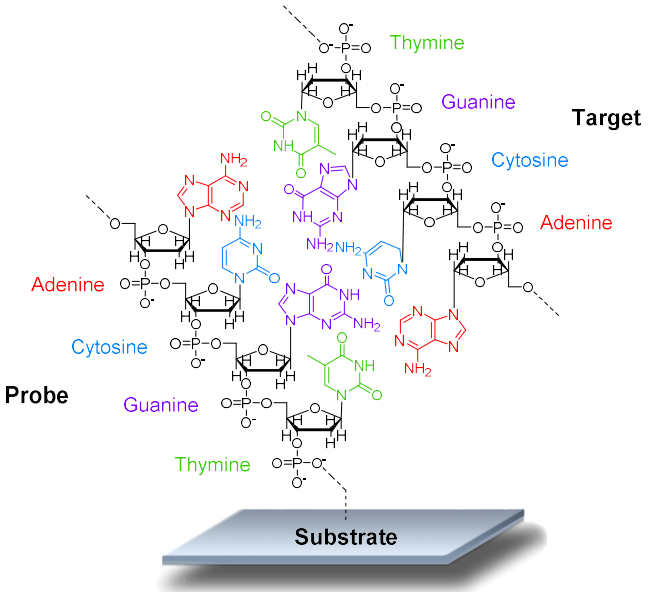

Figure 10 Example for an oligonucleotide sequence (DNA) and the specific base pairing during hybridization.

Oligonucleotide-based biosensors are used in a wide range of applications, such as pharmacogenomics, infection diagnosis, environmental monitoring, detecting microorganism contaminants in food and beverages, and for the determination of genetic risk factors.[109] They are widely used, because of their high specificity, wide range of applicability and stability. However, to achieve good performance, the DNA fragments must be immobilized in a way that keeps them reactive, stable, and most importantly accessible by the target. Therefore, the immobilized strand must be immobilized in the right orientation: orthogonal to the surface and immersed in analyte. Finally, to get an output, the successful hybridization between probe and target strands must be detectable. This can be achieved, for example, by indicators that do not bind to single strands, but prefer to bind to DNA duplexes or have detectable changes upon double strand formation. For example, SYBR Green I is a fluorescence dye, which emits weak fluorescence when it is in a free state, but its fluorescence intensity is substantially increased when it binds to double helix groove regions in DNA.[110] Alternatively, it was observed that single- and double-stranded DNA have different susceptibility to adsorb to citrate gold nanoparticles, and there are antibodies which specifically bind to the double helix.[111, 112] Lastly, for electrochemical detection intercalating molecules can be used, e.g. ferrocenyl naphthalene diimide.[113] For most detection methods, however, the respective label must be introduced to the target strands during preconditioning procedures.

Due to their charged backbone, charge repulsion between strands is a common issue in the field of biosensing, where the probe strand is immobilized on a surface and overcrowding can become an issue. That is why it is important to find a balance between immobilizing enough oligonucleotides to get a detectable signal and immobilizing few enough, to ensure the accessibility for each of the strands.[114]

2.3.3 Substrates and immobilization methods

The probe molecule in almost all bioanalytical assays must be immobilized onto a substrate, for the purpose of easy separation, incubation, washing, and finally detection. There are several methods to immobilize the probe molecule onto various base materials, called substrates. However, not all substrates work with all detection techniques, and not all immobilization methods work on all substrates. Fortunately, there are many methods and techniques to choose from. Some of them will be discussed in more detail.

Substrate Functionalization. Substrates can come in multiple forms and shapes. Commonly used materials are 96-well plates, glass slides, microbeads (fluorescent or magnetic or both), rods, chips or cups. The initial choice for the right substrate is mainly dependent on the mode of detection. Once the right platform is decided, substrates usually come in a variety of base materials (glass, metal, polymer, or composites). They can be used **unfunctionalized** if the material itself interacts with the bioprobe. However, for some applications special functionalities are needed, and there are several methods to introduce them. One straightforward approach is the use of plasma treatment, which eliminates surface contamination and inserts chemically reactive functional groups, and can also be used to change wettability, adhesion characteristics, and biocompatibility of the base material.[115]

Alternatively, substrates can be functionalized with a **monolayer** of functional groups. In this case, linkers are used that carry a substrate binding functionality on one side and a bioprobe reactive group on the other side. If a larger distance between substrate and linker is desired, longer linear chains can be implemented. This is supposed to make the bio reactive group more easily accessible to the biomolecule of interest. Prominent examples are self-assembled monolayers (SAMs) on gold or the silanization of glass surfaces, since silanes with diverse functional groups are readily available. However, the probe coverage in this

introduced monolayer is often not sufficient to create a detectable signal. To increase the number of functional groups available on a substrate, **polymer brushes** or **multivalent linkers** like dendrimers, hyperbranched polymers, or starshaped polymers are introduced.[116, 117] Therefore, a polymer is either grafted to or grafted from the surface. With every monomer a new functional group is introduced for the subsequent immobilization of a biomolecule. Although the introduction of multifunctional polymers greatly enhances the number of functional groups, not all these groups are accessible, especially if the biomolecule of interest is rather large. This is because these functional groups are densely packed. It is reported for poly(methyl methacrylate) (PMMA) beads that this method can create a high density of up to 50 nmol/cm^2 accessible COOH groups.[118] Additionally, for coupling reactions at the two-dimensional interface, the amount of effective collisions is reduced due to restrictions in translational and rotational degrees of freedom. Therefore, coupling reactions to surfaces show lower reaction rate constants compared to the respective reaction in solution and have lower conversions. It was found that surface DNA hybridization is suppressed 20- to 40-fold in comparison with bulk hybridization, probably owing to interactions between analyte and substrate.[119]

This is something which can be prevented by the entrapment of the bioprobe into a **hydrogel matrix**. In the solution-like environment, the probes stay immobilized, but the affinity interactions are less restricted. This method increases the distance between the surface and the bioprobe and increases the surface area for the immobilization of probes.[120] Instead of using the hydrogel simply as an immobilizing matrix, it can be used as the actual substrate or substrate coating, or even function as the sensor or transducer platform. In all of these cases hydrogels are very promising, due to their exceptional physicochemical, mechanical, electrical, and optical properties.

Immobilization of biomolecules – Methods. Immobilization engineering is a mandatory step in the development of a bioanalytical assay. If the immobilization is not done correctly, the bio-probes may lose all or part of their biological activity, which would impede subsequent detection steps.[102] The immobilization of biomolecules can occur via **adsorptive** forces (Figure 11, a), such as electrostatic interactions, H-bond formation, hydrophobic interactions, or dispersive interactions. The advantage is that the biomolecules can be used without previous modification, which eliminates additional steps. For example, electrostatic interactions can be used for the immobilization of oligonucleotides (short DNA strands),

because their phosphate backbone carries a negative charge. For the counterpart to the oligonucleotides, a positively charged surface is needed, which can be achieved by coating the surface with positively charged amine groups. DNA surface adsorption and coverage can be tuned by changing the pH and the ionic strength of the solution. However, a huge drawback is that the DNA strand most likely will attach in a flat-on orientation, causing conformational hindrance for the hybridization. In the case of proteins, the isoelectric point can be used to bring them close to a surface by adjusting the pH.[121] Adsorptive immobilization is widely used on a number of surfaces such as polymers, glass, membranes (nitrocellulose and nylon) or metal oxides.[122] For example, polystyrene is a prominent example in the immobilization of proteins, due to its high affinity and strong adsorption ability towards proteins, its excellent biocompatibility, lack of toxicity, and chemical inertness in biological processes. However, adsorptive binding is only applicable, if the interaction is strong enough to sustain washing, drying and detection steps. In any case, this method binds the biomolecules nonspecifically to the substrate and the proximity of the biomolecule to the surface can impact the structure and lower the activity of the bioprobe.[123] It is also difficult to control the coverage of the surface and reproducibility can be a problem.

An alternative approach is to couple the biomolecule **covalently** (Figure 11, b and c) to a surface. In this method, a chemical motive, which is naturally part of the biomolecule can be used directly. For example, thiols from the amino acid cysteine can self-assemble onto gold surfaces, undergo disulfide exchange, and react with alkyl halides or via Michael addition.[124] Amines occur as heterocyclic amines in the DNA bases purin and pyrimidine and as primary amine in the amino acid lysine. The primary amine is targeted especially often, due to the prevalence of methods for selectively targeting them. They will react with epoxides, sulfonyl chlorides, isocyanates, activated esters or aldehydes. Finally, the phenol moiety of tyrosine as a natural amino acid can be chemically crosslinked, or acid functionalities (from aspartic and glutamic acid) can be addressed by nucleophilic surfaces.[125] The distance between surface and coupled probe should be adjusted and optimized. As an example, it was found that a directly conjugated antibody often interferes with antigen detection due to steric hindrance and limited mobility. Additionally, denaturation was shown to increase if antibodies were physically adsorbed or covalently attached to solid supports. This can be improved by introducing a long and flexible PEG linker, which improves the accessibility of the immobilized bioprobe and can prevent protein denaturation.[126] Furthermore, bioorthogonal functional groups can be introduced. This is

advantageous if a directed immobilization is desired and nonspecific binding between probe and substrate becomes a problem. It greatly enhances control over the adsorption processes and reduces the interference of non-target-specific interactions.

Another very common method is the immobilization of biomolecules based on **secondary interactions** (Figure 11, d), such as the (strept)avidin-biotin interaction. This interaction is one of the strongest non-covalent interactions known. A high dissociation constant and the consequent high-temperature stability even allows for its use in nucleic acid detection under polymerase chain reaction (PCR) conditions.[127] There are several methods to couple biotin specifically to biomolecules. The biotinylated probe is then captured onto a streptavidin coated surface at high density in a directed orientation. Since a flexible linker can be used between probe and biotin, which improves the accessibility and binding capacity, another advantage is presented without the need for an additional step.

Finally, biomolecules can be immobilized by **entrapment into a hydrogel** (Figure 11, e). Here, the co-immobilization of probe and matrix is performed in a single step, and probes are kept inside the matrix simply by size exclusion. Since the probe is not chemically linked to a substrate, the affinity interaction between probe and target is more similar to the interaction in solution. The hydrogel itself can be co-immobilized onto the substrate by chemical modification.

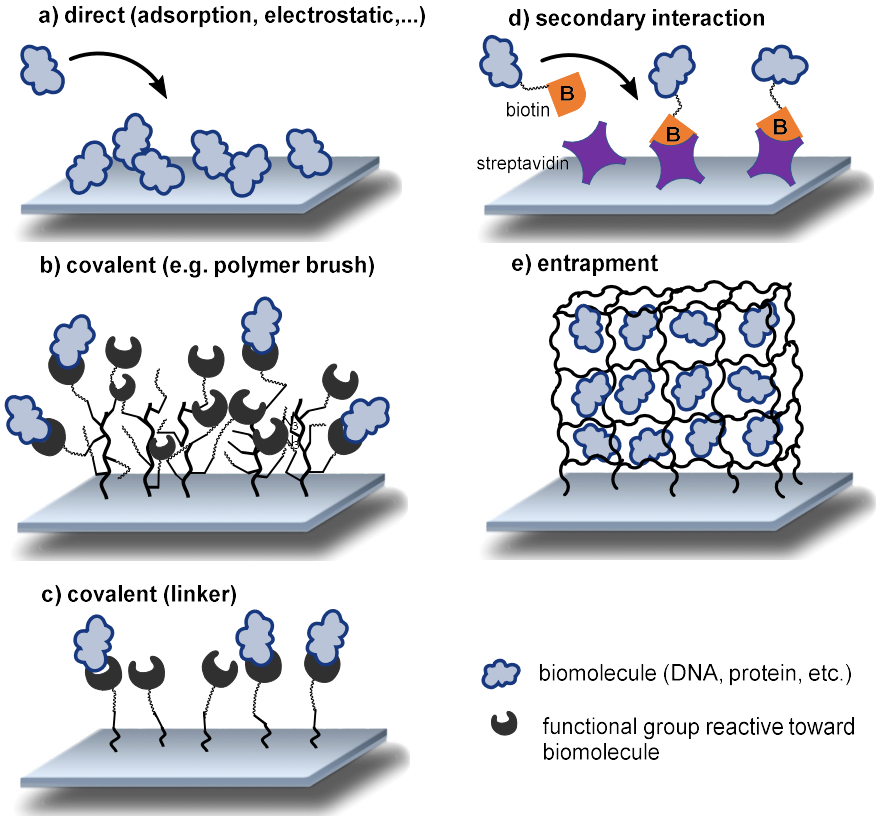

Figure 11 Illustration of common biomolecule immobilization methods.

Surface features. After immobilization of the probe onto the respective substrate, there are essentially two different implementations. In the first, the bioprobe is immobilized on a stationary surface and the target has to diffuse towards the surface during incubation. This is the case for the use of traditional microtiter plates. The second implementation is to immobilize the bioprobe on nano- or microparticles. As a result, both the substrate (containing the immobilized probe) and the target are immersed in solution. These solution-based assays enhance and accelerate the binding kinetics and capture efficiency due to superior mass transport of the target towards the probe on the surface.[128] Additionally, the nano- and microparticle-based assays have a higher surface-to-volume ratio, which allows for better capture efficiency.

After successful affinity interaction, the regeneration of the surface is an option that has the benefit of reduced cost and offers the ability to monitor changes in concentration over time without changing the setup. It is achieved by overcoming and reversing the attraction forces between probe and target. This is usually done with relatively harsh conditions such as heat, addition of urea, or highly basic buffers.[129] However, the structure and binding capability of the immobilized probe itself as well as the connection to the surface may not be

destroyed. This comprises a big challenge, and the surface regeneration results mostly in a reduced binding affinity, increased unspecific binding, and thus lower sensitivity.[128, 129]

Finally, with almost all methods, reduction of non-specific binding to the surface is important, especially when using naturally occurring chemistry (like amines or carboxylic acids). Methods for the passivation of a surface include using bovine serum albumin (BSA), ethanolamine, or hydrophilic macromolecules such as poly(hydroxyethyl methacrylate), poly(acrylamide), and poly(ethylene glycol).[128]

2.3.4 Detection methods

Having addressed the biochemical fundamentals regarding the affinity interactions between probe and target molecules and how to immobilize them onto surfaces, we now turn to converting the successful pairing into a measurable signal. As depicted in Figure 12 on the example of an antibody, there are different principal formats for affinity interactions:

a) There are no labels, and either the presence of the target is detected by mass per quartz crystal microbalance (QCM) or electromagnetic piezoelectric acoustic sensors (EMPAS), or changes in refractive index are measured by surface plasmon resonance (SPR).

b) Alternatively, the presence of the target is registered by a secondary affinity interaction that carries a label. Depending on the label, it is detected by electrodes, UV, IR, or fluorescence.

c) If this label is an enzyme, an additional step is introduced, in which a colorless substrate is converted into a colorful product.

d) If the preconditioning process allows it, the target can directly be tagged with a label.

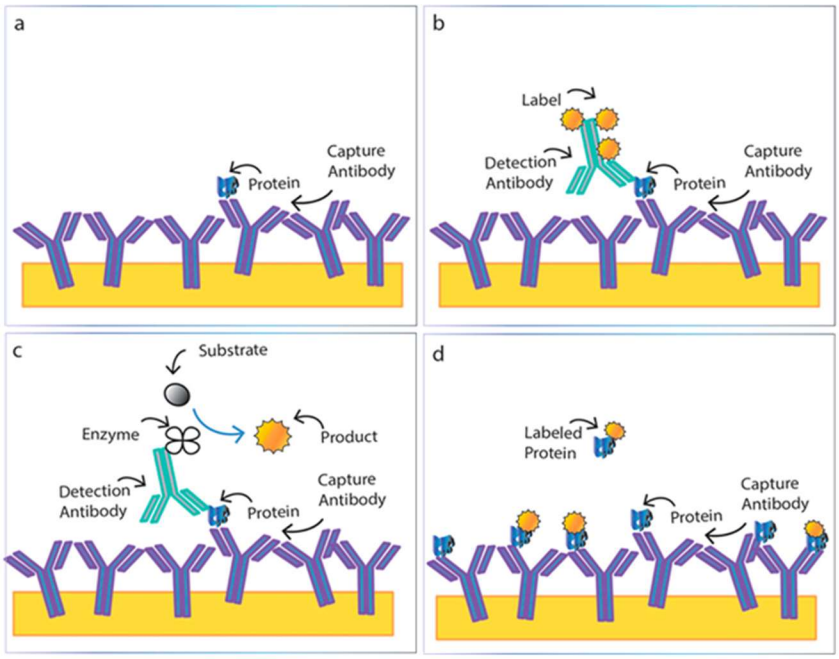

Figure 12 Detection formats of heterogeneous assays exemplified on an antibody. The same applies to other biomolecules. Reprinted and modified with permission from ref.[128]. Copyright 2019 American Chemical Society

Next to luminescence labelling, fluorescence labelling is the most common approach in the field of optical detection-based biosensors due to the high sensitivity, suitability toward a quantitative analysis, and fairly large dynamic range.[130] Also, fluorescence labeling allows for two or more samples of different colors to be detected in parallel. There is a wide variety of both chemical and biological methods for labeling biomolecules.[131] For DNA and RNA functionalization, the dyes can be incorporated during their synthesis, by using one fluorescently tagged primer oligonucleotide during DNA amplification by polymer chain reaction (PCR).[132] Alternatively, enzymatic ligation locates the dye in a more specific and directed fashion. Labels can also be introduced indirectly, by incorporating a biotinylated nucleotide, which is subsequently stained with fluorescence-labeled streptavidin.[133]

There are several ways to use the introduced fluorescence labels in an analytical assay. Firstly, the target can be labeled so that an increase in intensity reflects the amount of target. Secondly, competitive binding can be used. Here, a labeled marker interacts with the probe on a substrate. Upon exposure to the analyte, which contains the unlabeled target with a higher binding affinity towards the probe, the labeled biomolecule dissociates from the surface and the resulting fluorescence intensity is detected in solution.[134] Thirdly, the probe

can carry a fluorophore and the target a quencher, which means positive interaction will result in a decrease of intensity. This is especially advantageous if background fluorescence of the solution interferes with the assay.

2.3.5 Multiplex assays

The informative value of a parameter analysis can be expanded and improved by parallel recording of a larger amount of data from one single sample - the so-called multiparameter analysis or multiligand analysis. If these several targets are investigated from a single analyte in a single run, this assay is termed a multiplex assay.[135] Especially since the decoding of the human genome, the quest to obtain more molecular information from smaller samples is intensifying. The progression from conventional assays to multiplex assays increases the analytical throughput and thereby results in a higher output-to-input ratio. This makes multiplex assays a vital feature in many areas of molecular and clinical diagnostics, as well as for the detection of food- and beverage-associated microorganisms.[136] Predisposition to many diseases like Alzheimer's disease, cardiovascular and metabolic disorders, autoimmune diseases, and cancer, as well as their cause and progression, often depend on several biological markers.[135, 137, 138] If these markers are known, they can be tested simultaneously in one sample by a multiplex assay setup. Thus, multiplex analyses can be more effective in terms of time and cost in comparison to the conventional single-target assays.[139]

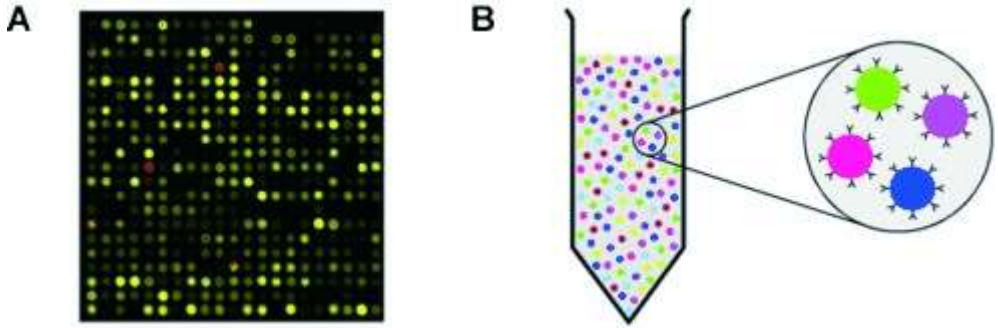

Figure 13 A) A conventional microarray consists of a two-dimensional grid of recognintion molecules and the identity of the recognition molecule is known from its location on the grid. B) A suspension array is composed of recognition molecules attached to encoded particles. In this image the code is based on different colors. Reprint from ref. [135]. Copyright 2006 WILEY-VCH Verlag GmbH & Co. KGaA, Weinheim

The most common multiplex assays are **microarrays** (DNA/protein chips) and **microbead-based arrays** (suspension arrays), depicted in Figure 13. In a microarray format, spatially separated spots are arranged in a grid onto a solid support, and it is possible to immobilize a different target-specific capture molecule (probe) in each of the spots. The identity of the bioprobe at each xy-position is predetermined. Consequently, from only one sample a huge number of targets can be investigated simultaneously. Such arrays provide high sensitivity and very high multiplexing capacity.[133] However, for this degree of miniaturization and multiplexing, arrays are manufactured by electrolithography or piezoelectric printing technology, which are complex procedures and only suitable for special fields of use. Additionally, microarrays struggle with cross-reactivity, background noise, and bad accessibility due to surface interaction.

A microarray codes the different probes by placing them at a specific xy-position. In microbead-based multiplex assays, however, the multiplexity relies on specifically encoded micrometer-sized beads. Each uniquely encoded particle population is functionalized with a specific bioprobe. There are several ways to encode microparticles, including physical, magnetic, thermal and graphical (barcode) properties.[135] Most common is optical encoding with fluorescent dyes, as well as size coding. Color coding means that a different dye or ratio of dyes is incorporated into the beads to make them distinguishable. Size coding means that the microbeads have distinct diameters, typically ranging between 0.5 and 500 µm, which are distinguishable by the detection platform.[140, 141] To obtain a multiplex detection, each of the bioprobes of interest is coupled to a differently coded microbead population. One bead population shares the same color and/or size but is different from the other populations used in the same assay. Then a mixture of bioprobes immobilized on their distinct bead population is suspended in the analyte solution, and affinity interaction between probe and target will proceed. A successful probe-target binding event is visualized by a separate signal, and finally, successful binding is connected invariably to the discrete microbead population. See Figure 14 for a schematic illustration of such a bead-based assay. The readout is often done by a flow cytometer, an instrument that measures the fluorescence and size of cells or microspheres in suspension as they flow past a sensing point.[142] Apart from flow cytometry, the detection and evaluation of multiplex microbead-based assays can be done with the help of a fluorescence microscope and appropriate software such as VideoScan.[143, 144] With this software, the detection, quantification and assignment are performed fully automatically. In a first step, the size and fluorescence of the microbeads are scanned, analyzed, and then

assigned to a microbead population with a known immobilized bioprobe. After incubation with the target analyte, the affinity interaction of probe and target occurs on the surface of the microbeads. They are labeled with a fluorescent dye of different wavelength, and thus the successful binding event can be analyzed by following the fluorescence intensity in the corona of the microbead. The multiplexicity of this kind of test is limited by the resolution and accuracy of the fluorescence microscope. Good results were obtained with up to 18 populations of microbeads (18-plex). Additionally, the VideoScan approach enables the stationary investigation of the microbead corona and therefore allows for kinetic studies and quantification of biological binding events.[145]

The choice of multiplex assay depends on the needs of the specific application. In planar microarrays, the quality of the data is limited by variations in performance between different arrays and the influence of surface-related interferences. The quality of data provided by suspension arrays is much higher, but the amount of molecular information is limited by the number of codes that can be distinguished in the same sample [135]

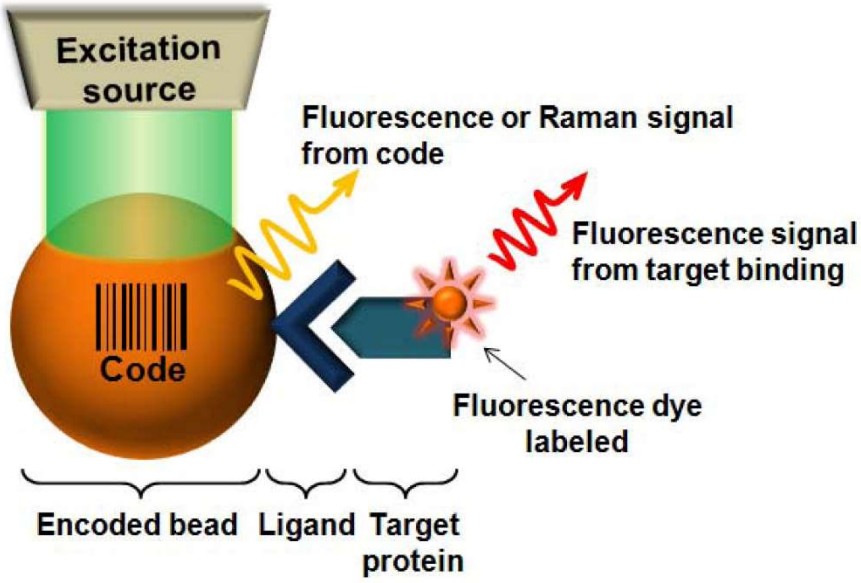

Figure 14 Schematic illustration of principle of a bead-based assay. Reprinted with permission from ref. [146]. Copyright 2012 MDPI.

2.3.6 Hydrogels in biosensing

Compared to two-dimensional and polymer brush functionalized planar surfaces, the three-dimensional nature of hydrogels confers several advantages in the fields of biosensing and bioanalytical systems. The hydrogel allows for the accommodation of larger amounts of recognition elements and provides a highly aqueous and biocompatible microenvironment. This more natural setting increases the stability of biomolecules and preserves their functionality, which is a crucial property for feasibility, specificity, and sensitivity of a biosensor.[147] The hydrogel itself can serve additional purposes, such as separating the target from other molecules in a sample.[6] There are essentially three different functions a hydrogel can adopt in the context of biosensing. They act either as the matrix for biomolecule immobilization, as the substrate material itself, or as a target-responsive transducer. The first two cases are discussed in more detail.

Hydrogels as matrices for biomolecule immobilization. Due to their porous structure, hydrogels increase the surface area of the material, allowing the immobilization of ligands ranging from small molecules to proteins and even cells. The highly hydrated structure resembles biological tissue; this makes hydrogels optimal for biological interactions and provides an ideal environment for probe molecules to be retained on the substrate. If the probes are entrapped inside the matrix as well as on top of the matrix, they are kept comfortably in the soft and flexible network, are less affected by surface interactions, and can maintain their biological activity.[5] Another outstanding feature of hydrogels as an immobilization matrix is the reduction or even prevention of unspecific binding. This is attributed to the hydrogel creating a solution-like environment in which biomolecules that are not chemically addressed will not bind to the surface. In 1990 it was found that a dextran coating showed great performance in SPR based techniques. A gold chip was coated with the dextran hydrogel, and the more flexibly bound antibodies showed superior performance to antibodies directly coupled to a solid support.[121] In a flow-through electrochemical sensor, super-porous agarose gel was used to immobilize the signal producing enzyme in larger amounts. This increased the signal intensity by a factor of more than five while retaining good flow properties.[148] As an example for a synthetic hydrogel, polyacrylamide based gel pads were used in immunoassays for their high capacity support, low nonspecific binding, and low background fluorescence.[149]

Hydrogels as a wearable device. Health monitoring is of particular importance for many diseases. If the monitoring can be done continuously and at home, this is a great relief on the health care system and increases the convenience for the patient. Personalized continuous health monitoring not only has logistical advantages but can also drive greater adoption and acceptance by patients. This holds true for simple diagnostic devices for measuring the temperature, blood pressure, or pH, for example, but is of even greater importance for measuring and monitoring glucose, hormones, lactate, or alcohol.[150] Such wearable devices must be directly attached to the system of interest, either externally (e.g. on skin) or internally (e.g. on soft tissue) and deliver accurate, reliable, and real-time measurement of physiological parameters or biomarkers (see Figure 15). The goal of these devices is to satisfy the demands of end-users in self- or ambulatory testing rather than requiring complex results.[151] Hydrogels have emerged as excellent candidates for such applications due to their mechanical flexibility, biocompatibility, and powerful sensory capacity.[152] For example, Lin et al. developed a contact lens based on hydroxyethylmethacrylat (HEMA). The hydrogel contains boronic acid, and upon exposure to glucose the boronic acid crosslinks break up and the lens swells. More glucose leads to more swelling, and the detection is performed with a smart phone imaging program.[153] As a wearable device on skin, a flexible silk fibroin patch with encapsulated enzyme served as substrate for a conducting polymer, which is photo-crosslinked on top. This flexible and biodegradable skin-like patch serves as a free-standing electronic device. If implanted, it could even serve as a platform for an “implant and forget” sensor, due to its biodegradability.[154, 155]

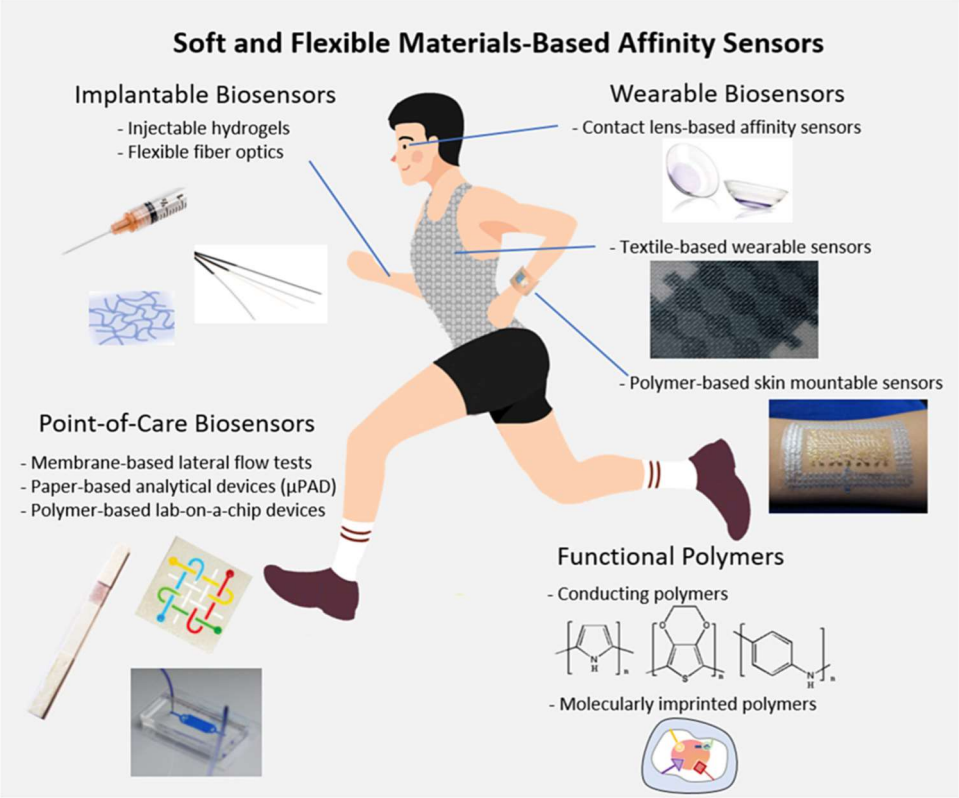

Figure 15 Schematic illustration summarizing applications of various soft and flexible materials used for the development of affinity biosensors ranging from point-of-care (PoC) tests, wearable biosensors and implantable affinity biosensors. Reprinted with permission from ref. [150]. Copyright 2019 Elsevier Inc.

3 Scientific goals

The use of hydrogels in the field of biosensing offers many advantages over monolayer approaches. The three-dimensional matrix greatly enhances the surface area, both as a coating and as an entrapment matrix. Moreover, hydrogels are known to be biocompatible and they offer a wide range of possibilities for modification such as tuning the mechanical properties, adjusting the swelling behavior, and introducing chemical functionalities. Regarding the immobilization onto surfaces, we investigated a bioorthogonal polyether polyol-based hydrogel for the non-covalent and covalent entrapment of proteins and an oligonucleotide (see Figure 16, Project 1). The goal was to create a stable biosensor with high immobilization efficiency, reduced nonspecific binding, and increased signal intensity. All of these being important features for a high-performing biosensor. This goal should be achievable by a hydrogel that is based on polyethylene glycol (PEG) and hyperbranched polyglycerol (hPG), which are bioinert and have several options for modification. PEG is a thoroughly investigated, linear, and hydrophilic polymer, and it was crosslinked with hPG to form a hydrogel. These compounds create a solution-like environment with a high surface area, which should enable the encapsulated biomolecules to remain accessible and immobilized after hydrogel formation.

In the second project, the hydrogel's ability to encapsulate larger objects was then applied to micrometer-sized beads. The objective was to place separated populations of beads into different layers and thereby increase the degree of multiplexity by the number of layers. In such a multiplex assay, the hydrogel would also work as a size-selective barrier, filtering the target molecules by size and thus directing them into their respective detection layers.

The size selectivity through the pores of hydrogels is often used empirically. In the third project, however, we aimed to develop an experimental setup to enable us to follow the diffusion of labeled solutes through the meshes of different hydrogels. Such a setup should allow us to determine the molecular weight cutoff and the energy barrier for mass transport through hydrogels.

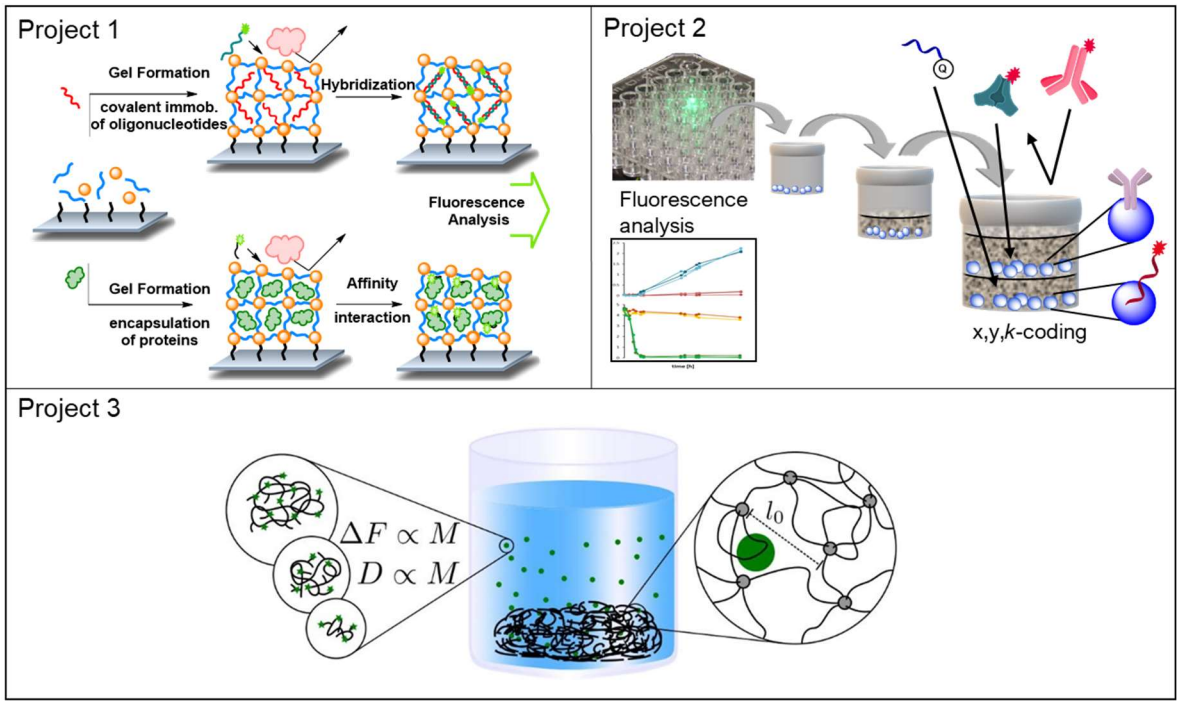

Figure 16 Overview of the projects covered in this thesis.

4 Publications and manuscript

In the following section the published articles and submitted manuscripts are listed, and the contributions of the authors are specified.

4.1 Bioorthogonal in Situ Hydrogels Based on Polyether Polyols for New Biosensor Materials with High Sensitivity

Anna Herrmann, Lena Kaufmann, Pradip Dey, Rainer Haag, and Uwe Schedler*

ACS Appl. Mater. Interfaces **2018**, *10,* 11382-11390.

https://doi.org/10.1021/acsami.8b01860

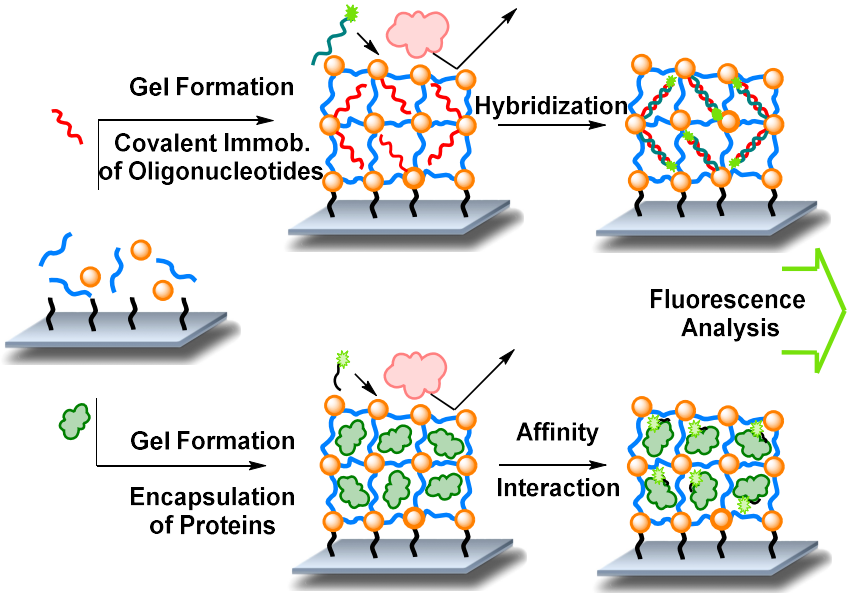

Figure 17 Graphical abstract. Reprinted with permission from ref. [156]. Copyright 2018 American Chemical Society

Author's contribution: In this publication, Anna Herrmann acquired the data and performed the synthesis for the covalent immobilization of biomolecules, investigated the accessibility of non-covalently entrapped streptavidin, wrote parts of the manuscript, and took care of all revision procedures. Lena Kaufmann performed the synthesis and experiments regarding the non-covalent entrapment, Pradip Dey helped with the hydrogel synthesis, Rainer Haag and Uwe Schedler supervised the project, provided scientific guidance, and proofread the manuscript.

4.2 Spatial Separation of Microbeads into Detection Levels by a Bioorthogonal Porous Hydrogel for Size-Selective Analysis and Increased Multiplexicity

Anna Herrmann, Stefan Rödiger, Carsten Schmidt, Peter Schierack, and Uwe Schedler*
Anal. Chem. **2019**, *91*, 8484-8491.
https://doi.org/10.1021/acs.analchem.9b01586

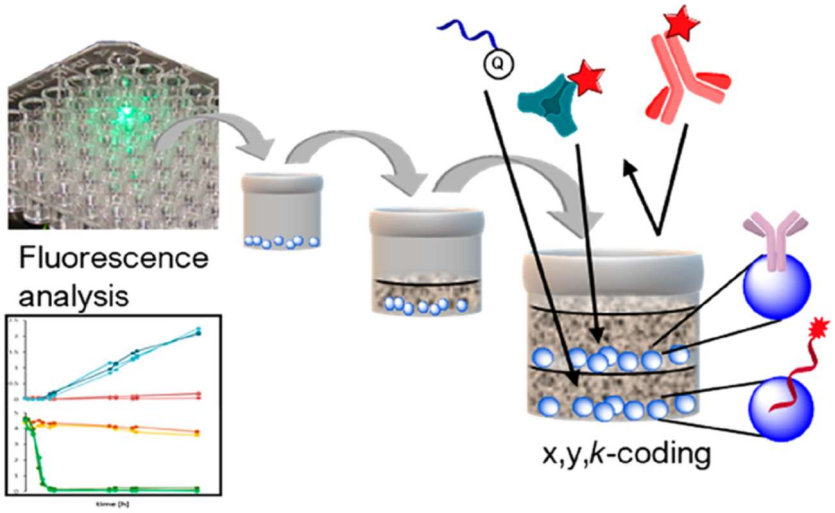

Figure 18 Graphical abstract. Reprinted with permission from ref.[157]. Copyright 2019 American Chemical Society

Author's contribution: In this publication, Anna Herrmann contributed to the design of the project, performed the syntheses and microbead functionalization, conducted all experiments, and wrote the paper. Stefan Rödiger contributed to the project idea and supervised the experiments, Carsten Schmidt introduced me into the microbead modification, Peter Schierack and Uwe Schedler supervised the project, provided scientific guidelines and suggestions, and corrected the manuscript.

4.3 Particle Diffusivity and Free-Energy Profiles in Inhomogeneous Hydrogel Systems from Time-Resolved Penetration Profiles

Amanuel Wolde-Kidan[#], Anna Herrmann[#], Albert Prause, Michael Gradzielski, Rainer Haag, Stephan Block, and Roland R. Netz

[#]These two authors contributed equally to this work

arXiv:2006.10676

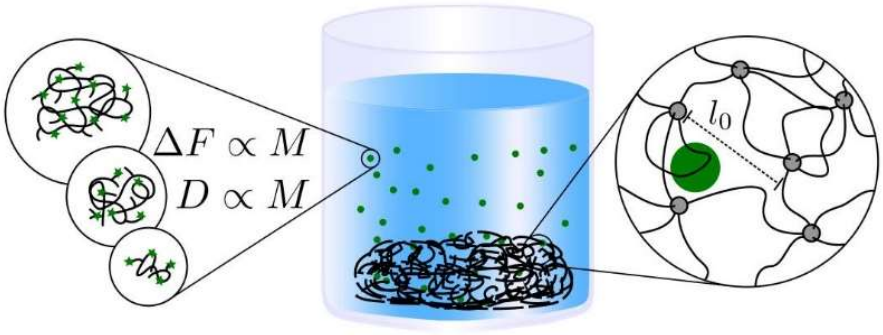

Figure 19 Graphical abstract.

Author's contribution: In this publication, Anna Herrmann performed all the experiments, including the development of the experimental setup, optimizations, and adapting them to the needs of the theoretical evaluation. Amanuel Wolde-Kidan evaluated the data and performed the theoretical evaluation. Albert Prause and Michael Gradzielski performed the FCS measurement and Rainer Haag provided scientific guidelines. Stephan Block gave the introduction to the Confocal microscope and supervised the experimental setup. Roland Netz supervised the project, provided scientific guidance, and wrote the manuscript.

Particle Diffusivity and Free-Energy Profiles in Inhomogeneous Hydrogel Systems from Time-Resolved Penetration Profiles

Amanuel Wolde-Kidan,[1,*] Anna Herrmann,[2,*] Albert Prause,[3] Michael Gradzielski,[3] Rainer Haag,[2] Stephan Block,[2] and Roland R. Netz[1,†]

[1] *Fachbereich Physik, Freie Universität Berlin, Arnimallee 14, 14195 Berlin, Germany*
[2] *Institut für Chemie und Biochemie, Freie Universität Berlin, Takustr. 3, 14195 Berlin, Germany*
[3] *Institut für Chemie, Straße des 17. Juni 124, Technische Universität Berlin, 10623 Berlin, Germany*

(Dated: June 19, 2020)

A combined experimental/theoretical method to simultaneously determine diffusivity and free-energy profiles of particles that penetrate into inhomogeneous hydrogel systems is presented. As the only input, arbitrarily normalized concentration profiles from fluorescence intensity data of labeled tracer particles for different penetration times are needed. The method is applied to dextran molecules of varying size that penetrate into hydrogels of polyethylene-glycol (PEG) chains with different lengths that are covalently cross-linked by hyperbranched polyglycerol (hPG) hubs. Extracted dextran bulk diffusivities agree well with fluorescence correlation spectroscopy data obtained separately. Scaling laws for dextran diffusivities and free energies inside the hydrogel are identified as a function of the dextran mass. An elastic free-volume model that includes dextran as well as PEG linker flexibility describes the repulsive dextran-hydrogel interaction free energy, which is of steric origin, quantitatively and furthermore suggests that the hydrogel mesh-size distribution is rather broad and particle penetration is dominated by large hydrogel pores. Particle penetration into hydrogels is for steric particle-hydrogel interactions thus governed by an elasticity-enhanced size-filtering mechanism that involves the tail of the hydrogel pore-size distribution.

INTRODUCTION

The penetration of particles into hydrogels is relevant for technological applications [1, 2], drug delivery [3] and in biological systems such as biofilms [4], the extracellular matrix [5] and mucus [6]. Mucus, which is the most common biological hydrogel, lines the epithelial tissues of different organs, such as the respiratory, gastrointestinal and urogenital tracts. Mucus is mainly composed of mucins, which are glycoproteins of varying length that absorb large amounts of water and thereby lend mucus its hydrogel nature, and additional components such as enzymes and ions [7]. Mucins are relevant in the cell signaling context and presumably also play a role in the development of cancer [8]. But primarily, mucus is a penetration barrier against pathogens, e.g. virions or bacteria, that enter the respiratory tract, while it allows the permeation of many non-pathogens, e.g. nutrients, that are absorbed through the mucosa of the small intestine [9]. Studies have suggested that, based on the type of mucus, different mechanisms give rise to the protective barrier function [10, 11], in addition to the advective transport of pathogens through mucus shedding or clearance [12, 13], which is not considered here. One typically distinguishes steric size-filtering mechanisms from interaction-filtering mechanisms [6, 14], the latter presumably play a major role in the defense of organisms against pathogens since they allow for precise regulation of the passage of wanted and unwanted particles and molecules [15, 16]. Recent studies demonstrated that attractive electrostatic interactions reduce particle diffusivity inside hydrogels substantially and much more than repulsive electrostatic interactions [17, 18] and that salt concentration and the distribution of charges and pore size are important parameters which influence the permeation properties of charged hydrogels [19, 20].

Particle penetration into mucus and biofilms has been studied by single-particle tracking techniques [21, 22] as well as by methods where a diffusor ensemble is observed [15, 16, 23, 24]. In the continuum description, which is valid on length scales larger than the hydrogel pore or mesh size, particle diffusion is completely described by the free-energy and diffusivity profiles across an inhomogeneous hydrogel system, on this level of description transient particle binding to the hydrogel [16] simply reduces the effective diffusivity. If the free-energy and diffusivity profiles are known, particle penetration can be quantitatively predicted, provided the particle concentration is low and the particles do not modify the hydrogel properties in an irreversible manner. In this context it should be noted that both profiles depend on the interactions between particle and hydrogel and therefore are different for each distinct hydrogel-particle pair. Due to method restrictions, experiments primarily focussed on determining either the particle diffusivity inside the hydrogel [6, 10, 21] or on the partitioning between hydrogel and the bulk solution [25], from which the free energy inside the hydrogel (relative to the bulk solution) can be determined. However, for prediction of the penetration or permeation speed of particles into the hydrogel, both the diffusivity and the free energy in the hydrogel are needed.

In this work, we study synthetic hydrogels that consist of polyethylene-glycol (PEG) linkers of different molec-

	n_{PEG} [μmol]	$V_{\mathrm{PEG}}^{\mathrm{sol}}$ [a] [μL]	n_{hPG} [μmol]	$V_{\mathrm{hPG}}^{\mathrm{sol}}$ [b] [μL]	$V_{\mathrm{H_2O}}$ [μL]	$V_{\mathrm{gel}}^{\mathrm{sol}}$ [μL]	V_{app} [μL]	m_{app} [μg]	$\mathrm{n_{app}}$ [nmol]
hPG-G6	0.14	10	0.05	2.80	13.00	25.80	1	38	7.30
hPG-G10	0.08	10	0.03	1.68	12.70	24.38	1	38	4.64

TABLE I. Composition of the hydrogels used in this study. Here, $V_{\mathrm{PEG}}^{\mathrm{sol}}$ and $V_{\mathrm{hPG}}^{\mathrm{sol}}$ denote the volumes of the stock solutions, $V_{\mathrm{H_2O}}$ is the volume of purified water added to the resulting gel solutions and n_{PEG} and n_{hPG} denote the amount of PEG-linkers and hPG-hubs in the gel solutions. From the total resulting volume of the gel solutions $V_{\mathrm{gel}}^{\mathrm{sol}}$ only $V_{\mathrm{app}} = 1$ μL was placed as a gel spot on the glass substrate, leading to the applied amount n_{app} and applied mass m_{app}. [a]Solution is of 8.5 wt% for 6 kDa PEG and 8.4 wt% for 10 kDa PEG. [b]hPG solution is of 5 wt%.

ular masses which are permanently cross-linked by hyperbranched polyglycerol (hPG) [2]. Such synthetic hydrogels can be regarded as simple models for mucus, since they display size-dependent particle permeabilities [14, 26], similar to mucus. As diffusing particles we employ fluorescently labelled dextran molecules of varying sizes. When using confocal laser-scanning fluorescence microscopy to investigate particle penetration into hydrogels, the sample can be oriented such that the hydrogel-bulk interface is either parallel [16] or perpendicular [27] to the optical axis, which makes no significant difference from a scanning perspective. However, for laterally extended samples like cell cultures that grow on a substrate, the parallel alignment causes the light path to span substantially larger distances, making this setup more prone to distortions in the imaging process. A perpendicular alignment, as employed in this work and sketched in Fig. 1, is therefore preferable for biological samples [27] and is also compatible with future extensions of such penetration assays to mucus-producing cell cultures.

We investigate the filtering function of the hydrogels by theoretical analysis of time-resolved concentration profiles of the labelled dextran molecules as they penetrate into the hydrogel. The employed numerical method allows for simultaneous extraction of free-energy and diffusivity profiles from relative concentration profiles at different times and is a significant extension of earlier methods [28–30] as it does not require absolute concentration profiles but works with relative, i.e. arbitrarily normalized, concentration profiles. This is a crucial advantage, as often fluorescence intensity profiles are subject to significant perturbation due to e.g. laser light intensity fluctuations or fluorescence dye bleaching over the course of the experiment, and makes the often difficult conversion of measured intensity data into absolute particle concentrations obsolete. Our method for the extraction of free-energy and diffusivity profiles from relative concentration profiles can be used for a wide range of different setups and systems. As a check on the robustness of the method, the extracted dextran bulk diffusivities are shown to agree well with fluorescence-correlation spectroscopy data that are obtained separately. The obtained particle free energies and diffusivities inside the hydrogel are shown to obey scaling laws as a function of the dextran mass. The dextran free energy inside the hydrogel is described by a free-volume model based on repulsive steric interactions between the dextran molecules and the hydrogel linkers, which includes dextran as well as hydrogel linker flexibility. This model constitutes a modified size-filtering mechanism for repulsive particle-hydrogel interactions, according to which particle penetration into hydrogel pores is assisted by the elastic widening of pores and the elastic shrinking of dextran molecules, and matches the extracted particle free energies in the hydrogel quantitatively. The model furthermore suggests that the hydrogel mesh size distribution is rather broad and that particle penetration is dominated by the fraction of large pores in the hydrogel.

METHODS

Hydrogel Preparation. The hydrogel is formed by cross-linking end-functionalized polyethylene glycol-bicyclo[6.1.0]non-4-yne (PEG-BCN) linkers with hyperbranched polyglycerol azide (hPG-N_3) hubs via strain-promoted azide-alkyne cycloaddition (SPAAC). The two macro-monomers PEG-BCN and hPG-N_3 are synthesized as previously described [2, 31]. The *click* reaction of binding the PEG-BCN linkers to the hPG-N_3 hubs works in water, at room temperature, without the addition of a catalyst or external activation like heat or UV radiation and without the formation of byproducts. Two different sizes of PEG-BCN linkers are employed, having a molecular weight of either $M_{\mathrm{PEG}} = 6$ or $M_{\mathrm{PEG}} = 10$ kDa (for details about the mass distributions see supplementary information), the hydrogels are denoted as *hPG-G6* and *hPG-G10*, respectively. The number ratio of the PEG-BCN linkers to the hPG-N_3 hubs ($\mathrm{M_{hPG}} = 3$ kDa, 20% azide) is kept constant at 3:1 for both *hPG-G6* and *hPG-G10*. This ratio can ideally lead to a cubic lattice structure if each hPG-hub exactly binds to six PEG-linkers. The chemical structure of the hPG-N_3 hubs, however, allows on average for eight binding sites, making the hydrogel presumably quite disordered.

The two components of the hydrogel are stored as aqueous stock solutions at concentrations of 8.5 wt% (6 kDa PEG-BCN), 8.4 wt% (10 kDa PEG-BCN) and 5 wt% (hPG-N_3). To initiate hydrogel formation, they are mixed according to Table I. The resulting gel solu-

tion is thoroughly vortexed before being placed as 1 μL drops on the glass substrate. Both hydrogel solutions are adjusted to have the same mass concentration. However, after drying and re-swelling on the glass substrate, volumes of the formed hydrogels are different and measured as $V_{\mathrm{tot}}^{\mathrm{hPG\text{-}G6}} = 0.42 \pm 0.03$ μL and $V_{\mathrm{tot}}^{\mathrm{hPG\text{-}G10}} = 0.31 \pm 0.04$ μL for *hPG-G6* and *hPG-G10*, respectively (for details see supplementary information). This results in a final hydrogel concentration of 9 wt% ($\approx$ 90 mg/mL) for *hPG-G6* and 12 wt% ($\approx$ 120 mg/mL) for *hPG-G10*.

Estimate of Mean Hydrogel Mesh Size. Assuming a cubic hydrogel network structure, the mean mesh size can be easily estimated. The length of a cubic unit cell l_0 follows from the total gel volume V_{tot} and the total number of hPG hubs $n_{\mathrm{hPG}}^{\mathrm{tot}}$ in mol as

$$l_0 = \sqrt[3]{\frac{V_{\mathrm{tot}}}{n_{\mathrm{hPG}}^{\mathrm{tot}} N_{\mathrm{A}}}} \tag{1}$$

where N_{A} is the Avogadro constant. The total volumes for the re-hydrated gels are $V_{\mathrm{tot}}^{\mathrm{hPG\text{-}G6}} = 0.42$ μL and $V_{\mathrm{tot}}^{\mathrm{hPG\text{-}G10}} = 0.31$ μL as mentioned above. The total number of hPG hubs is given as $n_{\mathrm{hPG}}^{\mathrm{tot}} = n_{\mathrm{hPG}} \cdot V_{\mathrm{app}} / V_{\mathrm{gel}}^{\mathrm{sol}}$, with the values from Table I for the respective gel and where we account for the fact that only $V_{\mathrm{app}} = 1$ μL of the total gel solution $V_{\mathrm{gel}}^{\mathrm{sol}}$ is applied onto the gel substrate. This results in estimates for the mesh size of $l_0^{\mathrm{hPG\text{-}G6}} = 7.1$ nm and $l_0^{\mathrm{hPG\text{-}G10}} = 7.5$ nm, which shows that even though PEG-linkers of significantly different masses were used, the mesh sizes of the two gels differ only slightly.

Dextran Preparation. Dextrans conjugated with the dye fluorescein isothiocyanate (FITC) are obtained from *Sigma-Aldrich* as d4-FITC, d10-FITC, d20-FITC, d40-FITC and d70-FITC, the number stating the molecular weight in kDa of the commercial product. To remove unbound FITC from the dextran solutions, all batches are subjected to a desalting PD-10 column, which eliminates low-molecular weight compounds such as free FITC dye. This step is done according to the manufacturers recommendations and the column is equilibrated using phosphate buffer saline (PBS). Afterwards, the molecular weight distribution of all dextrans is determined by gel permeation chromatography (GPC) (see supplementary information).

Penetration Assay of FITC-labeled Dextrans. After preparation of the hydrogel solutions and purification of the dextrans (see above), penetration assays are performed with five different dextran solutions and two different gels. For these assays, coverslips (Menzel #1; VWR, Darmstadt, Germany) with a diameter of 25 mm and a thickness of 0.13-0.16 mm are thoroughly washed with water and absolute ethanol and subsequently dried under a stream of nitrogen. For every experiment, 1 μL of the respective hydrogel solution is placed in the center of the coverslip. The substrates with the applied gel spots are kept in a humid environment overnight, allowing hydrogel formation to be completed before the hydrogel spots are left to dry for 30 min at ambient conditions. Permeation experiments are performed within one day after hydrogel formation. To start a permeation experiment, a home-made polydimethylsiloxane (PDMS) stamp (1 x 1 cm) prepared with a cylindrical cavity in the middle (5 mm diameter) is placed on the coverslip, so that the dried hydrogel is located in the middle of the stamp's cavity. The PDMS surrounding the dried hydrogel allows for the addition of solutions such as buffer or dextran. Prior to the measurement, 30 μL of PBS buffer are added to re-swell the hydrogel for 30 min, which typically creates hydrogel volumes of semi-spheroid shape with a base radius of 1050 μm and heights of about 150 μm for *hPG-G10* and about 210 μm for *hPG-G6* (see supplementary information). Afterwards, the coverslip is mounted on a Leica SP8 confocal laser scanning microscope (CLSM; Leica, Wetzlar, Germany) and imaged using a 20x objective (0.75 HC PL APO water immersion objective with correction ring). In a first step, the hydrogel is visually identified by imaging the sample with a 488 nm laser and collecting the transmitted light using the transmission photomultiplier tube (PMT) of the CLSM, allowing to place the optical axis of the CLSM in the centre of the hydrogel and to place the focal plane 30 μm below the glass-hydrogel interface. After aligning the sample like this, the PBS buffer is removed from the cavity and replaced by 35 μL of the FITC-dextran solution (0.07 mg/mL for all dextrans). This fixes the total length from the bottom of the glass dish at $z = z_{\mathrm{bot}}$ to the air-water interface at $z = -z_{\mathrm{top}}$, where $z = 0$ corresponds to the end of the measurement region (cf. Fig. 1A). The total length of the solution is thus $z_{\mathrm{tot}} = z_{\mathrm{top}} + z_{\mathrm{bot}} = 1780$ μm. The individual contributions to z_{tot} vary, due to different gel thicknesses, changing the extent of the measured region, ranging from $z = 0$ to $z = z_{\mathrm{bot}}$ (cf. Fig. 1A).

Immediately after the application of the dextran solution, the spatial distribution of the FITC-based fluorescence intensity is measured using a z-stack that starts 30 μm below and ends 410 μm above the glass-hydrogel interface (with 10 μm increments). The recorded intensities are afterwards truncated to probe the spatial FITC distribution within the hydrogel starting from the glass bottom (located at z_{bot}) and extending about 100 μm into the bulk solution, away from the gel-water interface located at $z = z_{\mathrm{int}}$ (cf. Fig. 1A). In these measurements, the sample is excited at $\lambda = 488$ nm and the emission is recorded between 500 nm and 550 nm using a PMT. For the $M_{\mathrm{dex}} = 4$ kDa to the $M_{\mathrm{dex}} = 40$ kDa dextrans, one z-

stack is recorded every $\Delta t = 10$ s, yielding time-resolved FITC distributions following the penetration of the dextran molecules into the hydrogel network over time. For the $M_{\mathrm{dex}} = 70$ kDa dextrans a period of $\Delta t = 30$ s is used instead, in order to account for the much smaller diffusion coefficient of the larger dextran molecules. For all dextran types, measurements are performed at least three times with total measurement times of about 30 minutes, with the exception of the $M_{\mathrm{dex}} = 70$ kDa dextrans. Here only one measurement is performed for each gel but with a longer recording time of about 1 hour.

Fluorescence Correlation Spectroscopy of FITC-labeled Dextrans. Reference diffusion coefficients for the FITC-labeled dextran molecules in the bulk solution are obtained using fluorescence correlation spectroscopy (FCS). The measurements are performed on a Leica TCS SP5 II CLSM with a FCS set-up from *PicoQuant*. The CLSM is equipped with an HCX PL APO 63x/1.20 W CORR CS water immersion objective. Samples are put on high precision cover glasses (18 x 18 mm, 170 ± 5 μm thick) and excited with the 488 nm Argon laser line. The fluorescent light is passed through a 50/50 beam splitter with a lower wavelength cut-off of $\lambda = 515$ nm. Both channels are detected separately with a single photon avalanche diode (SPAD). Afterwards a pseudo-cross correlation is performed between both channels to eliminate the influence of detector afterpulsing. Prior to a measurement, the optical setup is calibrated with the water soluble Alexa-Fluor 488 dye. The correlated signal is fitted with two components and accounting for triplet states. The first component is fixed to a freely diffusing FITC-dye molecule where only the fraction is a fit parameter. The second component is set to a log-normal distributed species. The component fractions and means of distribution are fitted and the width of distribution is taken from previously performed gel permeation chromatography (GPC) measurements (for details about the fitting procedure see supplementary information). The fitted diffusion times are used to calculate the diffusion coefficients and hydrodynamic radii using the Stokes-Einstein relation.

Numerical Model and Discretization. Extending a previously introduced method [28–30], spatially resolved diffusivity and free energy profiles are estimated from experimentally measured concentration profiles. Numerical profiles are computed by discretizing the entire experimental setup from the glass bottom of the substrate to the air-water interface (z_{bot} to $-z_{\mathrm{top}}$ in Fig. 1A). In the regime where concentration profiles are measured ($z = 0$ to $z = z_{\mathrm{bot}}$), the experimental resolution is used as the discretization width $\Delta z = 10$ μm. For the range without experimental data ($z = 0$ to $z = -z_{\mathrm{top}}$) in total six bins are employed. Two of those bins are spaced with $\Delta z = 10$ μm, for the other four bins, discretization spacings between $\Delta z = 300$ - 400 μm are used, depending on the z-length measured in the respective experiment z_{bot}. The z-dimension of the total system is the same for all experiments and given as $z_{\mathrm{tot}} = z_{\mathrm{top}} + z_{\mathrm{bot}} = 1780$ μm. The experimentally measured region always extends from the glass bottom through the gel and at least 100 μm into the bulk solution, away from the hydrogel-bulk interface, which leads to values of $z_{\mathrm{bot}} \approx 300$ μm, depending on the exact thickness of the hydrogel in the respective measurement.

The numerical optimization problem is given by the cost function, which is defined as

$$\sigma^2(D, F, \vec{f}) := \frac{1}{N \cdot M} \sum_{j=1}^{\mathrm{N}} \sum_{i=1}^{\mathrm{M}} \left[c_i^{\mathrm{num}}(t_j) - f_{\mathrm{j}} \cdot c_i^{\mathrm{exp}}(t_j)\right]^2 \tag{2}$$

with N the total number of experimental profiles, M the total number of experimental data points per concentration profile and $\sigma^2(D, F, \vec{f})$ being the mean squared deviation between the experimental and numerical profiles. The diffusivity profile $D = D(z)$, the free energy landscape $F = F(z)$ and the vector containing all scaling factors (see below for details) $\vec{f} = (f_1, ..., f_j, ..., f_N)$ are all optimized to find the minimal value of σ^2. This non-linear regression is performed using the trust region method implemented in python's *scipy* package [32].

The numerical profiles $\vec{c}_{\mathrm{num}}(t_{\mathrm{j}}) = (c_1^{\mathrm{num}}(t_{\mathrm{j}}), ..., c_i^{\mathrm{num}}(t_{\mathrm{j}}), ..., c_M^{\mathrm{num}}(t_{\mathrm{j}}))^T$ are computed from the diffusivity and free energy profiles as

$$\vec{c}_{\mathrm{num}}(t_{\mathrm{j}}) = e^{W t_{\mathrm{j}}} \cdot \vec{c}_{\mathrm{init}} \tag{3}$$

where the rate matrix $W(D, F)$ is defined as

$$W_{i,k} = \frac{D_i + D_k}{2\Delta z^2} e^{-\frac{F_i - F_k}{2 k_{\mathrm{B}} T}}, \quad \text{with} \quad k = i \pm 1 \tag{4}$$

according to ref [28]. Numerical profiles at time t_j depend on the initial profile $\vec{c}_{\mathrm{init}}$ at $t = 0$, which is determined as explained below.

The numerically computed profiles are fitted to the re-scaled experimental profiles $\vec{c}_{\mathrm{exp}}(t_{\mathrm{j}})$ at time $t_j > 0$. The scaling factors $\vec{f}$ are obtained simultaneously from the fitting procedure and correct drifts in the experimentally measured fluorescence intensity profiles (see supplementary information). As a check, the numerical model is compared to the analytical solution for a model with piece-wise constant values of the diffusivity and free energy in the respective regions. Results from the numerical model agree perfectly with those from the analytical solution (see supplementary information).

Construction of the Initial Concentration Profile. The initial profile $\vec{c}_{\mathrm{init}}$, used for the computation

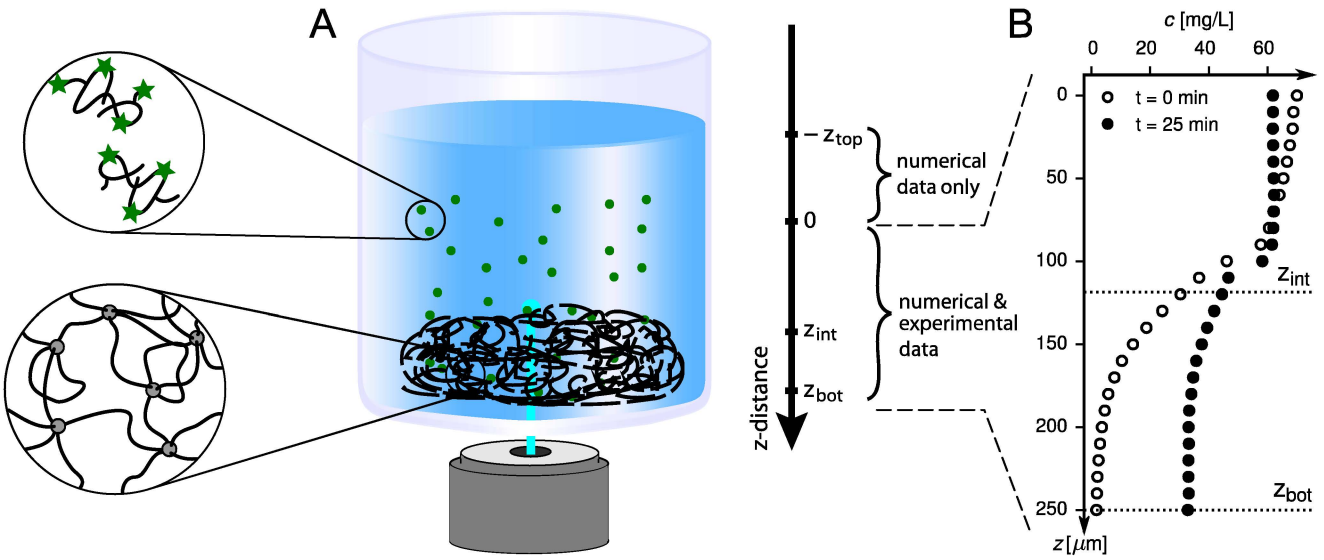

FIG. 1. A: Schematic drawing of the experimental setup. Concentration profiles of fluorescently labeled dextran molecules (green) are measured as they penetrate from the bulk solution (blue) into the hydrogel (black). The origin of the z-axis is positioned such that experimentally measured profiles range from $z = 0$ to $z = z_{\mathrm{bot}}$. The hydrogel-bulk solution interface is located at $z = z_{\mathrm{int}}$. In the range from $z = -z_{\mathrm{top}}$ to $z = 0$ only numerically determined concentration profiles are available. B: Exemplary experimental concentration profiles for two different penetration times for $M_{\mathrm{dex}} = 4$ kDa dextran diffusing into the *hPG-G10* hydrogel, positions of the hydrogel-bulk solution interface z_{int} and the hydrogel-glass bottom interface z_{bot} are indicated.

of all later profiles according to equation (3), needs to cover the entire computational domain and is generated by extending the first experimentally measured profile $\vec{c}_{\mathrm{exp}}(t = 0)$ into the bulk regime (from $z = 0$ to $z = -z_{\mathrm{top}}$, cf. Fig. 1A). We define $t = 0$ as the time of the first measurement, which is done approximately 10 seconds after application of the dextran solution onto the gel-loaded substrate. For the extension, a constant initial concentration is assumed in the bulk, the value of which is taken as the experimentally measured value furthest into the bulk $c_0 := c_1^{\mathrm{exp}}(t = 0)$ at $z = 0$. This leads to the following expression used for the initial profile

$$c_i^{\mathrm{init}} := \begin{cases} c_0, & \text{for } -z_{\mathrm{top}} \le z_i \le 0 \\ c_i^{\mathrm{exp}}(t = 0), & \text{for } 0 < z_i \le z_{\mathrm{bot}} \end{cases} \tag{5}$$

which by construction is continuous at $z = 0$. The initial profiles used for the fit procedure are shown in Fig. 2B and F as black lines. In order to obtain concentration profiles in physical units, we set the first measured value furthest into the bulk equal to the applied dextran concentration $c_0 = 0.07$ mg/mL.

Free Energy and Diffusivity Profiles. The diffusivity $D(z)$ and free energy $F(z)$ profiles are assumed to change in a sigmoidal shape from their values in the bulk solution to their values in the hydrogel. This sigmoidal shape is modeled using the following expressions

$$D(z) = \frac{D_{\mathrm{sol}} + D_{\mathrm{gel}}}{2} + \frac{D_{\mathrm{sol}} - D_{\mathrm{gel}}}{2} \operatorname{erf}\left(\frac{z - z_{\mathrm{int}}}{\sqrt{2} d_{\mathrm{int}}}\right) \tag{6a}$$

$$F(z) = \frac{F_{\mathrm{gel}}}{2} + \frac{F_{\mathrm{gel}}}{2} \operatorname{erf}\left(\frac{z - z_{\mathrm{int}}}{\sqrt{2} d_{\mathrm{int}}}\right) \tag{6b}$$

where $\operatorname{erf}(z) := 1/\sqrt{\pi} \int_{-z}^{z} e^{-z'^2}\, dz'$ is the error function. The fit parameters z_{int} and d_{int} determine the transition position and width, respectively, and are the same for the free energy and diffusivity profiles. Since only free energy differences carry physical meaning, the free energy in the bulk solution is set to zero, so that $F_{\mathrm{sol}} = 0$. The values of the diffusivity and free energy in the hydrogel and in the bulk solution are thus determined by fitting the five parameters of equations (6), namely D_{gel}, F_{gel}, D_{sol}, z_{int} and d_{int}, to the experimentally measured concentration profiles.

Confidence intervals for the obtained parameters of D_{sol}, D_{gel} and F_{gel} are estimated by determining the parameter values that change σ by not more than 50% (for details see supplementary information). The error bars shown in Figure 4 are then obtained by averaging the confidence intervals over all measurements.

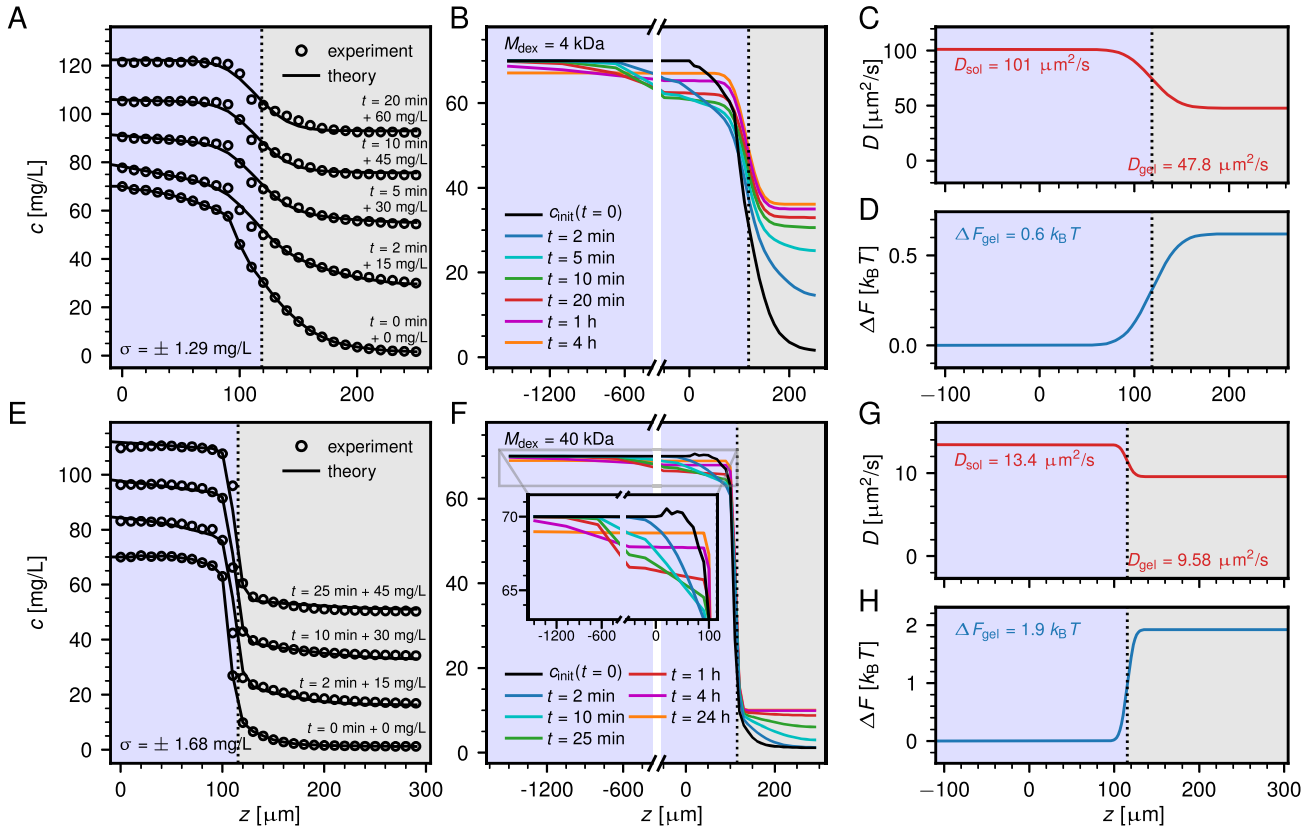

FIG. 2. Exemplary results for time-dependent dextran concentration profiles from experimental measurements (circles) and numerical modeling (solid lines) for the *hPG-G10* hydrogel. Results for the smallest dextran with $M_{\mathrm{dex}} = 4$ kDa in A-D are compared to results for $M_{\mathrm{dex}} = 40$ kDa in E-H. A&E: Experimental and modeled concentration profiles agree very accurately, note that concentration profiles are shifted vertically for better visibility. B&F: Modeled concentration profiles are presented for a wide range of penetration times. The initial profile $\vec{c}_{\mathrm{init}}$ (black line) is based on experimental data. C&G: Fitted diffusivity profiles, showing that the diffusivity in the hydrogel is slightly reduced compared to the bulk solution. D&H: Fitted free energy profiles. Significant exclusion of dextran from the hydrogel is observed, with a stronger effect for the larger dextran.

RESULTS AND DISCUSSION

Fluorescence intensity profiles of FITC-labeled dextran molecules penetrating into PEG-based hydrogels are analyzed using the procedure explained in the Methods section. The analysis is based on numerical solutions of the one-dimensional generalized diffusion equation [33]

$$\frac{\partial c(z,t)}{\partial t} = \frac{\partial}{\partial z}\left[D(z)e^{-\beta F(z)}\frac{\partial}{\partial z}\left(c(z,t)e^{\beta F(z)}\right)\right] \qquad (7)$$

where $c(z,t)$ is the concentration at time t and depth z (cf. also Fig. 1), $D(z)$ and $F(z)$ are the spatially resolved diffusivity and free energy profiles which the dextran molecules experience and $\beta = 1/k_{\mathrm{B}}T$ is the inverse thermal energy. While the diffusivity $D(z)$ describes the mobility of dextran molecules at position z, the free energy profile $F(z)$ uniquely determines the equilibrium partitioning of dextran molecules. The numerical solution of Eq. (7) provides a complete model of the penetration process into the hydrogel and at the same time allows for extraction of the diffusivity and free energy profiles by comparison with experimentally measured concentration profiles. A direct relation of measured fluorescence intensity to an absolute concentration is often difficult due to drifts of various kinds. The method developed here circumvents these problems and allows for in-depth analysis of arbitrarily normalized concentration profiles, as explained in the Methods section. Partition coefficients and diffusion constants both in the bulk and in the PEG hydrogel are obtained and the results for different hydrogels and dextran molecules of varying sizes are analyzed.

Comparison Between Experimental and Modeled Concentration Profiles. Figure 2A&E shows exemplary concentration profiles for dextran molecules with molecular masses of $M_{\mathrm{dex}} = 4$ kDa and $M_{\mathrm{dex}} = 40$ kDa penetrating into the *hPG-G10* hydrogel. Measurements are performed over a total time span of about 30 minutes

and concentration profiles are recorded every 10 seconds, leading to a total of about 180 concentration profiles as input for the fitting procedure. The first measured concentration profile at $t = 0$ min represents the start of the experiment, approximately 10 s after the dextran solution was applied onto the gel (see Methods section). The numerical model (lines) reproduces the experimentally measured concentration profiles (data points) very accurately, as seen in Fig. 2A&E. The deviation is estimated from the normalized sum of residuals, σ, according to eq. (2), which is below 2 mg/L for both measurements. A stationary concentration profile is obtained in the theoretical model only after 4 hours penetration for the smaller 4 kDa dextran, see Fig. 2B, for the larger dextran molecule the stationary profile is reached only after an entire day, see Fig. 2F. These times significantly exceed the duration of the experiments.

The diffusivity and free energy profiles in Fig. 2C, D, G, H, reveal the selective hydrogel permeability for dextran molecules of varying size. The free energy difference in the hydrogel is positive $\Delta F_{\rm gel} > 0$ for both dextran sizes, indicating that dextran is repelled from the hydrogel. The dextran partition coefficient K between the hydrogel and the bulk solution is related to the change in the free energy $\Delta F_{\rm gel}$ as

$$K_{\rm hydrogel/bulk} = e^{-\beta \Delta F_{\rm gel}} \qquad (8)$$

According to Eq. (8), the obtained free energy differences $\Delta F_{\rm gel} = 0.6\ k_{\rm B}T$ and $\Delta F_{\rm gel} = 1.9\ k_{\rm B}T$, correspond to partition coefficients of about $K_{\rm hydrogel/bulk} \approx 1/2$ and $K_{\rm hydrogel/bulk} \approx 1/7$ for the smaller and the larger dextran molecules, respectively, which illustrates a significant exclusion in particular for the larger dextran. Compared to the partition coefficients, the diffusion constants in the hydrogel decrease only slightly. This suggests that the dextran molecules are only modestly hindered in their motion, a conclusion that will be rationalized by our elastic free-volume model further below.

Figure 3 shows the temporal evolution of the average dextran concentration $\bar{c}$ in three different regions, namely inside the gel for $z_{\rm int} < z < z_{\rm bot}$, in the *near solution* for $0 < z < z_{\rm int}$, and in the *far solution* for $-z_{\rm top} < z < 0$ for the same data shown in Fig. 2. The lines show the model predictions, the circles the experimental data, which are not available in the *far solution* range. The average concentration in the gel (black) increases monotonically and saturates after about one hour for both dextran sizes. Note that the stationary final concentration in the hydrogel is considerably less for the larger dextran with $M_{\rm dex} = 40$ kDa. In contrast, the average concentration in the *far solution* saturates more slowly and shows a slight non-monotonicity for both dextran masses (blue). This non-monotonicity is more pronounced in the *near solution* (red) and is caused by the fact that dextran molecules diffuse

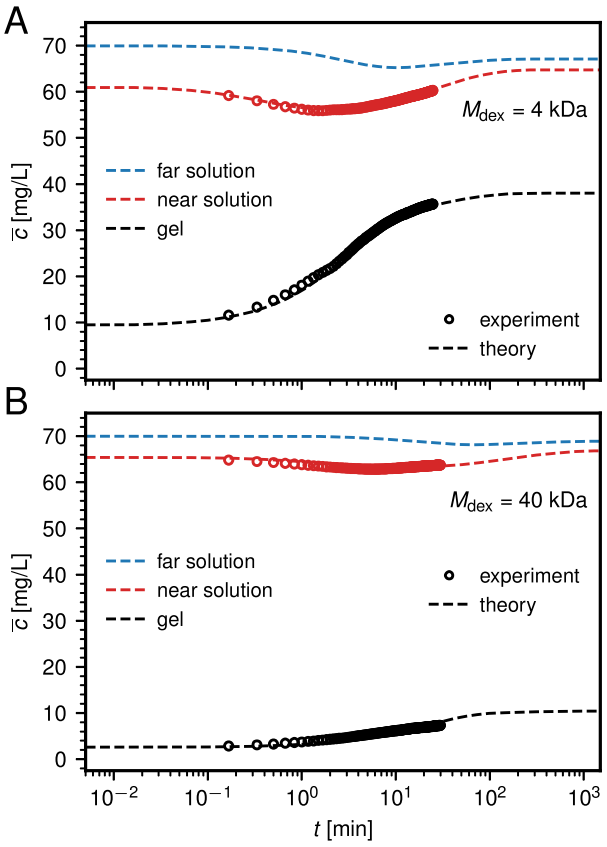

FIG. 3. Comparison of experimental results (circles) and modeling results (lines) for the mean dextran concentration $\bar{c}$ over time in three different regions, the *far solution* ($-z_{\rm top} < z < 0$), the *near solution* ($0 < z < z_{\rm int}$) and the gel ($z_{\rm int} < z < z_{\rm bot}$), see Fig. 1. The systems are the same as shown in Figure 2. A non-monotonic dextran concentration is measured over time in the near and far solution regions. The fact that $\bar{c}$ in the gel does not vanish for $t \to 0$ reflects that the first measurement is done approximately 10 s after the application of the dextran solution onto the gel.

quickly into the hydrogel from the *near solution* in the beginning of the experiment, while the replenishment from the bulk solution takes a certain time, as also seen in the concentration profiles in Fig. 2B&F. Very good agreement between experiments and modeling is observed.

Influence of Dextran Size on Hydrogel Penetration. The same analysis is performed for dextran molecules of molecular masses ranging from $M_{\rm dex} = 4$ kDa to $M_{\rm dex} = 70$ kDa that penetrate into PEG hydrogels with two different linker lengths, namely *hPG-G6* with a PEG-linker size of $M_{\rm PEG} = 6$ kDa and *hPG-G10* with $M_{\rm PEG} = 10$ kDa. Figure 4 shows the results obtained for the extracted diffusivities and free energies, which result from averages over at least three experi-

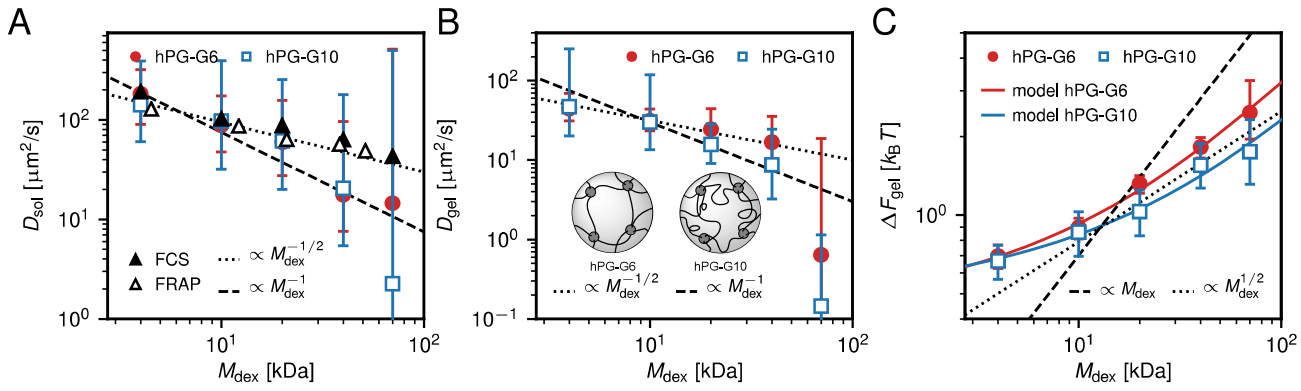

FIG. 4. Results for the diffusivity and free energy obtained from the experimental measurements as a function of dextran mass. A: Fitted diffusivities in the bulk solution (squares and circles) agree within the error with FCS data measured in the current work (solid black triangles) and with FRAP measurements from literature [34] (open black triangles). B: Fitted diffusivities in the hydrogel are reduced compared to the bulk values and are compared to different power laws. C: Dextran molecules are excluded from the hydrogel and $\Delta F_{gel} > 0$ for all dextran masses. For larger dextran molecules, ΔF_{gel} increases as a square root with the dextran mass. The results from the free-volume model of equation (13) (continuous lines) agree nicely with the measurements. Error bars have been estimated as explained in the supplementary information. The inset in B presents a schematic depiction of the two different gels. Even though the *hPG-G10* gel is composed of larger linkers, the mass density is larger than in the *hPG-G6* gel, which results in an effectively smaller pore size.

ments for each system, except for $M_{dex} = 70$ kDa dextran where only one experiment was performed.

Figure 4A shows the bulk diffusivities D_{sol} extracted from measured concentration profiles as colored symbols, in principle there should be no difference between results for *hPG-G6* and *hPG-G10*. A power law relation between the dextran mass and the diffusivity according to $D_{sol} \propto {M_{dex}}^{-\nu}$ is shown as straight lines for $\nu = 1$ (broken line) and for $\nu = 1/2$ (dotted line). The exponent $\nu = 1/2$ agrees nicely with our FCS data (solid black triangles) as well as with literature FRAP measurements [34] (open black triangles). An exponent of $\nu = 1/2$ follows from combining the Stokes-Einstein relation $D_{sol} = k_B T/6\pi\eta_w r_0$ with the scaling of the dextran hydrodynamic radius according to $r_0 \propto {M_{dex}}^{\nu}$ [35, 36] by assuming that the bulk solution is a theta solvent for dextran polymers [37, 38] (see supplementary information for details). The exponent $\nu = 1/2$ is only expected for linear polymers, while dextran rather is a branched polymer. The good agreement of FCS and FRAP data with the power law for $\nu = 1/2$ suggests that the degree of branching is low [39] or that it compensates self-avoidance effects. The hydrodynamic radii of the dextran molecules estimated from the FCS measurements compare well with the values reported by the supplier, see Table II. The data for D_{sol} obtained from the time-dependent dextran concentration profiles show rather large uncertainties, which is due to the fact that the concentration profiles are rather insensitive to the bulk diffusivities; they are within error bars consistent with our FCS results but do not allow extraction of the power-law scaling with any reasonable confidence.

M_{dex}	r_0	r_{FCS}
4 kDa	1.4 nm	1.45 nm
10 kDa	2.3 nm	2.7 nm
20 kDa	3.3 nm	3.15 nm
40 kDa	4.5 nm	4.3 nm
70 kDa	6.0 nm	6.4 nm

TABLE II. Dextran hydrodynamic radius r_0 as reported by the supplier, in comparison to estimated hydrodynamic radius r_{FCS} based on our FCS measurements using the Stokes-Einstein relation and the viscosity of water as $\eta_w = 0.8 \cdot 10^{-3}$ Pas.

Values for the diffusion constant in the hydrogel D_{gel} are compared to power laws with exponents $\nu = 1/2$ and $\nu = 1$ in Figure 4B. The difference of the diffusion constants between the two different hydrogels is within the error bars, in agreement with the fact that the estimated hydrogel mesh-sizes are $l_0^{\text{hPG-G6}} = 7.1$ nm and $l_0^{\text{hPG-G10}} = 7.5$ nm (see Methods section) and thus quite similar to each other. It is to be noted that for $M_{dex} \leq 20$ kDa, the mesh sizes are larger than twice the dextran hydrodynamic radii from Table II, which would not suggest any dramatic confinement effect on the diffusion constant. Interestingly, for the data where $M_{dex} \gtrsim 20$ kDa, the hydrogel with the larger linker length (*hPG-G10*), which has a slightly higher mesh size, is seen to reduce the diffusion constant slightly more, which at first sight is counterintuitive. This finding is rationalized by the fact that the *hPG-G10* gel has a higher mass density compared to the *hPG-G6* gel (see Methods sec-

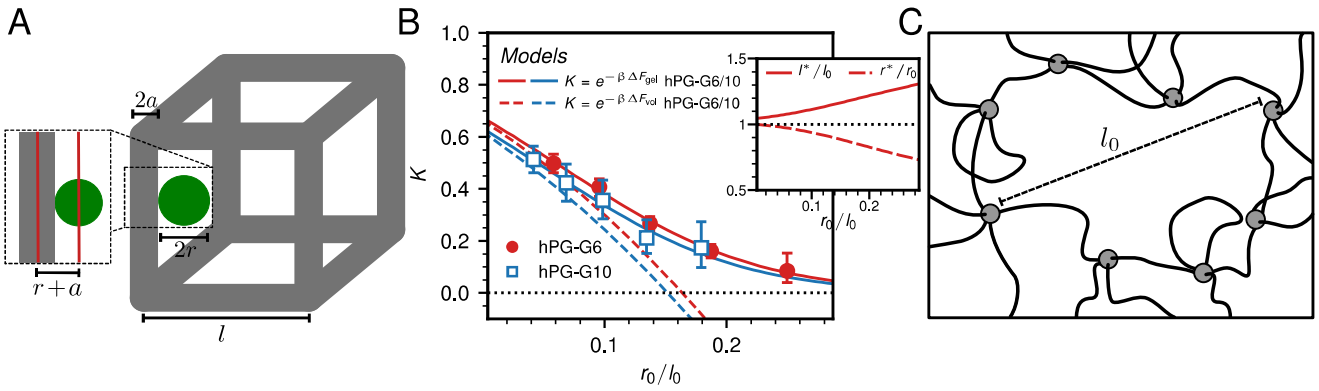

FIG. 5. Elastic free-volume model for the partitioning of a particle in a hydrogel. A: Cubic unit-cell model for the hydrogel, made up of connected linkers of length l and a finite radius of a. The diffusing particle is modeled as a sphere of radius r. Both the particle and the linkers are elastic and can stretch or contract. B: Partition coefficient K extracted from the experimentally measured dextran concentration profiles (symbols) in comparison to the elastic free-volume model predictions according to equation (13) (solid lines). The results of the non-elastic model according to equation (10) are shown as dashed lines. The inset shows the equilibrium values of l^* and r^* obtained for the *hPG-G6* gel. C: Illustration of a disordered pore in the hydrogel which has a mesh size l_0 and consists of more than four linkers.

tion), and thus the effective pore size is in fact substantially smaller. This is schematically illustrated in the inset in Figure 4B. A diffusivity scaling with an exponent $\nu > 1/2$, which describes the data for *hPG-G10* slightly better, could be rationalized by screened hydrodynamic interactions or by reptation-like diffusion [40]. In fact, a cross-over in the scaling as a function of the hydrogel density from $\nu = 1/2$ to $\nu = 1$ has been described before for dextran penetrating into hydroxypropylcellulose [36]. However, because of the large error bars, extraction of the diffusivity scaling with respect to dextran mass in the two gels is not uniquely possible. This is mostly due to the fact that the diffusivities change rather mildly with varying dextran mass.

Figure 4C shows the extracted values of ΔF_{gel} for the two hydrogels as a function of the dextran mass. For all measurements $\Delta F_{\mathrm{gel}} > 0$, which suggests exclusion of the dextran molecules from the hydrogel. Also the value of ΔF_{gel} increases with the dextran mass. Since dextran as well as the PEG-hPG based hydrogels are uncharged [41], this exclusion must be due to steric repulsion, possibly enhanced by hydration repulsion.

Elastic Free-Volume Model for Dextran Penetration in Hydrogels. For the larger dextran molecules, the hydrogel with the smaller PEG-linkers, *hPG-G6*, displays a slightly stronger exclusion. The power law relation between the hydrogel free energy and dextran mass according to $\Delta F_{\mathrm{gel}} \propto M_{\mathrm{dex}}^{\alpha}$ with an exponent of $\alpha = 1/2$ describes the data well for larger dextran masses $M_{\mathrm{dex}} \gtrsim 20$ kDa, as shown by the dotted black line in Figure 4C. This power law behavior is in fact compatible with an elastic free-volume model for the penetration of dextran molecules into hydrogels, which yields the solid lines and will be derived in the following.

The model geometry is sketched in Figure 5A and consists of a single dextran molecule of radius r (green sphere) inside a cubic unit cell of the PEG based hydrogel (grey cylinders). The dextran experiences a reduction of its free volume compared to the bulk solution, due to steric interactions with the PEG-linkers. In the simple model geometry, the PEG-linkers are located at the edges of the unit cell and are impenetrable cylinders of radius a and length l. The inaccessible volume for dextran in the cubic unit cell consists of a quarter of each of the twelve cylinders at the edges. The accessible or free volume in the hydrogel V_{free} depends on the sum of sphere radius r and cylinder radius a and is given by

$$\begin{aligned} V_{\mathrm{free}} &= V_{\mathrm{unit}} - V_{\mathrm{ex}} \\ &= l^3 - \frac{12}{4}\pi(r+a)^2\left(l - \frac{4}{3}(a+r)\right) \end{aligned} \tag{9}$$

where $V_{\mathrm{unit}} = l^3$ is the volume of the unit cell and subtraction of $4(a+r)/3$ from l avoids over counting of the corners. The entropic contribution to the total free energy is given by

$$\begin{aligned} \Delta F_{\mathrm{vol}} &= -k_{\mathrm{B}}T \ln\left(\frac{V_{\mathrm{free}}}{V_{\mathrm{unit}}}\right) \\ &= -k_{\mathrm{B}}T \ln\left(1 - 3\pi\left[\frac{r+a}{l}\right]^2\left[1 - \frac{4(a+r)}{3l}\right]\right) \end{aligned} \tag{10}$$

Since dextran and the PEG linkers are elastic polymers,

they are both flexible and can deform. For small deformations, the polymers behave like Gaussian chains [37, 38]. The elastic deformation free energy for a cubic unit cell consisting of 12 equally deformed PEG-linkers can be written as (for a detailed derivation see supplementary information)

$$\Delta F_{\mathrm{PEG}} = \frac{12}{2} k_{\mathrm{B}} T \left(\left[\frac{l}{l_0} \right]^2 + \frac{1 - 4 \left[\frac{l}{l_0} \right]^2}{2 + \left[\frac{l}{l_0} \right]^2} \right) \qquad (11)$$

Here l/l_0 is the relative stretching of the PEG-linkers, where l_0 denotes the edge length of the unit cell in the absence of dextran molecules. The elastic deformation energy of dextran is obtained in the same fashion and reads

$$\Delta F_{\mathrm{dex}} = \frac{3}{2} k_{\mathrm{B}} T \left(\left[\frac{r}{r_0} \right]^2 + \left[\frac{r_0}{r} \right]^2 - 2 \right) \qquad (12)$$

where r denotes the deformed dextran radius and the equilibrium dextran radius is denoted by r_0 and is taken from Table II. The complete free energy follows as

$$\Delta F_{\mathrm{gel}}(r, l) = \Delta F_{\mathrm{vol}}(r, l) + \Delta F_{\mathrm{PEG}}(l) + \Delta F_{\mathrm{dex}}(r) \quad (13)$$

The equilibrium free energy is given by its minimal value, obtained for the optimal stretched unit cell length l^* and the optimal dextran radius r^*, which are determined numerically. The values of the unit cell length l_0 and the PEG linker thickness a are adjusted by fits. The model results are shown in Figure 5B in terms of the partition coefficient as solid lines and compared to the experiments (circles and squares) as a function of the length ratio r_0/l_0. The inset shows the obtained equilibrium values for l^* and r^* for the *hPG-G6* gel. A considerable stretching of PEG-linkers and compression of dextran is observed, which shows that elasticity effects of both PEG linkers and dextran molecules are important.

The fit to the experimental data yields $l_0^{\text{hPG-G6}} = 24.0$ nm, $l_0^{\text{hPG-G10}} = 33.5$ nm, $a_{\text{hPG-G6}} = 5.4$ nm and $a_{\text{hPG-G10}} = 8.2$ nm. The values of a certainly represent an effective PEG linker radius, including the effects of polymer crumpling and a layer of tightly bound hydration water. In fact, the free-volume model yields estimates of the number of hydration waters per PEG monomer in the range from 6 to 12, depending on dextran mass and PEG length, in rough agreement with literature data (for details see supplementary information). The fit values for the unit cell length l_0 are several times larger than the mean mesh size estimated based on equation (1) but still shorter than the PEG contour length $L = b_0 N$, which is L =48.5 nm for the *hPG-G6* gel and L =80.9 nm for the *hPG-G10* gel, where $b_0 = 0.356$ nm is the PEG monomer length [42]. Since there is no reason why the linkers should be stretched to almost their contour length, we rationalize this surprising result in terms of a broad distribution of pore sizes that exhibit different topologies. To illustrate this, a random pore is schematically shown in Figure 5C. Based on the 3:1 ratio of linkers and cross linkers in the hydrogel formulation, a perfectly cubic lattice could form where each hub is connected to 6 different linkers. Such an ideal cubic connectivity is of course entropically highly unfavorable and the connectivity distribution of hubs, i.e. the distribution of the number of linkers that connect to one hub, will be rather broad and the network topology will be disordered. While in a cubic lattice each cubic facet consists of four hubs and four linkers, the pores present in the actual hydrogel will show a broad distribution of the number of participating linkers. For illustration, the pore shown in Figure 5C consists of eight linkers. Clearly, dextran molecules will tend to be located in large pores in order to maximize their free volume, and therefore the fit parameters of our model tend to be dominated by the tail of the pore size distribution, which explains the large fit values for l_0. This finding also explains why the dextran diffusivities in the hydrogel differ only mildly from the bulk diffusivities, since large pores restrict the diffusion of particles only slightly. Clearly, the precise topology and compositional distribution of pores cannot be predicted by our analysis, our results should thus be merely interpreted as an indication of the presence of large pores and a disordered network topology.

An approximate non-elastic version of the free-volume model is obtained by neglecting the polymer deformation term and just keeping the excluded volume term, equation (10), which becomes accurate in the limit of $l_0 \gg r_0$, where $r \approx r_0$ and $l \approx l_0$. These approximate results are shown as broken lines in Figure 5B and describe the experimental data only for small values of r_0/l_0. When additionally approximating the logarithm, the obtained expression for the free energy is similar to results derived for a random-fiber network [43].

Derivation of Particle Permeability through Hydrogels. Permeation through biological barriers is quantified by the permeability coefficient P, which is defined as [44]

$$P(z_1, z_2) = \frac{J}{c(z_1) - c(z_2)} \qquad (14)$$

where $c(z_1)$ and $c(z_2)$ are the particle concentrations at the two sides z_1 and z_1 of the barrier, and J denotes the particle flux through the barrier. Based on the diffusion equation (7), the permeability can be written as (for a detailed derivation see supplementary information)

$$\frac{1}{P(z_1, z_2)} = \int_{z_1}^{z_2} \frac{e^{\beta F(z)}}{D(z)} \, dz \qquad (15)$$

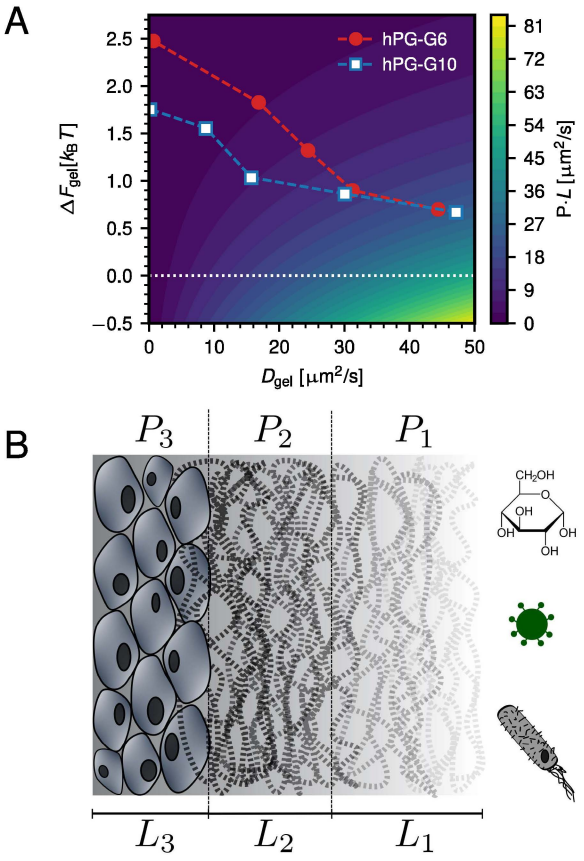

FIG. 6. A: Normalized permeability coefficient PL through a hydrogel barrier of width L as a function of the hydrogel free energy $\Delta F_{\rm gel}$ and the hydrogel diffusivity $D_{\rm gel}$ from equation (16). High permeability is observed for low energy barriers and high mobility in the hydrogel. The symbols denote the experimental data from Fig. 4. Due to opposing trends in the energy barrier and the diffusivity, both hydrogels display comparable permeability coefficients. B: Schematic layered structure of a mucous membrane, as found in the stomach. Examples for different diffusors are shown, including nutrients such as glucose and pathogens such as virions or bacteria. The diffusors have to penetrate different layers of varying permeabilities to enter the tissue below the mucous membranes, the total permeability of a layered structure follows from Eq. (17).

For a step-like barrier one obtains

$$\frac{1}{P} = \frac{e^{\beta\Delta F_{\rm gel}}}{D_{\rm gel}} L \tag{16}$$

Here $\Delta F_{\rm gel}$ and $D_{\rm gel}$ are the particle free energy relative to the solution and the diffusivity inside the hydrogel and L denotes the width of the hydrogel barrier.

Figure 6A shows normalized permeability coefficients PL, which are independent of the thickness of the barrier L, as a function of the free energy and the diffusivity. The values obtained from the experimental data for different dextran molecules in the two gels from Fig. 4 are indicated by data points. Obviously, the highest permeability is observed for a low energy barrier and a high diffusor mobility, as is the case for the smallest dextran molecules (lower right corner in Figure 6A). On the other hand, permeation is hindered by either a high energy barrier or a low mobility in the hydrogel, both of which are observed for dextran molecules with larger molecular weights. Due to counterbalancing effects of stronger exclusion in the *hPG-G6* gel and increased immobilization in the case of *hPG-G10*, both hydrogels display comparable permeability coefficients for the chosen dextran molecular masses.

CONCLUSION

The method introduced in this paper allows for the simultaneous extraction of diffusivity and free-energy profiles of particles that permeate into spatially inhomogeneous hydrogel systems. The advantage over alternative methods is that both quantities are obtained from a single experimental setup. This is important, as only the combination of diffusivity and free-energy profiles completely determines the diffusion of particles.

From measurements of fluorescently labeled dextran molecules permeating into PEG-hPG-based hydrogels, diffusivities and free energies in the hydrogel are obtained and analyzed in terms of scaling laws as a function of dextran mass. Dextran and PEG linkers repel each other via steric interactions. A modified free volume model that includes the elasticity of PEG linkers and of the diffusing dextran molecules quantitatively accounts for the extracted free energy values and shows that the effective hydrogel mesh size is substantially larger than the mean mesh size. This means that the dextran molecules preferentially move into larger hydrogel pores that are locally even more enlarged due to the osmotic pressure exerted by the dextran molecule on the local hydrogel network.

Diffusional barriers in biological systems often show a layered structure, as previously demonstrated for skin [28–30] and is also the case for mucous membranes, as found for instance in the gastrointestinal tract, schematically indicated in Fig. 6B. For a layered system, equation (15) shows that the individual piecewise constant permeability coefficients P_i add up inversely as

$$\frac{1}{P_{\rm tot}} = \sum_i \frac{1}{P_i} = \sum_i \frac{e^{\beta\Delta F_i}}{D_i} L_i = \sum_i \frac{L_i}{D_i K_i} \tag{17}$$

where the sum goes over all layers, represented by their respective diffusion constants D_i, free energy values ΔF_i or partition coefficients K_i and thicknesses L_i. Here, $P_{\rm tot}$ denotes the total permeability, which is dominated by the smallest permeability in the inverse sum.

Figure 6B illustrates permeation through a layered system which represents the mammalian stomach [45]. The

outermost layer of mucus is only loosely bound and characterized by the permeability P_1, it is followed by a layer of more tightly bound mucus, characterized by P_2, and adheres onto the first layer of epithelial cells, characterized by P_3. The total thickness of this diffusional barrier is about a millimetre, with the two mucus layers spanning a few hundred micrometers only [46]. Measurements in rat gastrointestinal mucosa give values of $L_1 = 109$ μm, $L_2 = 80$ μm and $L_3 \approx L_2$ [47], which are close to the range of gel thicknesses studied in this work.

The total permeability is determined by the free energies and the mobilities inside all layers. Nutrients for instance can easily penetrate through the epithelia of the gastrointestinal tract, displaying large permeabilities in the different layers. Pathogens on the other hand are in healthy environments kept from reaching the epithelium, due to low permeability in the tightly bound mucus layer ($P_2 \ll P_1$) [45]. From equation (17), it is apparent that the lowest permeability in such a layered system dominates the total permeability, leading to an effective barrier function.

The method introduced in this work can be used to determine free-energy and diffusivity profiles of different kinds of fluorescently labeled molecules, particles or even organisms that penetrate into various layered systems, including systems that contain hydrogels and mucus. This will help to shed light on the underlying mechanisms of the function of biological barrier including mucous membranes.

* These two authors contributed equally to this work.
† rnetz@physik.fu-berlin.de

[1] D. Wirthl, R. Pichler, M. Drack, G. Kettlguber, R. Moser, R. Gerstmayr, F. Hartmann, E. Bradt, R. Kaltseis, C. M. Siket, S. E. Schausberger, S. Hild, S. Bauer, and M. Kaltenbrunner, Science Advances **3**, e1700053 (2017).
[2] A. Herrmann, L. Kaufmann, P. Dey, R. Haag, and U. Schedler, ACS Applied Materials & Interfaces **10**, 11382 (2018).
[3] J. Li and D. J. Mooney, Nature Reviews Materials **1**, 16071 (2016).
[4] N. Billings, A. Birjiniuk, T. S. Samad, P. S. Doyle, and K. Ribbeck, Reports on Progress in Physics **78**, 036601 (2015).
[5] A. M. Rosales and K. S. Anseth, Nature Reviews Materials **1**, 15012 (2016).
[6] O. Lieleg, I. Vladescu, and K. Ribbeck, Biophysical Journal **98**, 1782 (2010).
[7] C. Wagner, K. Wheeler, and K. Ribbeck, Annual Review of Cell and Developmental Biology **34**, 189 (2018).
[8] M. A. Hollingsworth and B. J. Swanson, Nature Reviews Cancer **4**, 45 (2004).
[9] M. A. McGuckin, S. K. Lindén, P. Sutton, and T. H. Florin, Nature Reviews Microbiology **9**, 265 (2011).
[10] M. Dawson, D. Wirtz, and J. Hanes, Journal of Biological Chemistry **278**, 50393 (2003).
[11] S. K. Lai, D. E. O'Hanlon, S. Harrold, S. T. Man, Y.-Y. Wang, R. Cone, and J. Hanes, Proceedings of the National Academy of Sciences **104**, 1482 (2007).
[12] M. E. V. Johansson, PLoS ONE **7**, e41009 (2012).
[13] B. Button, L.-H. Cai, C. Ehre, M. Kesimer, D. B. Hill, J. K. Sheehan, R. C. Boucher, and M. Rubinstein, Science **337**, 937 (2012).
[14] J. Witten and K. Ribbeck, Nanoscale **9**, 8080 (2017).
[15] L. D. Li, T. Crouzier, A. Sarkar, L. Dunphy, J. Han, and K. Ribbeck, Biophysical Journal **105**, 1357 (2013).
[16] M. Marczynski, B. T. Käsdorf, B. Altaner, A. Wenzler, U. Gerland, and O. Lieleg, Biomaterials Science **6**, 3373 (2018).
[17] X. Zhang, J. Hansing, R. R. Netz, and J. E. DeRouchey, Biophysical Journal **108**, 530 (2015).
[18] J. Hansing, C. Ciemer, W. K. Kim, X. Zhang, J. E. DeRouchey, and R. R. Netz, The European Physical Journal E **39**, 53 (2016).
[19] J. Hansing and R. R. Netz, Biophysical Journal **114**, 2653 (2018).
[20] J. Hansing, J. R. Duke, E. B. Fryman, J. E. DeRouchey, and R. R. Netz, Nano Letters **18**, 5248 (2018).
[21] M. Dawson, E. Krauland, D. Wirtz, and J. Hanes, Biotechnology Progress **20**, 851 (2004).
[22] C. E. Wagner, B. S. Turner, M. Rubinstein, G. H. McKinley, and K. Ribbeck, Biomacromolecules **18**, 3654 (2017).
[23] J. N. Wilking, V. Zaburdaev, M. De Volder, R. Losick, M. P. Brenner, and D. A. Weitz, Proceedings of the National Academy of Sciences **110**, 848 (2013).
[24] J. R. Lawrence, G. M. Wolfaardt, and D. R. Korber, Applied and Environmental Microbiology **60**, 1166 (1994).
[25] A. P. Sassi, A. J. Shaw, Sang Min Han, H. W. Blanch, and J. M. Prausnitz, Polymer **37**, 2151 (1996).
[26] A. Herrmann, S. Rödiger, C. Schmidt, P. Schierack, and U. Schedler, Analytical Chemistry **91**, 8484 (2019).
[27] M. Furter, M. E. Sellin, G. C. Hansson, and W.-D. Hardt, Cell Reports **27**, 2665 (2019).
[28] R. Schulz, K. Yamamoto, A. Klossek, R. Flesch, S. Hönzke, F. Rancan, A. Vogt, U. Blume-Peytavi, S. Hedtrich, M. Schäfer-Korting, E. Rühl, and R. R. Netz, Proceedings of the National Academy of Sciences **114**, 3631 (2017).
[29] R. Schulz, K. Yamamoto, A. Klossek, F. Rancan, A. Vogt, C. Schütte, E. Rühl, and R. R. Netz, Biophysical Journal **117**, 998 (2019).
[30] S. B. Lohan, S. Saeidpour, M. Colombo, S. Staufenbiel, M. Unbehauen, A. Wolde-Kidan, R. R. Netz, R. Bodmeier, R. Haag, C. Teutloff, R. Bittl, and M. C. Meinke, Pharmaceutics **12**, 400 (2020).
[31] P. Dey, T. Schneider, L. Chiappisi, M. Gradzielski, G. Schulze-Tanzil, and R. Haag, Macromolecular Bioscience **16**, 580 (2016).
[32] M. A. Branch, T. F. Coleman, and Y. Li, SIAM Journal on Scientific Computing **21**, 1 (1999).
[33] H. Risken and T. Frank, *The Fokker-Planck Equation: Methods of Solution and Applications*, Springer Series in Synergetics (Springer Berlin Heidelberg, 2012).
[34] P. Gribbon and T. E. Hardingham, Biophysical Journal **75**, 1032 (1998).
[35] Y. Cheng, R. K. Prud'homme, and J. L. Thomas, Macromolecules **35**, 8111 (2002).
[36] Z. Bu and P. S. Russo, Macromolecules **27**, 1187 (1994).
[37] M. Rubinstein and R. H. Colby, *Polymer Physics* (OUP

Oxford, 2003).
[38] R. R. Netz and D. Andelman, Physics Reports **380**, 1 (2003), 0203364.
[39] K. A. Granath, Journal of Colloid Science **13**, 308 (1958).
[40] P. G. de Gennes, The Journal of Chemical Physics **55**, 572 (1971).
[41] Y.-Y. Wang, S. K. Lai, J. S. Suk, A. Pace, R. Cone, and J. Hanes, Angewandte Chemie International Edition **47**, 9726 (2008).
[42] S. Liese, M. Gensler, S. Krysiak, R. Schwarzl, A. Achazi, B. Paulus, T. Hugel, J. P. Rabe, and R. R. Netz, ACS Nano **11**, 702 (2017).
[43] J. C. Giddings, E. Kucera, C. P. Russell, and M. N. Myers, The Journal of Physical Chemistry **72**, 4397 (1968).
[44] J. M. Diamond and Y. Katz, The Journal of Membrane Biology **17**, 121 (1974).
[45] M. E. V. Johansson, H. Sjövall, and G. C. Hansson, Nature Reviews Gastroenterology & Hepatology **10**, 352 (2013).
[46] N. Jordan, J. Newton, J. Pearson, and A. Allen, Clinical Science **95**, 97 (1998).
[47] C. Atuma, V. Strugala, A. Allen, and L. Holm, American Journal of Physiology-Gastrointestinal and Liver Physiology **280**, G922 (2001).

Supplementary Information: Particle Diffusivity and Free-Energy Profiles in Inhomogeneous Hydrogel Systems from Time-Resolved Penetration Profiles

Amanuel Wolde-Kidan,[1,*] Anna Herrmann,[2,*] Albert Prause,[3] Michael Gradzielski,[3] Rainer Haag,[2] Stephan Block,[2] and Roland R. Netz[1,†]

[1] *Fachbereich Physik, Freie Universität Berlin, Arnimallee 14, 14195 Berlin, Germany*
[2] *Institut für Chemie und Biochemie, Freie Universität Berlin, Takustr. 3, 14195 Berlin, Germany*
[3] *Institut für Chemie, Straße des 17. Juni 124, Technische Universität Berlin, 10623 Berlin, Germany*

(Dated: June 19, 2020)

Molecular Mass Distributions of PEG-Linkers and Dextran Molecules.

The dextran molecular mass distribution is characterized using gel permeation chromatography (GPC), the results of which are presented in Table I. GPC measurements were performed on an *Agilent* device (1100er series) with a PSS Suprema column (pre-column, 1x with poresize of 30 Å, 2x with poresize of 1000 Å, all of them with a particle size of 10 μm), with pullulan as calibration standard, and ethylene glycol as internal standard. As solvent, H_2O with 0.1 M $NaNO_3$ was used.

For the characterization of the PEG-linker mass distribution matrix assisted laser desorption ionization (MALDI) on a *Bruker Ultraflex* II is performed. The obtained values are shown in Table II.

From the number average molecular mass M_n and the weight average molecular mass M_w the polydispersity index PDI is determined as

$$PDI = \frac{M_\mathrm{w}}{M_\mathrm{n}}. \tag{S1}$$

The dextran molecules show a considerable dispersion regarding the molecular mass, while the PEG-linker mass distribution is rather uniform.

M_dex [kDa]	M_w [kDa]	M_n [kDa]	PDI
4	3.55	2.32	1.53
10	9.55	5.55	1.72
20	16.5	9.42	1.75
40	35.7	19.5	1.84
70	61.9	50.1	1.24

TABLE I. Results obtained from GPC measurements of the different dextran molecules.

M_PEG [kDa]	M_w [kDa]	M_n [kDa]	PDI
6	6.29	5.90	1.07
10	11.3	11.3	1.00

TABLE II. Molecular weights and polydispersity of the PEG-linkers as measured in MALDI experiments.

Hydrogel Volume Reconstruction.

The hydrogel volume is determined using confocal laser scanning microscopy as follows. The hydrogels are first equilibrated using PBS buffer, followed by injection of the $M_{\mathrm{dex}} = 70$ kDa FITC-labeled dextran and recording of 3D dextran concentration profiles using confocal microscopy (covering an imaged volume of 2,304 x 2,304 x 0.5 mm^3). The permeation measurements (shown in the main text) reveal that this dextran is too large to penetrate the hydrogel, so that the hydrogel can be identified in these 3D concentration profiles based on an exclusion of FITC-labeled dextran (i.e., absence of FITC fluorescence; see Fig. S1). In order to quantify the hydrogel volume, the (2D) hyperplane at which the FITC intensity has dropped to 50% of its bulk value is determined using home-written scripts in *Matlab* (*MathWorks*, Natick, MA). This hyperplane indicates the positions, at which the point spread function of the confocal microscope is equally filled by the FITC-dextran bulk solution and either the hydrogel or the supporting substrate, and therefore allows for extraction of the exact locations of the substrate and hydrogel interface within the sample. Furthermore, as the substrate is a flat glass slide, the hydrogel-substrate interface is extracted from this data by first fitting a plane to the regions corresponding to the substrate-bulk interface (i.e., in regions far away from the hydrogel spot) and by interpolating the position of this plane underneath the hydrogel. This procedure allows for extraction of the entire hydrogel boundary, allowing determination of the hydrogel volume by numerical integration. This yields volumes of $V_{\mathrm{tot}}^{\mathrm{hPG\text{-}G6}} = 0.42 \pm 0.03$ μL and $V_{\mathrm{tot}}^{\mathrm{hPG\text{-}G10}} = 0.31 \pm 0.04$ μL for the two hydrogels.

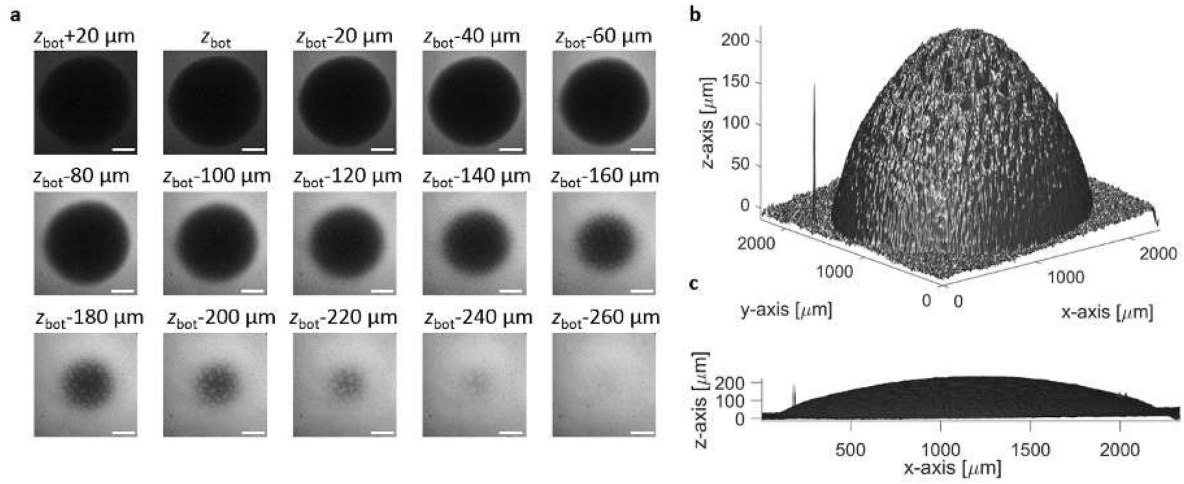

Supplementary Figure S1. In these experiments, the hydrogels have been equilibrated using PBS buffer (as described in the Methods section in the main text) followed by application of a $M_{\mathrm{dex}} = 70$ kDa dextran solution. The dextran is too large to penetrate into the hydrogel as evidenced by using confocal fluorescence microscopy to record multiple sample sections (at different z-heights as indicated in (a)). In these images, the hydrogel appears as a black circle, the radius of which decreases with increasing distance to the glass interface (located at the z-height z_{bot}). The bright areas correspond to FITC-dextran solution in the bulk. These images can be used to extract the position of the glass interface and hydrogel in space. A 3D representation and a side view of this hyperplane are given in (b) and (c), respectively, showing that the hydrogels possess a semi-elliptical shape with radii being on the order of 1050 μm (major axis) and 150 – 210 μm (minor axis). This figure shows a representative measurement for the *hPG-G6* gel. The scale bars in (a) correspond to 500 μm.

Fitting Procedure for FCS Measurements.

An accurate description of the dextran autocorrelation functions (ACFs) G(τ) required to use at least 2 components, which originate from the fluorescence emission of the FITC-labeled dextrans and, in addition, of residuals of free FITC molecules (i.e., not being conjugated to dextran). The FCS ACF G(τ) was therefore described using the equation

$$G(\tau) = T(\tau) \cdot (G_{\mathrm{F}}(\tau) + G_{\mathrm{DF}}(\tau)) \,, \tag{S2}$$

in which $G_{\mathrm{F}}(\tau)$ and $G_{\mathrm{DF}}(\tau)$ give the contributions from free FITC molecules and FITC-labeled dextrans, respectively, while the term $T(\tau)$ accounts for triplet state dynamics according to

$$T(\tau) = \frac{\left(1 - \Phi_{\mathrm{T}} + \Phi_{\mathrm{T}} e^{-\frac{\tau}{\tau_{\mathrm{T}}}}\right)}{1 - \Phi_{\mathrm{T}}}, \tag{S3}$$

with Φ_{T} denoting the fraction of molecules in the triplet state and τ_{T} the corresponding decay time of triplet states [1].

The contribution of the free FITC molecules was modeled using the theoretically derived ACF for free diffusion in 3D

$$G_{\mathrm{F}}(\tau) = \rho_{\mathrm{F}} \left(1 + \frac{\tau}{\tau_{\mathrm{F}}}\right)^{-1} \left(1 + \frac{\tau}{\tau_{\mathrm{F}}\kappa^2}\right)^{-\frac{1}{2}}, \tag{S4}$$

in which ρ_{F} denotes the average number density of free FITC molecules in the confocal readout volume, τ the lag time of the ACF, κ the ratio of axial r_{z} to radial extension r_{xy} of the confocal readout volume, and τ_{F} the decay time [2]. The value of τ_{F} was determined from calibration measurements on FITC molecules diffusing in buffer and κ was fixed to 6 [3], so that only the density ρ_{F} was a free parameter when fitting the component $G_{\mathrm{F}}(\tau)$ to experimentally determined ACF.

Since the dextrans showed a log-normal size distribution, as observed in the GPC measurements, the component of FITC-labeled dextrans of the ACF, $G_{\mathrm{DF}}(\tau)$, was modeled by the superposition

$$G_{\mathrm{DF}}(\tau) = \sum_i p_{\mathrm{i}} G_{\mathrm{DF,i}}(\tau), \tag{S5}$$

using the log-normally distributed weights

$$p_{\mathrm{i}} := \frac{1}{\tau_{\mathrm{DF,i}} \sigma_{\mathrm{DF}} \sqrt{2\pi}} e^{-\frac{\left(\ln(\tau_{\mathrm{DF,i}}) - \mu_{\mathrm{DF}}\right)^2}{2\sigma_{\mathrm{DF}}^2}}, \tag{S6}$$

and the corresponding ACF contributions

$$G_{\mathrm{DF,i}}(\tau) := \rho_{\mathrm{DF}} \left(1 + \frac{\tau}{\tau_{\mathrm{DF,i}}}\right)^{-1} \left(1 + \frac{\tau}{\tau_{\mathrm{DF,i}}\kappa^2}\right)^{-\frac{1}{2}}. \tag{S7}$$

The parameter σ_{DF}, which determines the broadness of the log-normal distribution, was determined by matching the FCS-related polydispersity index (PDI), defined by

$$PDI_{\mathrm{FCS}} = \frac{\sum_i p_i M_i^2}{\left(\sum_i p_i M_i\right)^2} \tag{S8}$$

using

$$M_i \propto R_i^3, \tag{S9a}$$

$$R_i = \frac{k_{\mathrm{B}} T}{6\pi\eta D_i}, \tag{S9b}$$

$$D_i = \frac{r_{\mathrm{xy}}^2}{4\tau_{\mathrm{DF,i}}}, \tag{S9c}$$

where the PDI of the dextran mass distribution was determined using GPC. The parameters ρ_{DF} and $\tau_{\mathrm{DF}} = e^{\mu_{\mathrm{DF}}}$ denote the average number density of FITC-labeled dextran molecules in the confocal readout volume and their average decay time, respectively, and were determined when fitting the component $G_{\mathrm{DF}}(\tau)$ to the experimentally determined ACF.

Fitting the 2-component model therefore yields information about the number densities of free FITC molecules and FITC-labeled dextran molecules in the confocal readout volume (ρ_{F} and ρ_{DF}, respectively) and their decay times τ_{F} and τ_{DF}, which can be translated into diffusion coefficients using

$$D_{\mathrm{F}} = \frac{r_{\mathrm{xy}}^2}{4\tau_{\mathrm{F}}} \tag{S10a}$$

$$D_{\mathrm{DF}} = \frac{r_{\mathrm{xy}}^2}{4\tau_{\mathrm{DF}}}, \tag{S10b}$$

and into hydrodynamic radii using the Stokes-Einstein relation [2].

Drifts in the Measured Fluorescence Intensity Data.

The experimentally measured fluorescence intensity data displays a continuous drift in the signal in all recorded measurements, which is likely due to an automatic re-adjustment of the laser intensity in the used setup. An example of the observed drift in the raw un-scaled signal is shown in Figure S2, recorded for $M_{\mathrm{dex}} = 70$ kDa dextran molecules at the *hPG-G10* interface. Even though almost no penetration of the large dextran molecules into the hydrogel is observed, the fluorescence intensity in the probed part of the bulk solution changes significantly over time. In order to obtain physical values for the dextran concentration, the measured profiles are being re-scaled during the fitting procedure. The obtained re-scaling factors for every measured concentration profile $\vec{f}$ decline over time, thus overcoming the constant increase of signal intensity due to the drift (see Figure S3A). Additionally, smaller changes in the fluorescence intensity are apparent. Since robust results are obtained by employing this re-scaling routine, this suggests that the entire information about the diffusion process is present in the relative shape of the concentration profiles.

The obtained re-scaling factor can additionally be used, to estimate the experimental bulk concentration c_{bulk} far away from the hydrogel interface, based on the experimentally measured profiles alone, without using the numerically computed dextran distributions. The total amount of dextran in the system C_{tot} is computed from the first concentration profile as $C_{\mathrm{tot}} = \int_{-\infty}^{\infty} c(z, t = 0)\, dz$, where $c(z, t = 0)$ was approximated by c_i^{init} according to equation (5) in the main text. An average experimental concentration in the bulk region $\bar{c}_{\mathrm{bulk}}(t_{\mathrm{j}})$ can then be estimated from the fitted re-scaling factors as

$$\bar{c}_{\mathrm{bulk}}(t_{\mathrm{j}}) = \frac{C_{\mathrm{tot}} - \sum_{i=1}^{M} f_{\mathrm{j}} \cdot c_i^{\mathrm{exp}}(t_j) \cdot \Delta z_i}{z_{\mathrm{top}}}, \tag{S11}$$

Values for $\bar{c}_{\mathrm{bulk}}(t_{\mathrm{j}})$ are shown in Figure S3B and are virtually constant for the exemplary measurement of $M_{\mathrm{dex}} = 70$ kDa dextrans, as is expected due to the absence of penetration into the hydrogel.

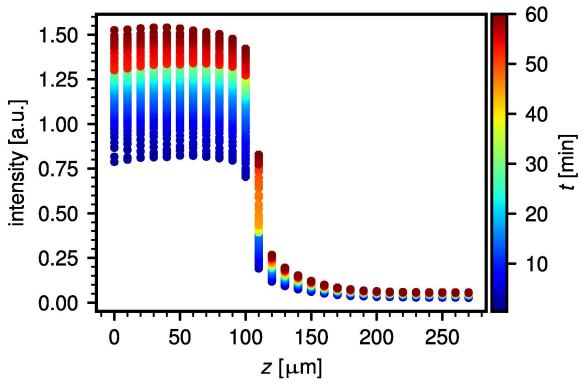

Supplementary Figure S2. Raw fluorescence intensity data from experiments of $M_{\mathrm{dex}} = 70$ kDa dextrans in combination with the *hPG-G10* hydrogel. A significant change in the signal over time is observed in the probed part of the bulk solution, even though almost no penetration of the dextrans into the hydrogel is apparent. This drift in the experimentally measured signal is overcome by the numerically determined re-scaling factors.

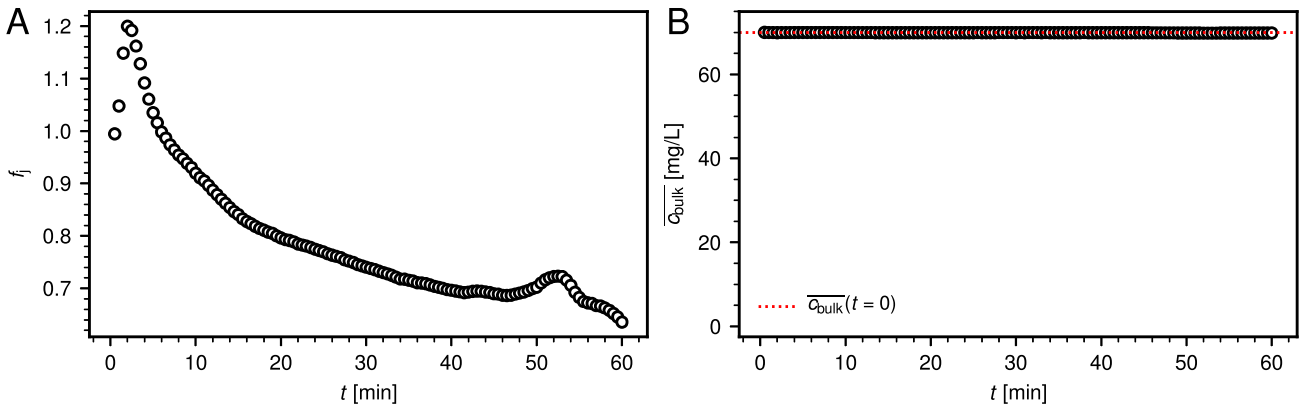

Supplementary Figure S3. A: Set of re-scaling factors $\vec{f}$ for every measured concentration profile obtained from numerical analysis of experimental data from $M_{\mathrm{dex}} = 70$ kDa dextrans at the *hPG-G10* hydrogel interface. Decreasing re-scaling factors counteract the drift observed in the raw experimental data. Additionally, peaks in the re-scaling factor distribution are observed, counteracting shorter fluctuations in the fluorescence intensity. B: Average bulk concentration $\overline{c_{\mathrm{bulk}}}$ computed according to equation (S11) for the same measurements. The bulk concentration remains constant in this measurement, since almost no dextran penetrates into the hydrogel.

Analytical Solution for Two-Segment System.

Simplifying the hydrogel-water setup as a two-box system with piece-wise constant values of the free energy and diffusion constant in the two regions allows for an analytical solution of the diffusion problem. The modeled system with the corresponding boundary conditions is sketched in Figure S4A.

We solve the following diffusion equation in each of the two segments

$$\frac{\partial}{\partial t}c(z,t) = D(z)\frac{\partial^2}{\partial z^2}c(z,t), \tag{S12}$$

where the diffusion constant $D(z)$ has a different value in each of the two regions

$$D(z) = \begin{cases} D_0, & 0 \le z \le z_{\text{int}} \\ D_1, & z_{\text{int}} < z \le z_{\text{bot}}, \end{cases} \tag{S13}$$

as does the free energy $F(z)$, which we set to zero in the left segment as reference

$$F(z) = \begin{cases} F_0 = 0, & 0 \le z \le z_{\text{int}} \\ F_1, & z_{\text{int}} < z \le z_{\text{bot}}. \end{cases} \tag{S14}$$

At the interface z_{int}, the flux needs to be continuous due to mass conservation, while the jump in the free energy leads to a jump in the concentration profile $c(z = z_{\text{int}}, t)$. This defines the boundary conditions at z_{int} as

$$\lim_{z \nearrow z_{\text{int}}} D_0 \frac{\partial}{\partial z}c(z,t) = \lim_{z \searrow z_{\text{int}}} D_1 \frac{\partial}{\partial z}c(z,t) \tag{S15a}$$

$$\lim_{z \nearrow z_{\text{int}}} c(z,t)e^{-\beta F_1} = \lim_{z \searrow z_{\text{int}}} c(z,t). \tag{S15b}$$

Since we are modeling a closed system, the edges at $z = 0$ and $z = z_{\text{bot}}$ are reflecting boundaries with

$$\frac{\partial}{\partial z}c(z = 0, t) = 0 \tag{S16a}$$

$$\frac{\partial}{\partial z}c(z = z_{\text{bot}}, t) = 0. \tag{S16b}$$

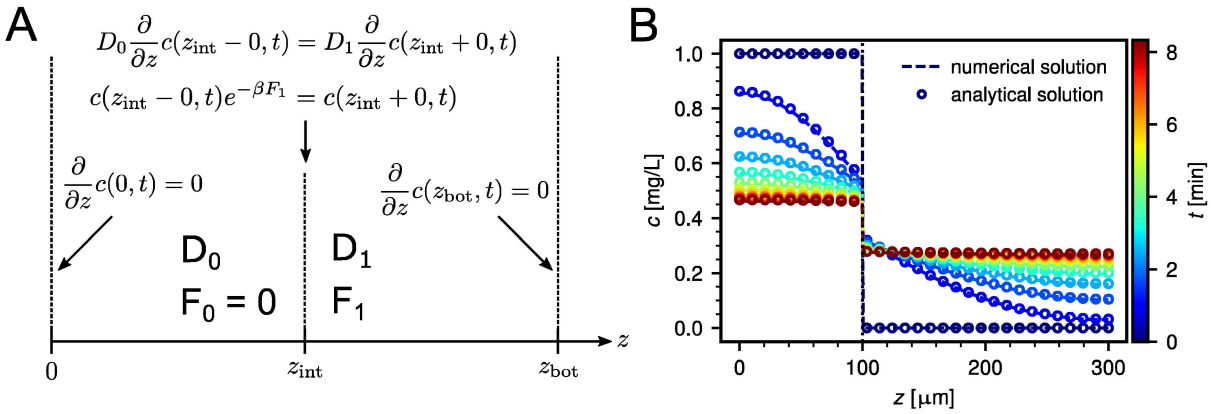

Supplementary Figure S4. Approximation of the dextran hydrogel setup as a two-segment system, which can be solved analytically. A: Two-segment system with different diffusion constants and a jump in the free energy at the interface z_{int}. The used boundary conditions are also indicated. B: Comparison of the numerical model and the analytical solution of the system explained in A, with values for the parameters of $z_{\text{int}} = 100$ μm, $z_{\text{bot}} = 300$ μm, $c_0 = 1$, $D_0 = 50$ $\mu\text{m}^2/s$, $D_1 = 100$ $\mu\text{m}^2/s$ and $F_1 = 0.5$ $k_{\text{B}}T$.

Initially, the diffusors are only present in the left segment, modeling the bulk solution. This defines our initial condition as

$$c(z, t=0) = \begin{cases} c_0, & 0 \leq z \leq z_{\text{int}} \\ 0, & z_{\text{int}} < z \leq z_{\text{bot}}. \end{cases} \tag{S17}$$

We now solve equation (S12) by means of Laplace transformation. To this end, we use the single sided Laplace transform in time, defined as $\hat{f}(s) := \int_0^\infty f(t)e^{-st}dt$, where s is the complex variable in Laplace space $s = \sigma + i\omega$. This converts the partial differential equation (S12) into an ordinary differential equation of second order

$$\left[s - D(z)\frac{\partial^2}{\partial z^2} \right] \hat{c}(z, s) = c(z, t=0). \tag{S18}$$

The general solution of equation (S18) for the two regions reads

$$\hat{c}(z, s) = \begin{cases} a_1 e^{\lambda_0 z} + a_2 e^{-\lambda_0 z} + \hat{c}_{\text{p}}, & 0 \leq z \leq z_{\text{int}} \\ a_3 e^{\lambda_1 z} + a_4 e^{-\lambda_1 z}, & z_{\text{int}} < z \leq z_{\text{bot}}, \end{cases} \tag{S19}$$

where we define $\lambda_{\text{i}} := \sqrt{\frac{s}{D_{\text{i}}}}, i = 0, 1$ and $\hat{c}_{\text{p}} := \frac{c_0}{s}$. The coefficients a_i of equation (S19) are determined by solving the system of linear equations obtained by Laplace transforming the boundary conditions of equations (S15) and (S16) and substituting the general solution (S19). After some algebra, the solution to the posed problem is obtained as

$$\hat{c}(z, s) = \begin{cases} \hat{c}_{\text{p}} \frac{K \cdot \tanh(\lambda_1(z_{\text{bot}} - z_{\text{int}}))[\cosh(\lambda_0 z_{\text{int}}) - \cosh(\lambda_0 z)] + \sinh(\lambda_0 z_{\text{int}})\sqrt{\delta}}{K \cdot \tanh(\lambda_1(z_{\text{bot}} - z_{\text{int}}))\cosh(\lambda_0 z_{\text{int}}) + \sinh(\lambda_0 z_{\text{int}})\sqrt{\delta}}, & 0 \leq z \leq z_{\text{int}} \\ \hat{c}_{\text{p}} \frac{K \cdot \cosh(\lambda_1(z_{\text{bot}} - z))\tanh(\lambda_0 z_{\text{int}})\sqrt{\delta}}{K \cdot \sinh(\lambda_1(z_{\text{bot}} - z_{\text{int}})) + \tanh(\lambda_0 z_{\text{int}})\cosh(\lambda_1(z_{\text{bot}} - z_{\text{int}}))\sqrt{\delta}}, & z_{\text{int}} < z \leq z_{\text{bot}}, \end{cases} \tag{S20}$$

where $\delta := \frac{D_0}{D_1}$ and $K := e^{-\beta F_1}$.

The solution in Laplace space (S20) is then transformed into real space by use of the Mellin integral

$$\begin{aligned} c(z, t) &= \frac{1}{2\pi i} \int_{s=\sigma-i\infty}^{s=\sigma+i\infty} \hat{c}(z, s) e^{st} \, ds \\ &= \frac{e^{\sigma t}}{2\pi} \int_{-\infty}^{+\infty} \hat{c}(z, \sigma + i\omega) e^{i\omega t} \, dw, \end{aligned} \tag{S21}$$

where the last integral was solved numerically through the inverse discrete Fourier transform.

Figure S4B shows a comparison of the analytical solution and the numerical model for an exemplary parameter set of $z_{\text{int}} = 100$ μm, $z_{\text{bot}} = 300$ μm, $c_0 = 1$ mg/L, $D_0 = 50$ $\mu\text{m}^2/s$, $D_1 = 100$ $\mu\text{m}^2/s$ and $F_1 = 0.5$ $k_{\text{B}}T$, mimicking a slight immobilization and repulsion in the right segment, as observed for the smaller dextrans in the experiments (see main text). The stationary state is reached faster in the approximate system compared to the actual measurements in the main text, due to the much smaller z-dimension. Perfect agreement between the numerical model and the analytical solution is obtained.

Error Estimate for Numerical Analysis.

In order to determine confidence intervals for the fitted parameters of D_{sol}, D_{gel} and ΔF_{gel}, the values are varied from the optimum until the agreement with the experimental data is 50% worse than for the optimal parameter values. Figure S5 shows an exemplary analysis of the fitted parameters influence on the error. All parameters are varied independently, meaning that the error is always computed while keeping all other parameters fixed at their optimal values. Also, the fitted values for d_{int} and z_{int} are not changed but kept at their optimum. It is apparent that increasing the fitted diffusion constants does not affect the agreement with the experimental data as strongly as a decrease (see Figure S5A and B). Changing the free energy difference influences the numerical error σ more symmetrically, meaning increasing ΔF_{gel} has the same influence on the error as decreasing it.

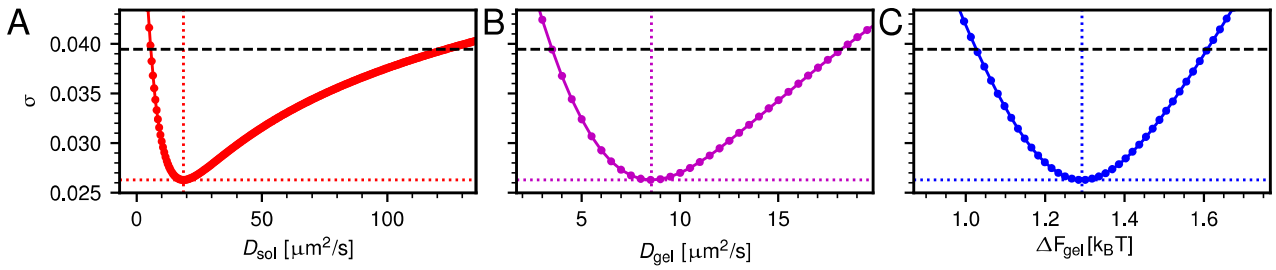

Supplementary Figure S5. Error estimation of the fitted values for D_{sol} (A), D_{gel} (B) and ΔF_{gel} (C) for measurements of $M_{\mathrm{dex}} = 40$ kDa dextran molecules diffusing into the *hPG-G10* hydrogel. Fitted optimal values for the parameters are indicated by dotted lines, while a 50% change in σ is shown by the dashed black line. A larger value of the diffusion constants does not affect the agreement with the experimental data as strongly as a smaller value.

Scaling of Diffusion Constant with Dextran Size.

According to the Stokes-Einstein relation the diffusion constant of dextran molecules in the bulk solution D_{sol} is expected to scale with the dextran radius r_0 as

$$D_{\mathrm{sol}} \propto r_0^{-1}. \tag{S22}$$

Assuming the dextran polymer behaves like a freely jointed chain, its radius should relate to the number of monomers N as [4, 5]

$$r_0 = b\sqrt{N}, \tag{S23}$$

where b is the monomer length and N can be estimated from the total molecular mass of a dextran molecule M_{dex}, when the monomer mass $M_{\mathrm{dex}}^{\mathrm{mono}}$ is known

$$N = \frac{M_{\mathrm{dex}}}{M_{\mathrm{dex}}^{\mathrm{mono}}}. \tag{S24}$$

This leads to the following equality

$$D_{\mathrm{sol}} = \frac{k_{\mathrm{B}}T}{6\pi\eta \frac{b}{\sqrt{M_{\mathrm{dex}}^{\mathrm{mono}}}}\sqrt{M_{\mathrm{dex}}}}, \tag{S25}$$

which gives rise to a scaling of $D_{\mathrm{sol}} \propto M_{\mathrm{dex}}^{-1/2}$.

Expression for the Elastic Deformation Free Energy.

The free energy cost for stretching a polymer chain from an initial equilibrium mean square end-to-end distance $\langle \vec{R}_0^2 \rangle$ to a larger end-to-end distance $\langle \vec{R}^2 \rangle$ can be written as [4, 5]

$$\Delta F_{\text{stretch}} = \frac{3}{2} k_{\text{B}} T \frac{\langle \vec{R}^2 \rangle - \langle \vec{R}_0^2 \rangle}{\langle \vec{R}_0^2 \rangle}, \tag{S26}$$

where $k_{\text{B}}T$ denotes the thermal energy. In the case of the PEG-linkers we define the z-component of the end-to-end distance as $l := \langle R_z \rangle$, so that $l_0 := \langle R_{0,z} \rangle$. The PEG polymer chain is now only stretched in the z-direction, thus equation (S26) reduces to

$$\Delta F_{\text{stretch}} = \frac{3}{2} k_{\text{B}} T \frac{\langle R_x^2 \rangle + \langle R_y^2 \rangle + l^2 - \langle R_{0,x}^2 \rangle - \langle R_{0,y}^2 \rangle - l_0^2}{\langle \vec{R}_0^2 \rangle} = \frac{3}{2} k_{\text{B}} T \frac{l^2 - l_0^2}{\langle \vec{R}_0^2 \rangle}, \tag{S27}$$

since $\langle R_x^2 \rangle = \langle R_{0,x}^2 \rangle$ and $\langle R_y^2 \rangle = \langle R_{0,y}^2 \rangle$. As the PEG polymer chain performs a random walk in all three spatial dimensions, all components of the mean squared end-to-end distance contribute equally and so

$$\frac{\langle \vec{R}_0^2 \rangle}{3} = \langle R_{0,x}^2 \rangle = \langle R_{0,y}^2 \rangle = \langle R_{0,z}^2 \rangle = l_0^2. \tag{S28}$$

Together with equation (S27), equation (S28) leads to the stretching free energy for a single PEG-linker polymer chain

$$\Delta F_{\text{stretch}} = \frac{1}{2} k_{\text{B}} T \left[\frac{l^2}{l_0^2} - 1 \right]. \tag{S29}$$

For the compression of a polymer chain from an initially larger mean square end-to-end distance $\langle \vec{R}_0^2 \rangle$ to a smaller one $\langle \vec{R}^2 \rangle$ we write [4, 5]

$$\Delta F_{\text{compress}} = \frac{3}{2} k_{\text{B}} T \frac{\langle \vec{R}_0^2 \rangle - \langle \vec{R}^2 \rangle}{\langle \vec{R}^2 \rangle}. \tag{S30}$$

In the same way as above, we only allow compression along the z-axis, which leads to

$$\Delta F_{\text{compress}} = \frac{3}{2} k_{\text{B}} T \frac{\langle R_{0,x}^2 \rangle + \langle R_{0,y}^2 \rangle + l_0^2 - \langle R_x^2 \rangle - \langle R_y^2 \rangle - l^2}{\langle R_x^2 \rangle + \langle R_y^2 \rangle + l^2} = \frac{3}{2} k_{\text{B}} T \frac{l_0^2 - l^2}{\langle R_{0,x}^2 \rangle + \langle R_{0,y}^2 \rangle + l^2}. \tag{S31}$$

Using equation (S28) to substitute the x- and y-components of the equilibrium end-to-end distance gives the expression for the compression free energy of a single PEG-linker

$$\Delta F_{\text{compress}} = \frac{1}{2} k_{\text{B}} T \frac{3l_0^2 - 3l^2}{2l_0^2 + l^2}. \tag{S32}$$

The total elastic deformation free energy per PEG-linker is the sum of equations (S29) and (S32)

$$\Delta F_{\text{PEG}} = \frac{1}{2} k_{\text{B}} T \left(\left[\frac{l}{l_0} \right]^2 + \frac{l_0^2 - 4l^2}{2l_0^2 + l^2} \right). \tag{S33}$$

Estimating PEG-Monomer Hydration Numbers.

Based on equations (8) and (13) from the main text, we obtain the following relation between the partition coefficient K and the volume accessible to the dextran diffusors V_{acc}

$$K = \frac{V_{\mathrm{acc}}}{V_{\mathrm{tot}}} e^{-\beta(\Delta F_{\mathrm{dex}} + \Delta F_{\mathrm{PEG}})}. \tag{S34}$$

The volume inaccessible to the dextran molecules V_{inacc} is either occupied by the gel components or by tightly bound hydration water, so that

$$V_{\mathrm{inacc}} = V_{\mathrm{tot}} - V_{\mathrm{acc}} = V_{\mathrm{gel}} + V_{\mathrm{hyd}}, \tag{S35}$$

where $V_{\mathrm{gel}} = V_{\mathrm{PEG}} + V_{\mathrm{hPG}}$ denotes the inaccessible volume due to the gel components and V_{hyd} is the volume occupied by hydration water. The mass fraction Φ_{gel} of the gel components inside the hydrogel is defined as the ratio of the mass of the gel components m_{gel} to the total mass m_{tot}, but since the mass density of the gel components is comparable to that of water, it also represents the fraction of inaccessible volume due to the gel components

$$\Phi_{\mathrm{gel}} := \frac{m_{\mathrm{gel}}}{m_{\mathrm{tot}}} \approx \frac{V_{\mathrm{gel}}}{V_{\mathrm{tot}}}. \tag{S36}$$

In the same fashion we can also estimate the fraction of inaccessible volume due to only the PEG linkers as

$$\Phi_{\mathrm{PEG}} = \frac{m_{\mathrm{PEG}}}{m_{\mathrm{tot}}} = \frac{n_{\mathrm{PEG}} M_{\mathrm{PEG}}}{m_{\mathrm{tot}}} \frac{V_{\mathrm{app}}}{V_{\mathrm{gel}}^{\mathrm{sol}}} \approx \frac{V_{\mathrm{PEG}}}{V_{\mathrm{tot}}}, \tag{S37}$$

where we use the values for the number n_{PEG} and the molar mass M_{PEG} of the PEG linkers given in the Methods section in the main text. The factor of $V_{\mathrm{app}}/V_{\mathrm{gel}}^{\mathrm{sol}}$ accounts for the fact that only $V_{\mathrm{app}} = 1\ \mu\mathrm{L}$ of the total volume of prepared gel solution $V_{\mathrm{gel}}^{\mathrm{sol}}$ are actually placed on the gel spot for the experiments (see Methods section for details). The total mass of the hydrogel m_{tot} is estimated from the measured hydrogel volumes by using the water mass density (see Methods section). Combining equations (S34), (S35) and (S36) from above gives the following expression for volume fraction occupied by hydration water

$$\frac{V_{\mathrm{hyd}}}{V_{\mathrm{tot}}} = 1 - \Phi_{\mathrm{gel}} - K e^{\beta(\Delta F_{\mathrm{dex}} + \Delta F_{\mathrm{PEG}})}. \tag{S38}$$

The hydration water of equation (S38) binds to the entire hydrogel, meaning the hPG hubs and the PEG linkers. Since we here want to estimate only the number of hydration waters per PEG molecule and since the two components of the hydrogel are mixed in a ratio 3:1 of PEG linkers to hPG hubs, we assume that also only a fraction of 3/4 of the total hydration water binds to the PEG linkers, so that $V_{\mathrm{hyd}}^{\mathrm{PEG}} \approx 0.75 \cdot V_{\mathrm{hyd}}$. This assumption is justified by the comparable chemical structures of PEG and hPG molecules and thus likely comparable hydrophilicities. Using now only the mentioned fraction of the total hydration water, we can compute the fraction of hydration water per unit PEG volume from equations (S37) and (S38) as

$$\frac{V_{\mathrm{hyd}}^{\mathrm{PEG}}}{V_{\mathrm{PEG}}} = \frac{n_{\mathrm{hyd}} v_{\mathrm{w}}}{n_{\mathrm{PEG}} v_{\mathrm{PEG}}} = 0.75 \cdot \frac{1 - \Phi_{\mathrm{gel}} - K e^{\beta(\Delta F_{\mathrm{dex}} + \Delta F_{\mathrm{PEG}})}}{\Phi_{\mathrm{PEG}}}, \tag{S39}$$

where n_{hyd} is the number of hydration water molecules, v_{w} is their partial volume, n_{PEG} is the number of PEG linkers and v_{PEG} is the PEG linker partial volume. The ratio between the partial volumes of water and the PEG linkers is approximated by the ratio of their molar masses as

$$\frac{v_{\mathrm{w}}}{v_{\mathrm{PEG}}} \approx \frac{M_{\mathrm{w}}}{M_{\mathrm{PEG}}}, \tag{S40}$$

with the water molar mass $M_w = 18$ g/mol and the molar mass of the respective PEG linker M_{PEG} (see Methods section). From equation (S39), we can now compute the number of hydration waters per PEG linker molecule as

$$\frac{n_{hyd}}{n_{PEG}} = 0.75 \cdot \frac{1 - \Phi_{gel} - Ke^{\beta(\Delta F_{dex} + \Delta F_{PEG})}}{\Phi_{PEG}} \frac{M_{PEG}}{M_w}. \tag{S41}$$

In order to obtain the number of hydration waters per PEG-monomer we simply divide equation (S41) by the respective number of PEG-monomers per linker N_{PEG}^{mono}, which we obtain from the ratio of total linker mass M_{PEG} and PEG-monomer mass $M_{PEG}^{mono} = 44$ g/mol, as $N_{PEG}^{mono} = M_{PEG}/M_{PEG}^{mono}$. The number of hydration waters per PEG-monomer can thus be obtained as

$$\frac{n_{hyd}}{n_{PEG}^{mono}} = 0.75 \cdot \frac{1 - \Phi_{gel} - Ke^{\beta(\Delta F_{dex} + \Delta F_{PEG})}}{\Phi_{PEG}} \frac{M_{PEG}^{mono}}{M_w}. \tag{S42}$$

With the values of $Ke^{\beta(\Delta F_{dex} + \Delta F_{PEG})}$, Φ_{gel} and Φ_{PEG} for the two hydrogels from the main text, equation (S42) allows us to estimate the number of hydration waters per PEG monomer for all measurements. Figure S6 shows the results of the calculation for each of the two hydrogels. Estimated values range from 6 to 12 water molecules per PEG monomer. Depending on the employed experimental method, values reported in the literature vary, ranging from 2 to 11 water molecules per PEG monomer [6–10]. Additionally, an increase of the hydration waters per monomer has been observed, as a function of the polymerization degree [11]. The values obtained from our estimates, lie within the errors in the range of values reported in the literature, as indicated in Figure S6. This further corroborates our methodology and specifically the model for the free energy of equation (13) from the main text, since the estimate of equation (S42) is based on this model.

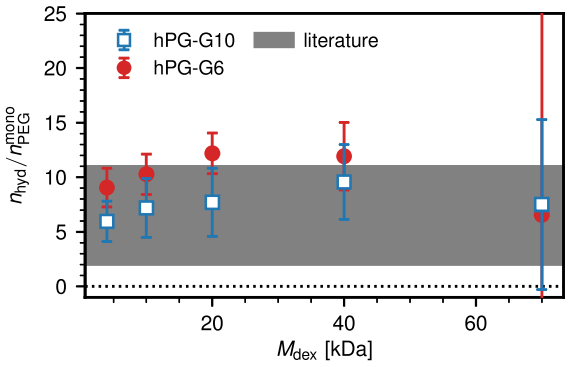

Supplementary Figure S6. Estimated number of water molecules per PEG monomer n_{hyd}/n_{PEG}^{mono} from the obtained values of K for the two hydrogels based on equation (S42). The estimated values range from $n_{hyd}/n_{PEG}^{mono} = 6$ to $n_{hyd}/n_{PEG}^{mono} = 12$ and agree within the errors to the range of values reported in the literature indicated as the grey shaded area, ranging from $n_{hyd}/n_{PEG}^{mono} = 2$ to $n_{hyd}/n_{PEG}^{mono} = 11$ [6–10].

Derivation of Expression for Permeability.

The definition of the permeability coefficient P is, as stated in the main text [12]

$$P(z_1, z_2) := \frac{J}{c(z_1) - c(z_2)}, \tag{S43}$$

with the stationary flux J and the equilibrium concentrations at both sides of the barrier $c(z_1)$ and $c(z_2)$. From the generalized diffusion equation (7) in the main text, one obtains the stationary flux for the case of $\partial c(z,t)/\partial t = 0$ as

$$J = D(z)e^{-\beta F(z)} \frac{\partial}{\partial z} \left(c(z,t) e^{\beta F(z)} \right), \tag{S44}$$

as a function of the diffusion constant $D(z)$ and the free energy landscape $F(z)$ across the barrier. After rearranging equation (S44) and integrating from one side of the barrier from z_1 to the other z_2, we obtain the following relation

$$J \int_{z_1}^{z_2} \frac{e^{\beta F(z)}}{D(z)} \, dz = c(z_1,t) e^{\beta F(z_1)} - c(z_2,t) e^{\beta F(z_2)}. \tag{S45}$$

We now assume that the free energy value is the same on both sides of the barrier and additionally set it to zero as reference so that $F(z_1) = F(z_2) = 0$ and thus

$$J \int_{z_1}^{z_2} \frac{e^{\beta F(z)}}{D(z)} \, dz = c(z_1,t) - c(z_2,t), \tag{S46}$$

which, in combination with equation (S43), gives the expression used in the main text

$$\frac{1}{P} = \int_{z_1}^{z_2} \frac{e^{\beta F(z)}}{D(z)} \, dz. \tag{S47}$$

---

* These two authors contributed equally to this work.
† rnetz@physik.fu-berlin.de

[1] J. Widengren, R. Rigler, and Ü. Mets, Journal of Fluorescence **4**, 255 (1994).
[2] R. Rigler and E. S. Elson, *Fluorescence Correlation Spectroscopy: Theory and Applications*, Springer Series in Chemical Physics (Springer Berlin Heidelberg, 2012).
[3] S. Rüttinger, V. Buschmann, B. Krämer, R. Erdmann, R. MacDonald, and F. Koberling, Journal of Microscopy **232**, 343 (2008).
[4] M. Rubinstein and R. H. Colby, *Polymer Physics* (OUP Oxford, 2003).
[5] R. R. Netz and D. Andelman, Physics Reports **380**, 1 (2003).
[6] L. Huang and K. Nishinari, Journal of Polymer Science, Part B: Polymer Physics **39**, 496 (2001).
[7] T. Shikata, R. Takahashi, and A. Sakamoto, The Journal of Physical Chemistry B **110**, 8941 (2006).
[8] U. Kaatze, O. Gottmann, R. Podbielski, R. Pottel, and U. Terveer, The Journal of Physical Chemistry **82**, 112 (1978).
[9] T. W. N. Bieze, A. C. Barnes, C. J. M. Huige, J. E. Enderby, and J. C. Leyte, The Journal of Physical Chemistry **98**, 6568 (1994).
[10] W. Żwirbla, A. Sikorska, and B. B. Linde, Journal of Molecular Structure **743**, 49 (2005).
[11] C. Branca, S. Magazù, G. Maisano, F. Migliardo, P. Migliardo, and G. Romeo, The Journal of Physical Chemistry B **106**, 10272 (2002).
[12] J. M. Diamond and Y. Katz, The Journal of Membrane Biology **17**, 121 (1974).

5 Summary and Conclusion

This work deals with hydrogels based on linear bifunctional polyethylene glycol (PEG-BCN) and azide-functionalized hyperbranched polyglycerol (hPG-N_3), which were crosslinked by the bioorthogonal strain-promoted azide-alkyne cycloaddition. The hydrogel was immobilized onto different kind of surfaces, including glass slides, 96-well plates, cover slips, and Nunc NucleoLink stripes. The gels were linked to the surfaces by both covalent and adsorptive bonds. Common to all projects was the design of the hydrogel, which consisted of the two bioinert, hydrophilic, and tunable macromonomers PEG-BCN and hPG-N_3. Tuning the PEG length altered the mesh size, the mechanical properties, and the swelling behavior. Using the multivalent hPG allowed us to introduce further functions to the hydrogel, depending on the demands of the application.

In the first project, we successfully investigated the hydrogel as a new biosensor matrix for the in situ, non-covalent entrapment of streptavidin and an antibody. We could show that the loading was drastically increased as compared to two-dimensional surfaces, the binding sites were still accessible, and small molecules (such as biotin and the FLAG peptide) would not stick to the gel unless their complementary binding partner was present. To detect a smaller oligonucleotide, however, it had to be anchored covalently to the hubs of the network. In a hybridization assay with fluorescence-labeled targets, the loading capacity was increased, and the sensitivity improved. This was attributed to the higher surface area of the hydrogel compared to flat surfaces, and to the better accessibility of each probe by the target due to the solution-like environment. Furthermore, the hydrogel-based biosensor was recovered for at least five cycles, and the hydrogel was stable against heat and against treatment with a strong base. The possibility of spotting the probe-containing hydrogel showed the potential for this method to be implemented in industrial applications.

In the second project, our hydrogel was introduced into a microparticle-based planar multiplex assay. The hydrogel increased the multiplexicity by coding the microparticles not only in x,y-position but in x,y,*k*-position. The detection in *k* levels by a fluorescence microscope equipped with the VideoScan software created a novel three-dimensional assay format. Additionally, the hydrogel network formed a filter on the molecular level that controlled the pathways of differently sized target analytes into the respective levels. We were able to show that the sieve effect, i.e. the size exclusion, allowed us to separately detect oligonucleotides, Fab fragments, and entire IgG antibodies in a single assay. We not only

investigated the assay performance but also characterized the hydrogel and its size-exclusion capability. We showed that the hydrogel was able to embed and immobilize fluorescent microparticles at different positions without disturbing the performance of the hybridization and immunoassay. Once the microparticles were set in the matrix they remained fixed during all assay procedures (incubation, washing, drying, etc.). Moreover, the whole system was subject to several circles of swelling and drying, during which the hydrogel managed to repeatedly separate two layers of microbeads.

Encouraged by the diffusion behavior of the differently sized biomolecules, the third project aimed to develop a method for the simultaneous extraction of diffusivity and free-energy profiles of particles that permeate into our hydrogel system. Therefore, we studied the diffusion of five differently sized, fluorescence-labeled dextrans into two hydrogels with different PEG linker lengths. The fluorescence intensity data of the labeled dextrans, recorded using a standard confocal fluorescence microscopy setup, was sufficient for this approach. The numerical analysis of the experimental measurements provided a complete model of the penetration process. This allowed access to the dextran distribution over time across the entire bulk solution (which would not be accessible experimentally) and in the hydrogel, while at the same time extracting diffusion constants and partition coefficients. The results we obtained matched nicely with complementary fluorescence correlation spectroscopy (FCS) measurements and data from literature. From the partitioning of the dextran molecules we developed a free volume model that also accounts for the elastic flexibility of both the dextran and PEG polymers. We obtained an estimated mesh size, which indicated a heterogeneous gel structure involving a broad pore size distribution.

6 Outlook

This work demonstrates the excellent features of a hydrogel based on the bioorthogonal SPAAC reaction between two macromonomers. The comprehensive characterization and investigation of the hydrogel's features lead us to believe that this approach of combining PEG and hPG has more to offer for future projects. One perspective to increase the scope of this research is to build a set of polymers, where the chemical crosslinking is modular and thus, can be adapted depending on the requirements. The introduction of aldehyde groups to the hPG, for example, would be reactive towards naturally occurring amines and thus, be used for the immobilization of biomolecules. The resulting imine bond would either be reduced to a stable amine or, if needed, the biomolecule could get cleaved off again. Additionally, the number of available aldehydes in the hydrogel is adjustable, which would give control over the biomolecule immobilization efficiency. In combination with the adjustable swelling and stiffness of the hydrogel, the surface structure and roughness can be altered. This would make the hydrogel an ideal surface coating or an ideal substrate itself for point-of-care technologies.

The newly developed experimental setup to study diffusion of labeled molecules through hydrogels should further be exploited with biologically relevant molecules. We optimized the setup for out model systems and could show that it works. As a follow-up, interesting results regarding e.g. the interaction of viruses or charged molecules with mucus could be obtained from the penetration profiles. Since any kind of hydrogel (synthetic, natural, biomimetic, etc.) could be immobilized on the coverslip and be combined with any kind of diffusor (with a fluorescence label), this has a huge potential in studying biologically important process.

7 Zusammenfassung

Diese Arbeit befasst sich mit Hydrogelen auf der Basis von linearem bifunktionellem Polyethylenglykol (PEG-BCN) und azidfunktionalisiertem, hyperverzweigtem Polyglycerin (hPG), die durch die bioorthogonale spannungsvermittelte Azid-Alkin-Cycloaddition (SPAAC, engl. Strain-promoted azide-alkyne cycloaddition) vernetzt wurden. Das Hydrogel wurde auf verschiedenen Arten von Oberflächen immobilisiert, darunter Glasobjektträger, 96-Well-Platten, Deckgläser und Nunc NucleoLink-Streifen. Die Gele waren sowohl durch kovalente als auch durch adsorptive Bindungen mit den Oberflächen verbunden. Allen Projekten gemeinsam war das Design des Hydrogels, das aus den beiden bioinerten, hydrophilen und modifizierbaren Makromonomeren bestand. Die Einstellung der PEG-Länge veränderte die Maschenweite, die mechanischen Eigenschaften und das Quellverhalten. Die Verwendung des multivalenten hPGs erlaubte es, dem Hydrogel je nach den Anforderungen der Anwendung weitere Funktionen zuzuführen.

Im ersten Projekt wurde das Hydrogel erfolgreich als neue Biosensor-Matrix für den in situ, nicht-kovalenten Einschluss von Streptavidin und einem Antikörper eingesetzt. Wir konnten zeigen, dass die Beladung im Vergleich zu 2D-Oberflächen drastisch erhöht war, die Bindungsstellen noch zugänglich waren und kleine Moleküle (wie Biotin und das FLAG-Peptid) nicht am Gel haften blieben, wenn ihr komplementärer Bindungspartner nicht vorhanden war. Das kleinere Oligonukleotid musste jedoch kovalent an den Knotenpunkten des Netzwerks verankert werden. In einem Hybridisierungsassay mit fluoreszenzmarkierten Targets wurde die Beladungskapazität erhöht und die Sensitivität verbessert. Dies wurde zurückgeführt auf die größere Oberfläche des Hydrogels im Vergleich zu flachen Oberflächen und auf die bessere Zugänglichkeit jeder Sonde durch das Target aufgrund der lösungsähnlichen Umgebung. Darüber hinaus wurde der Biosensor auf Hydrogel-Basis mindestens über fünf Zyklen regeneriert, und das Hydrogel war gegen Hitze und Behandlung mit einer starken Base stabil. Die Möglichkeit, die Sonde zusammen mit dem Hydrogel zu spotten, zeigte das Potenzial, unser System auch in industriellem Kontext anzuwenden.

Im zweiten Projekt wurde das Hydrogel in einen planaren Multiplex-Assay auf Mikropartikelbasis eingeführt. Das Hydrogel erhöhte die Multiplexität, indem es die Mikropartikel nicht nur in x,y-Position, sondern in x,y,*k*-Position kodierte. Die Detektion in *k*-Stufen durch ein Fluoreszenzmikroskop, das mit der VideoScan-Software ausgestattet war, schuf ein neuartiges 3-dimensionales Assay-Format. Zusätzlich bildete das

Hydrogelnetzwerk einen Filter auf molekularer Ebene, der den Weg von unterschiedlich großen Zielanalyten in die jeweiligen Ebenen kontrollierte. Wir konnten zeigen, dass der Siebeffekt, d.h. der Größenausschluss, den getrennten Nachweis von Oligonukleotiden und Immunglobulinen (ganze Antikörper vom IgG-Typ) und Fab-Fragmenten in einem Assay ermöglichte. Wir untersuchten nicht nur die Leistungsfähigkeit des Assays, sondern charakterisierten auch das Hydrogel und seine Fähigkeit zum Größenausschluss. Wir zeigten, dass das Hydrogel in der Lage war, fluoreszierende Mikropartikel an verschiedenen Positionen einzubetten und zu immobilisieren, ohne die Leistung der Hybridisierung und des Immunoassays zu stören. Sobald die Mikropartikel in der Matrix fixiert waren, blieben sie während aller Testverfahren (Inkubation, Waschen, Trocknen usw.) fixiert. Darüber hinaus wurde das gesamte System während mehrerer Zyklen gequollen und getrocknet, wobei es dem Hydrogel gelang, zwei Schichten von Mikrobeads wiederholt zu trennen.

Angeregt durch das Diffusionsverhalten der Biomoleküle unterschiedlicher Größe zielte das dritte Projekt darauf ab, eine Methode zur gleichzeitigen Extraktion von Diffusivitäts- und freien Energieprofilen von Partikeln zu entwickeln, die in unser Hydrogelsystem eindringen. Dafür wurde die Diffusion von fünf unterschiedlich großen, fluoreszenzmarkierten Dextranen in zwei Hydrogele mit unterschiedlichen PEG-Linkerlängen untersucht. Die Fluoreszenzintensitätsdaten der markierten Dextrane, die mit einem konfokalen Standard-Fluoreszenzmikroskopie-Setup aufgezeichnet wurden, waren für diese Anforderungen ausreichend. Die numerische Analyse der experimentellen Messungen lieferte ein vollständiges Modell des Penetrationsprozesses. Dies ermöglichte den Zugriff auf die zeitliche Verteilung von Dextran über die gesamte Bulklösung (die experimentell nicht zugänglich wäre) und im Hydrogel, während gleichzeitig Diffusionskonstanten und Verteilungskoeffizienten extrahiert wurden. Die erhaltenen Ergebnisse stimmten gut mit Messungen der Fluoreszenzkorrelationsspektroskopie (FCS) und Daten aus der Literatur überein. Aus der Partitionierung der Dextranmoleküle entwickelten wir ein Freies-Volumenmodell, das auch die elastische Flexibilität sowohl der Dextran- als auch der PEG-Polymere berücksichtigt. Wir erhielten eine geschätzte Maschengröße, die auf eine heterogene Gelstruktur mit einer breiten Porengrößenverteilung hinwies.

8 References

[1] I. Y. Jung, E. H. Lee, A. Y. Suh, S. J. Lee, H. Lee, *Anal. Bioanal. Chem.* **2016**, *408*, 2383-2406.

[2] W. H. Koch, *Nat. Rev. Drug Discov.* **2004**, *3*, 749-761.

[3] J. Kim, A. S. Campbell, B. E.-F. de Ávila, J. Wang, *Nat. Biotechnol.* **2019**, *37*, 389-406.

[4] J. Chao, Z. Li, J. Li, H. Peng, S. Su, Q. Li, C. Zhu, X. Zuo, S. Song, L. Wang, L. Wang, *Biosens. Bioelectron.* **2016**, *81*, 92-96.

[5] A. Larsson, T. Ekblad, O. Andersson, B. Liedberg, *Biomacromolecules* **2007**, *8*, 287-295.

[6] A. Mateescu, Y. Wang, J. Dostalek, U. Jonas, *Membranes* **2012**, *2*, 40-69.

[7] P. Dey, T. Schneider, L. Chiappisi, M. Gradzielski, G. Schulze-Tanzil, R. Haag, *Macromol. Biosci.* **2016**, *16*, 580-590.

[8] N. A. Peppas, J. Z. Hilt, A. Khademhosseini, R. Langer, *Adv. Mater.* **2006**, *18*, 1345-1360.

[9] J. Li, D. J. Mooney, *Nat. Rev. Mater.* **2016**, *1*, 16071.

[10] B. Grigoryan, S. J. Paulsen, D. C. Corbett, D. W. Sazer, C. L. Fortin, A. J. Zaita, P. T. Greenfield, N. J. Calafat, J. P. Gounley, A. H. Ta, F. Johansson, A. Randles, J. E. Rosenkrantz, J. D. Louis-Rosenberg, P. A. Galie, K. R. Stevens, J. S. Miller, *Science* **2019**, *364*, 458-464.

[11] Y. Zhang, J. Yu, K. Ren, J. Zuo, J. Ding, X. Chen, *Biomacromolecules* **2019**, *20*, 1478-1492.

[12] S. P. Authimoolam, T. D. Dziubla, *Polymers* **2016**, *8*.

[13] O. Wichterle, D. LÍM, *Nature* **1960**, *185*, 117-118.

[14] W. S. Jinn, M.-K. Shin, B. Kang, S. Oh, C.-E. Moon, B. Mun, Y. W. Ji, H. K. Lee, S. Haam, *J. Mater. Chem. B* **2019**, *7*, 7120-7128.

[15] F. Li, D. Lyu, S. Liu, W. Guo, *Adv. Mater.* **2020**, *32*, 1806538.

[16] G. W. M. Vandermeulen, H.-A. Klok, *Macromol. Biosci.* **2004**, *4*, 383-398.

[17] C. Ghobril, E. K. Rodriguez, A. Nazarian, M. W. Grinstaff, *Biomacromolecules* **2016**, *17*, 1235-1252.

[18] X. Li, Y. Zhao, D. Li, G. Zhang, X. Gao, S. Long, *Polym. Eng. Sci.* **2019**, *59*, 145-154.

[19] H. C. Kolb, M. G. Finn, K. B. Sharpless, *Angew. Chem. Int. Ed.* **2001**, *40*, 2004-2021.

[20] Y. Okumura, K. Ito, *Adv. Mater.* **2001**, *13*, 485-487.

[21] E. M. Sletten, C. R. Bertozzi, *Angew. Chem. Int. Ed.* **2009**, *48*, 6974-6998.

[22] H. Meier, H. Petersen, H. Kolshorn, *Chem. Ber.* **1980**, *113*, 2398-2409.

[23] R. B. Turner, A. D. Jarrett, P. Goebel, B. J. Mallon, *J. Am. Chem. Soc.* **1973**, *95*, 790-792.

[24] J. Garcia-Hartjes, J. Dommerholt, T. Wennekes, F. L. van Delft, H. Zuilhof, *Eur. J. Org. Chem.* **2013**, *2013*, 3712-3720.

[25] M. L. Blackman, M. Royzen, J. M. Fox, *J. Am. Chem. Soc.* **2008**, *130*, 13518-13519.

[26] P. Dey, M. Adamovski, S. Friebe, A. Badalyan, R.-C. Mutihac, F. Paulus, S. Leimkühler, U. Wollenberger, R. Haag, *ACS Appl. Mater. Interfaces* **2014**, *6*, 8937-8941.

[27] S. M. Hodgson, S. A. McNelles, L. Abdullahu, I. A. Marozas, K. S. Anseth, A. Adronov, *Biomacromolecules* **2017**, *18*, 4054-4059.

[28] D. Steinhilber, T. Rossow, S. Wedepohl, F. Paulus, S. Seiffert, R. Haag, *Angew. Chem. Int. Ed.* **2013**, *52*, 13538-13543.

[29] C. M. Madl, S. C. Heilshorn, *Adv. Funct. Mater.* **2018**, *28*, 1706046.
[30] E. Alexandre, B. Schmitt, K. Boudjema, E. W. Merrill, P. J. Lutz, *Macromol. Biosci.* **2004**, *4*, 639-648.
[31] C.-H. Park, C. K. Son, J. H. Park, I. S. Chung, *Biotechnol. Bioprocess Eng.* **1997**, *2*, 113-116.
[32] M. A. Carnahan, C. Middleton, J. Kim, T. Kim, M. W. Grinstaff, *J. Am. Chem. Soc.* **2002**, *124*, 5291-5293.
[33] D. L. Wang, T. Y. Zhao, X. Y. Zhu, D. Y. Yan, W. X. Wang, *Chem. Soc. Rev.* **2015**, *44*, 4023-4071.
[34] R. Haag, A. Sunder, J.-F. Stumbé, *J. Am. Chem. Soc.* **2000**, *122*, 2954-2955.
[35] A. Sunder, R. Hanselmann, H. Frey, R. Mülhaupt, *Macromolecules* **1999**, *32*, 4240-4246.
[36] D. Wilms, S. E. Stiriba, H. Frey, *Acc. Chem. Res.* **2010**, *43*, 129-141.
[37] R. K. Kainthan, J. Janzen, E. Levin, D. V. Devine, D. E. Brooks, *Biomacromolecules* **2006**, *7*, 703-709.
[38] S. Abbina, S. Vappala, P. Kumar, E. M. J. Siren, C. C. La, U. Abbasi, D. E. Brooks, J. N. Kizhakkedathu, *J. Mater. Chem. B* **2017**, *5*, 9249-9277.
[39] C. Siegers, M. Biesalski, R. Haag, *Chem. - Eur. J.* **2004**, *10*, 2831-2838.
[40] G. R. Newkome, G. R. Baker, S. Arai, M. J. Saunders, P. S. Russo, K. J. Theriot, C. N. Moorefield, L. E. Rogers, J. E. Miller, *J. Am. Chem. Soc.* **1990**, *112*, 8458-8465.
[41] M. H. M. Oudshoorn, R. Rissmann, J. A. Bouwstra, W. E. Hennink, *Biomaterials* **2006**, *27*, 5471-5479.
[42] N. E. Fedorovich, M. H. Oudshoorn, D. van Geemen, W. E. Hennink, J. Alblas, W. J. A. Dhert, *Biomaterials* **2009**, *30*, 344-353.
[43] D. Steinhilber, S. Seiffert, J. A. Heyman, F. Paulus, D. A. Weitz, R. Haag, *Biomaterials* **2011**, *32*, 1311-1316.
[44] E. Kapourani, F. Neumann, K. Achazi, J. Dernedde, R. Haag, *Macromol. Biosci.* **2018**, *18*, 1800116.
[45] T. Rossow, J. A. Heyman, A. J. Ehrlicher, A. Langhoff, D. A. Weitz, R. Haag, S. Seiffert, *J. Am. Chem. Soc.* **2012**, *134*, 4983-4989.
[46] B. von Lospichl, S. Hemmati-Sadeghi, P. Dey, T. Dehne, R. Haag, M. Sittinger, J. Ringe, M. Gradzielski, *Colloids Surf. B. Biointerfaces* **2017**, *159*, 477-483.
[47] D. Williams, *Med Device Technol* **2003**, *14*, 10-13.
[48] G. Gao, D. Lange, K. Hilpert, J. Kindrachuk, Y. Zou, J. T. J. Cheng, M. Kazemzadeh-Narbat, K. Yu, R. Wang, S. K. Straus, D. E. Brooks, B. H. Chew, R. E. W. Hancock, J. N. Kizhakkedathu, *Biomaterials* **2011**, *32*, 3899-3909.
[49] M. Bochenek, N. Oleszko-Torbus, W. Wałach, D. Lipowska-Kur, A. Dworak, A. Utrata-Wesołek, *Polym. Rev.* **2020**, 1-51.
[50] W. Sun, W. Liu, Z. Wu, H. Chen, *Macromol. Rapid Commun.* **2020**, *41*, 1900430.
[51] P. B. Messersmith, J. Rivera, Y.-K. Gong, US 8,796,394 B2 ed., Northwestern University, Evanston, IL USA, **2014**.
[52] T. Ekblad, G. Bergström, T. Ederth, S. L. Conlan, R. Mutton, A. S. Clare, S. Wang, Y. Liu, Q. Zhao, F. D'Souza, G. T. Donnelly, P. R. Willemsen, M. E. Pettitt, M. E. Callow, J. A. Callow, B. Liedberg, *Biomacromolecules* **2008**, *9*, 2775-2783.
[53] M. Weinhart, T. Becherer, N. Schnurbusch, K. Schwibbert, H.-J. Kunte, R. Haag, *Adv. Eng. Mater.* **2011**, *13*, B501-B510.
[54] Q. Wei, T. Becherer, S. Angioletti-Uberti, J. Dzubiella, C. Wischke, A. T. Neffe, A. Lendlein, M. Ballauff, R. Haag, *Angew. Chem. Int. Ed.* **2014**, *53*, 8004-8031.

[55] K. Höger, T. Becherer, W. Qiang, R. Haag, W. Frieß, S. Küchler, *Eur. J. Pharm. Biopharm.* **2013**, *85*, 756-764.
[56] S. Q. Liu, C. Yang, Y. Huang, X. Ding, Y. Li, W. M. Fan, J. L. Hedrick, Y.-Y. Yang, *Adv. Mater.* **2012**, *24*, 6484-6489.
[57] E. Axpe, D. Chan, G. S. Offeddu, Y. Chang, D. Merida, H. L. Hernandez, E. A. Appel, *Macromolecules* **2019**, *52*, 6889-6897.
[58] C. N. Salinas, K. S. Anseth, *Macromolecules* **2008**, *41*, 6019-6026.
[59] E. Karpushkin, M. Dušková-Smrčková, M. Šlouf, K. Dušek, *Polymer* **2013**, *54*, 661-672.
[60] H. Holback, Y. Yeo, K. Park, in *Biomedical Hydrogels* (Ed.: S. Rimmer), Woodhead Publishing, **2011**, pp. 3-24.
[61] P. J. Flory, J. Rehner, *J. Chem. Phys.* **1943**, *11*, 521-526.
[62] N. A. Peppas, P. Bures, W. Leobandung, H. Ichikawa, *Eur. J. Pharm. Biopharm.* **2000**, *50*, 27-46.
[63] M. T. Shaw, W. J. MacKnight, *Introduction to Polymer Viscoelasticity*, 4th ed., John Wiley & Sons, Inc, New York, **2018**.
[64] K. S. Anseth, C. N. Bowman, L. Brannon-Peppas, *Biomaterials* **1996**, *17*, 1647-1657.
[65] A. Borzacchiello, L. Ambrosio, *Hydrogels: Biological Properties and Applications*, Springer-Verlag, Milan, **2009**.
[66] P. J. Flory, N. Rabjohn, M. C. Shaffer, *J. Polym. Sci.* **1949**, *4*, 225-245.
[67] F. A. Morrison, *Understanding Rheology*, New York, NY: Oxford University Press, **2001**.
[68] J. M. Zuidema, C. J. Rivet, R. J. Gilbert, F. A. Morrison, *J. Biomed. Mater. Res., Part B* **2014**, *102*, 1063-1073.
[69] J. D. Ferry, *Viscoelastic Properties of Polymers*, 3 ed., NY: Wiley, New York,, **1980**.
[70] M. N. Mason, A. T. Metters, C. N. Bowman, K. S. Anseth, *Macromolecules* **2001**, *34*, 4630-4635.
[71] G. M. Cruise, D. S. Scharp, J. A. Hubbell, *Biomaterials* **1998**, *19*, 1287-1294.
[72] R. A. Gemeinhart, J. Chen, H. Park, K. Park, *J. Biomater. Sci., Polym. Ed.* **2000**, *11*, 1371-1380.
[73] T. Sakai, T. Matsunaga, Y. Yamamoto, C. Ito, R. Yoshida, S. Suzuki, N. Sasaki, M. Shibayama, U.-i. Chung, *Macromolecules* **2008**, *41*, 5379-5384.
[74] Y. Shmidov, M. Zhou, G. Yosefi, R. Bitton, J. B. Matson, *Soft Matter* **2019**, *15*, 917-925.
[75] B. Singh, B. Singh, *Int. J. Biol. Macromol.* **2018**, *116*, 91-99.
[76] J. Karvinen, T. O. Ihalainen, M. T. Calejo, I. Jönkkäri, M. Kellomäki, *Mater. Sci. Eng., C* **2019**, *94*, 1056-1066.
[77] M. Doi, S. F. Edward, *The Theory of Polymer Dynamics*, Clarendon Press, Oxford, **1986**.
[78] T. Canal, N. A. Peppas, *J. Biomed. Mater. Res.* **1989**, *23*, 1183-1193.
[79] S. P. Zustiak, J. B. Leach, *Biomacromolecules* **2010**, *11*, 1348-1357.
[80] N. A. Peppas, H. J. Moynihan, L. M. Lucht, *J. Biomed. Mater. Res.* **1985**, *19*, 397-411.
[81] O. Lieleg, K. Ribbeck, *Trends Cell Biol.* **2011**, *21*, 543-551.
[82] E. W. Merrill, K. A. Dennison, C. Sung, *Biomaterials* **1993**, *14*, 1117-1126.
[83] C. C. Miller, J. Walker, *Proceedings of the Royal Society of London. Series A, Containing Papers of a Mathematical and Physical Character* **1924**, *106*, 724-749.
[84] S. Liese, M. Gensler, S. Krysiak, R. Schwarzl, A. Achazi, B. Paulus, T. Hugel, J. P. Rabe, R. R. Netz, *ACS Nano* **2017**, *11*, 702-712.

[85] L. Masaro, X. X. Zhu, *Prog. Polym. Sci.* **1999**, *24*, 731-775.
[86] Y. Cheng, R. K. Prud'homme, J. L. Thomas, *Macromolecules* **2002**, *35*, 8111-8121.
[87] D. E. Liu, C. Kotsmar, F. Nguyen, T. Sells, N. O. Taylor, J. M. Prausnitz, C. J. Radke, *Ind. Eng. Chem. Res.* **2013**, *52*, 18109-18120.
[88] M. Marczynski, B. T. Käsdorf, B. Altaner, A. Wenzler, U. Gerland, O. Lieleg, *Biomaterials Science* **2018**, *6*, 3373-3387.
[89] R. Renneberg, D. Pfeiffer, F. Lisdat, G. Wilson, U. Wollenberger, F. Ligler, A. P. Turner, *Adv. Biochem. Eng./Biotechnol.* **2008**, *109*, 1-18.
[90] O. S. Kwon, H. S. Song, T. H. Park, J. Jang, *Chem. Rev.* **2019**, *119*, 36-93.
[91] A. Vallée-Bélisle, F. Ricci, K. W. Plaxco, *J. Am. Chem. Soc.* **2012**, *134*, 2876-2879.
[92] F. Scheller, F. Schubert, *Biosensors, Vol. 11*, Elesevier Science Publishers B.V., Amsterdam, Netherlands, **1992**.
[93] N. J. Ronkainen, H. B. Halsall, W. R. Heineman, *Chem. Soc. Rev.* **2010**, *39*, 1747-1763.
[94] A. L. Nelson, J. M. Reichert, *Nat. Biotechnol.* **2009**, *27*, 331-337.
[95] L. J. F. Hefta, M. Neumaier, J. E. Shively, *Immunotechnology* **1998**, *4*, 49-57.
[96] B. Saha, T. H. Evers, M. W. J. Prins, *Anal. Chem.* **2014**, *86*, 8158-8166.
[97] X. Yu, Y.-P. Yang, E. Dikici, S. K. Deo, S. Daunert, *Annu. Rev. Anal. Chem.* **2017**, *10*, 293-320.
[98] A. R. Jones, C. C. Stutz, Y. Zhou, J. D. Marks, E. V. Shusta, *Biotechnol. J.* **2014**, *9*, 664-674.
[99] E. Takano, N. Shimura, Y. Ujima, H. Sunayama, Y. Kitayama, T. Takeuchi, *ACS Omega* **2019**, *4*, 1487-1493.
[100] A. L. Nelson, *MAbs* **2010**, *2*, 77-83.
[101] V. Crivianu-Gaita, A. Romaschin, M. Thompson, *Biochem. Biophys, Rep.* **2015**, *2*, 23-28.
[102] D. Saerens, L. Huang, K. Bonroy, S. Muyldermans, *Sensors phiri*
2008, *8*, 4669-4686.
[103] E. O. Saphire, R. L. Stanfield, M. D. Max Crispin, P. W. H. I. Parren, P. M. Rudd, R. A. Dwek, D. R. Burton, I. A. Wilson, *J. Mol. Biol.* **2002**, *319*, 9-18.
[104] H. Ueda, J. Dong, *Biochim. Biophys. Acta* **2014**, *1844*, 1951-1959.
[105] E. Engvall, P. Perlmann, *Immunochemistry* **1971**, *8*, 871-874.
[106] B. K. Van Weemen, A. H. Schuurs, *FEBS Lett.* **1971**, *15*, 232-236.
[107] A. Villalonga, A. M. Pérez-Calabuig, R. Villalonga, *Anal. Bioanal. Chem.* **2020**, *412*, 55-72.
[108] W. Xiang, Q. Lv, H. Shi, B. Xie, L. Gao, *Talanta* **2020**, *214*, 120716.
[109] P. M. Cullen, in *Leitfaden Molekulare Diagnostik* (Eds.: F. Thiemann, P. M. Cullen, H.-G. Klein), WILEY-VCH, Weinheim, **2006**.
[110] Y. Wang, K. Kang, S. Wang, W. Kang, C. Cheng, L. M. Niu, Z. Guo, *Sensors Actuators B: Chem.* **2020**, *305*, 127348.
[111] H. Li, L. J. Rothberg, *Anal. Chem.* **2004**, *76*, 5414-5417.
[112] J. Schonborn, J. Oberstraβ, E. Breyel, J. Tittgen, J. Schumacher, N. Lukacs, *Nucleic Acids Res.* **1991**, *19*, 2993-3000.
[113] S. Takenaka, K. Yamashita, M. Takagi, Y. Uto, H. Kondo, *Anal. Chem.* **2000**, *72*, 1334-1341.
[114] B. Esteban Fernández de Ávila, H. M. Watkins, J. M. Pingarrón, K. W. Plaxco, G. Palleschi, F. Ricci, *Anal. Chem.* **2013**, *85*, 6593-6597.
[115] S. Yoshida, K. Hagiwara, T. Hasebe, A. Hotta, *Surf. Coat. Technol.* **2013**, *233*, 99-107.

[116] S. S. Mark, N. Sandhyarani, C. Zhu, C. Campagnolo, C. A. Batt, *Langmuir* **2004**, *20*, 6808-6817.
[117] C.-J. Huang, N. D. Brault, Y. Li, Q. Yu, S. Jiang, *Adv. Mater.* **2012**, *24*, 1834-1837.
[118] A. Hennig, H. Borcherding, C. Jaeger, S. Hatami, C. Würth, A. Hoffmann, K. Hoffmann, T. Thiele, U. Schedler, U. Resch-Genger, *J. Am. Chem. Soc.* **2012**, *134*, 8268-8276.
[119] Y. Gao, L. K. Wolf, R. M. Georgiadis, *Nucleic Acids Res.* **2006**, *34*, 3370-3377.
[120] Y. Jung, J. Y. Jeong, B. H. Chung, *Analyst* **2008**, *133*, 697-701.
[121] S. Löfas, B. Johnsson, *J. Chem. Soc., Chem. Commun.* **1990**, 1526-1528.
[122] P. Pavlickova, E. M. Schneider, H. Hug, *Clin. Chim. Acta* **2004**, *343*, 17-35.
[123] J. E. Butler, L. Ni, W. R. Brown, K. S. Joshi, J. Chang, B. Rosenberg, E. W. Voss, *Mol. Immunol.* **1993**, *30*, 1165-1175.
[124] M. M. Phiri, D. W. Mulder, S. Mason, B. C. Vorster, *R. Soc. Open Sci.* **2019**, *6*, 190205.
[125] A. N. Glazer, *Annu. Rev. Biochem* **1970**, *39*, 101-130.
[126] T. Cao, A. Wang, X. Liang, H. Tang, G. W. Auner, S. O. Salley, K. Y. S. Ng, *Biotechnol. Bioeng.* **2007**, *98*, 1109-1122.
[127] C. Schmidt, P. Schierack, U. Gerber, C. Schröder, Y. Choi, I. Bald, W. Lehmann, S. Rödiger, *Langmuir* **2020**, *36*, 628-636.
[128] L. Cohen, D. R. Walt, *Chem. Rev.* **2019**, *119*, 293-321.
[129] Q. Zhou, T. Kwa, Y. Gao, Y. Liu, A. Rahimian, A. Revzin, *LChip* **2014**, *14*, 276-279.
[130] I. Y. Jung, J. S. Kim, B. R. Choi, K. Lee, H. Lee, *Adv. Healthcare Mater.* **2017**, *6*.
[131] K. M. Dean, A. E. Palmer, *Nat. Chem. Biol.* **2014**, *10*, 512-523.
[132] Z. Guo, R. A. Guilfoyle, A. J. Thiel, R. Wang, L. M. Smith, *Nucleic Acids Res.* **1994**, *22*, 5456-5465.
[133] R. Bumgarner, *Curr. Protoc. Mol. Biol.* **2013**, *101*, 22.21.21-22.21.11.
[134] V. Crivianu-Gaita, M. Thompson, *Biosens. Bioelectron.* **2016**, *85*, 32-45.
[135] R. Wilson, A. R. Cossins, D. G. Spiller, *Angew. Chem. Int. Ed.* **2006**, *45*, 6104-6117.
[136] L. Settanni, A. Corsetti, *J. Microbiol. Methods* **2007**, *69*, 1-22.
[137] J. Lu, G. Getz, E. A. Miska, E. Alvarez-Saavedra, J. Lamb, D. Peck, A. Sweet-Cordero, B. L. Ebert, R. H. Mak, A. A. Ferrando, J. R. Downing, T. Jacks, H. R. Horvitz, T. R. Golub, *Nature* **2005**, *435*, 834-838.
[138] S. C. Chapin, D. C. Appleyard, D. C. Pregibon, P. S. Doyle, *Angew. Chem.* **2011**, *50*, 2289-2293.
[139] K. J. Lackne, in *Multiparameteranalytik in Forschung und Praxis* (Eds.: K. Conrad, D. Roggenbuck, W. Lehmann, U. Schedler, U. Peine), Pabst Science Publishers, Lengerich, Berlin, Bremen, Miami, Riga, Viernheim, Wien, Zagreb, **2011**.
[140] R. Jin, Y. C. Cao, C. S. Thaxton, C. A. Mirkin, *Small* **2006**, *2*, 375-380.
[141] S. Rödiger, C. Liebsch, C. Schmidt, W. Lehmann, U. Resch-Genger, U. Schedler, P. Schierack, *Microchimica Acta* **2014**, *181*, 1151-1168.
[142] L. Bonetta, *Nat. Methods* **2005**, *2*, 785-795.
[143] W. Lehmann*, Vol. US7361515B2*, Attomol Molekulare Diagnostika GmbH, **2008**.
[144] W. Lehmann, A. Böhm, K. Grossmann, R. Hiemann, J. Nitschke, S. Rödiger*, Vol. WO/2008/152145*, Attomol Molekulare Diagnostika GmbH, **2008**.
[145] S. Rödiger, P. Schierack, A. Böhm, J. Nitschke, I. Berger, U. Frömmel, C. Schmidt, M. Ruhland, I. Schimke, D. Roggenbuck, W. Lehmann, C. Schröder, in *Molecular Diagnostics* (Eds.: H. Seitz, S. Schumacher), Springer Berlin Heidelberg, Berlin, Heidelberg, **2013**, pp. 35-74.
[146] B.-H. Jun, H. Kang, Y.-S. Lee, D. H. Jeong, *Molecules* **2012**, *17*, 2474-2490.

[147] S. H. Gehrke, L. H. Uhden, J. F. McBride, *J. Controlled Release* **1998**, *55*, 21-33.
[148] M. Khayyami, M. T. Pérez Pita, N. Peña Garcia, G. Johansson, B. Danielsson, P.-O. Larsson, *Talanta* **1998**, *45*, 557-563.
[149] P. Arenkov, A. Kukhtin, A. Gemmell, S. Voloshchuk, V. Chupeeva, A. Mirzabekov, *Anal. Biochem.* **2000**, *278*, 123-131.
[150] L. Meng, A. P. F. Turner, W. C. Mak, *Biotechnol. Adv.* **2020**, *39*, 107398.
[151] M. Xu, D. Obodo, V. K. Yadavalli, *Biosens. Bioelectron.* **2019**, *124-125*, 96-114.
[152] Y.-J. Liu, W.-T. Cao, M.-G. Ma, P. Wan, *ACS Appl. Mater. Interfaces* **2017**, *9*, 25559-25570.
[153] Y. R. Lin, C. C. Hung, H. Y. Chiu, B. H. Chang, B. R. Li, S. J. Cheng, J. W. Yang, S. F. Lin, G. Y. Chen, *Sensors* **2018**, *18*.
[154] R. K. Pal, A. A. Farghaly, M. M. Collinson, S. C. Kundu, V. K. Yadavalli, *Adv. Mater.* **2016**, *28*, 1406-1412.
[155] R. K. Pal, A. A. Farghaly, C. Wang, M. M. Collinson, S. C. Kundu, V. K. Yadavalli, *Biosens. Bioelectron.* **2016**, *81*, 294-302.
[156] A. Herrmann, L. Kaufmann, P. Dey, R. Haag, U. Schedler, *ACS Appl. Mater. Interfaces* **2018**, *10*, 11382-11390.
[157] A. Herrmann, S. Rödiger, C. Schmidt, P. Schierack, U. Schedler, *Anal. Chem.* **2019**, *91*, 8484-8491.

9 List of abbreviations

Ab	antibody
BSA	bovine serum albumin
DNA	deoxyribonucleic acid
dPG	dendritic polyglycerol
Fab	fragment antigen binding
FCS	fluorescence correlation spectroscopy
h	hour
HEMA	hydroxyethylmethacrylat
hPG	hyperbranched polyglycerol
Ig	immunoglobulin
IUPAC	International Union of Pure and Applied Chemistry
N_3	azide
PEG	polyethylene glycol
PHEMA	poly(2-hydroxyethyl methacrylate)
RNA	ribonucleic acid
r.t.	room temperature
SAOS	small-amplitude oscillatory shear
BCN	bicyclo[6.1.0]non-4-yn-9-yl

10 List of Publications, Patents, Manuscripts, and Conferences

Publications, Manuscript, and Patent:

[1] Wolde-Kidan, A.; Herrmann, A.; Prause, A.; Gradzielski, M.; Haag, R.; Block, S.; Netz, R., Particle Diffusivity and Free-Energy Profiles in Inhomogeneous Hydrogel Systems from Time-Resolved Penetration Profiles, preprint.
http://arxiv.org/abs/2006.10676

[2] Herrmann, A.; Rödiger, S.; Schmidt, C.; Schierack, P.: Schedler, U., Spatial Separation of Microbeads into Detection Levels by a Bioorthogonal Porous Hydrogel for Size-Selective Analysis and Increased Multiplexity. *Analytical Chemistry* **2019**, 91 (13), 8484-8491

[3] Herrmann, A.; Kaufmann, L.; Dey, P.; Haag, R.; Schedler, U., Bioorthogonal in Situ Hydrogels Based on Polyether Polyols for New Biosensor Materials with High Sensitivity. *ACS Applied Materials & Interfaces* **2018,** *10* (13), 11382-11390.

[4] Trunk, M.; Herrmann, A.; Bildirir, H.; Yassin, A.; Schmidt, J.; Thomas, A., Copper-Free Sonogashira Coupling for High-Surface-Area Conjugated Microporous Poly(aryleneethynylene) Networks. *Chemistry – A European Journal* **2016,** *22* (21), 7179-7183.

[5] Patent DE 10 2018 115391.0, WO 2020/002350 A1
Herrmann, A.; Rödiger, S.; Haag, R.; Schierack, P.; Schedler, U.
"Assay, Verfahren zu seiner Herstellung sowie seine Verwendung"

Oral presentations:

[1] **A. Herrmann**, R. Haag, P. Schierack, S. Rödiger, U. Schedler
Geometric Separation of Detection Levels by a Bioorthogonal Porous Polymer – Introducing Functionality and Multiplexicity.

Frontiers in Biomedical Polymers – 13th International Symposium (Teneriffe, Spain), May 2019

[2] **A. Herrmann,** R. Haag, P. Schierack, S. Rödiger, U. Schedler
Development of a multilayered microbead based assay for a size selective detection with increased multiplexicity
Award: Best talk
International Biotech Innovation Days (Senftenberg), May 2018

[3] **A. Herrmann**, U. Schedler, R. Haag
Bioorthogonal in situ Hydrogels based on Polyether-Polyols for new Biosensor Materials with high Sensitivity
The International Conference on Surfaces, Coatings and Interfaces, Surfaces and Coatings (Incheon, South Korea), March 2018

Poster presentations:

[1] **A. Herrmann**, S. Rödiger, P. Schierack, U. Schedler, R. Haag
Geometric Separation of Detection Levels by a Bioorthogonal Porous Polymer – Introducing Functionality and Multiplexicity.
Biennial Meeting of the GDCh-Division of Macromolecular Chemistry: Dimension Control of Polymer Materials – From Synthesis to Function (Karlsruhe, Germany), September 2018

[2] **Anna Herrmann**, Lena Kaufmann, Pradip Dey, Rainer Haag, Uwe Schedler
Bioorthogonal 3D *in situ* Hydrogels for Highly Sensitive Biosensors
Poster presentation and speed lecture
International Symposium: Functional Biointerfaces (Berlin, Germany), October 2016

[3] Participation in Summer School: Materials for Biomedical Applications (Barcelona, Spain), June 2017

11 Curriculum vitae

For reasons of data protection, the curriculum vitae is not included in the online version.

Declaration of honesty

Hereby I declare and confirm that this PhD thesis is entirely the result of my own work and that no other sources than those cited have been used. All annotations, which have been used from published or unpublished sources, are identified as such. The shown illustrations have been created by me, or have been marked with the corresponding references.

_____

Anna Herrmann

June 2020